# JAYCOR

81 7 13 238

205 South Whiting Street
Alexandria, Virginia 22304

(12)

# PRELIMINARY EXPERIMENTAL DESIGN AND THEORETICAL INVESTIGATION OF A PLASMA IMPLOSION DRIVEN MASS ACCELERATOR

(9) Final Report

(14) JAYCOR FINAL REPORT NO. J207-81-008

prepared by:

(10) D. A. Tidman and S. A. Goldstein
JAYCOR
205 S. Whiting Street
Alexandria, VA 22304

DTIC
AUG 2 1 1981

submitted to:

Department of the Army (11) 1981
US Army Armament R&D Command
ATTN: Dr. Peter Kemmey
DRDAR-PRW-FS
Dover, NJ 07801

(15)
Contract: DAAK10-80-C-0267
Amount: $49,900
Period: 9/29/80 - 6/30/81

393 453

# CONTENTS

## 1.    INTRODUCTION

The basic idea that motivated this research effort is the prospect that a series of timed z-pinch plasma implosions could be used to sequentially propel a projectile to high velocities.  Such a process would provide us with a new type of electrically driven gun with the potential for achieving projectile velocities well above those attainable by chemical guns.  The concept in its earliest form is described in references 1-4 and the system appears to have the attractive feature of being potentially rep-ratable. The current flows axially along sections of the accelerator instead of perpendicular to the projectile path as in a rail gun, i.e., plasma pressure propels the projectile, not the $\underline{j} \times \underline{B}$ force.

The primary objective of this research was to design a test module which if built could be used to investigate the effectiveness of such z-pinch implosions for projectile propulsion.  Other objectives were to examine background experimental information on z-pinch implosions and to explore a range of parameters using a lumped-parameter computer model for the implosions and their driving circuits.. Our results for these three components of the program are presented in sections 2, 3, and the Appendix.

## 2.    DESIGN AND ENGINEERING DRAWINGS FOR AN ACCELERATOR TEST MODULE

In this section we have compiled the drawings (Figures 1-28) that provide a design for a single test module.  Such a design also has the advantage that it can easily be stacked into an assembly of more than one module.  This has been verified by using internal GT-Devices funds to construct and perform experiments with several of these modules of various implosion chamber designs.  In order to provide the reader with a visual image we have also enclosed a picture (Figure 29) showing an

assembled 5 module system. The remaining figures and captions give the particular drawings that were prepared under the support of this contract.

## 3. LUMPED PARAMETER IMPLOSION MODEL

This model is based on an equation for the driving circuit energized by a capacitor, together with a snow-plow model for the imploding z-pinch discharge. The snow plow model assumes that all of the gas initially present in the implosion volume is swept up by the radially imploding discharge which in turn is propelled inward by the $\underline{j} \times \underline{B}$ force involving the self azimuthal magnetic field. The geometry is shown in Figure 30 and the model is discussed in reference 1.

In this section we first summarize the model equations, and then present some computer results that provide us with a view of how things vary over a range of parameters. The basic equations are an equation of motion for the imploding plasma shell:

$$ m_g \frac{d}{dt} \left[ (1 - \frac{a^2}{a_w^2}) \dot{a} \right] = - \frac{I^2 \ell}{ac^2} \tag{1} $$

together with the circuit equation

$$ V = \frac{Q}{c} = \frac{d}{dt} (LI) + IR $$

$$ L = L_g + \frac{2\ell}{c^2} \ell n \left( \frac{a_w}{a} \right) \tag{2} $$

$$ R \approx \ell / 2\pi\sigma\delta a $$

for an implosion driven by discharge of a capacitor C, where $L$, $L_g$, $R$, $V$ are the total inductance, external inductance, discharge resistance, and voltage, respectively, and

2

$$m_g = \pi a_w^2 \ell \rho_0 \qquad (3)$$

is the mass of gas in the module. In the formula for the discharge resistance we take $\delta$ as the current penetration skin depth, i.e.,

$$\delta = \left(\frac{c^2 t}{4\pi\sigma}\right)^{\frac{1}{2}} + \delta_{flash} , \qquad (4)$$

where $\sigma$ is assumed constant and $\delta_{flash}$ is the small initial conducting layer thickness associated with the initiating surface breakdown at $a_w$.

In deriving scaling laws or utilizing computer results it is useful to write these equations in the following dimensionless form:

$$\frac{d}{d\tau}\left((1-A^2)\frac{dA}{d\tau}\right) = -\frac{i^2}{A} ,$$

$$\frac{d^2}{d\tau^2}(\mathscr{L}i) + \frac{d}{d\tau}\left(\frac{ir}{A(\tau^{\frac{1}{2}} + \varepsilon)}\right) + i = 0 , \qquad (5)$$

where the dimensionless radius A, current i, and time $\tau$ are defined by

$$A = a/a_w, \quad i = I/I_0, \quad \tau = \omega\tau , \qquad (6)$$

respectively, and

$$\mathscr{L} = \frac{L}{L_0} = \left(1 - \frac{L_m}{L_g}\frac{\ln A}{\ln(a_w/a_p)}\right)\left(1 + \frac{L_m}{L_g}\right)^{-1} ,$$

$$L_0 = L_g + L_m, \quad L_m = \frac{2\ell}{c^2}\ln\left(\frac{a_w}{a_p}\right) ,$$

$$\omega = (L_0 C)^{-\frac{1}{2}} , \qquad (7)$$

$$I_0 = c a_w \omega (m_g/\ell)^{\frac{1}{2}} ,$$

$$r = \frac{2\ell}{c a_w L_0 (4\pi\sigma\omega)^{\frac{1}{2}}}$$

3

$$\frac{1}{\sigma} = \frac{Z\ell nA}{1.7 \times 10^{14}T_{ev}^{3/2}} + \frac{1}{\sigma_{eo}} \quad ,$$

where $\sigma_{eo}^{-1}$ is the contribution to the resistivity from electron-neutral scattering.

The initial conditions at $\tau = 0$ are

$$A = 1 - \frac{\delta_{flash}}{a_w} \approx 1, \quad i = 0, \quad \frac{dA}{d\tau} = 0 \quad ,$$

$$\left(\frac{di}{d\tau}\right)_{\tau=0} = \frac{V_0}{L_g I_0 \omega} = \frac{(2C\ell)^{\frac{1}{2}}}{a_w} \left(1 + \frac{L_m}{L_g}\right)\left(\frac{\frac{1}{2}CV_0^2}{\pi a_w^2 \rho_0 c^2 \ell}\right)^{\frac{1}{2}} \quad .$$

(8)

Solutions are insensitive to the initial thin flash-over layer $\delta_{flash}$ which appears in both the initial value of A and also in the initial resistance.

Numerical solutions to Eq. (5) are presented in Figures 31-36 for a range of parameters. Figure 31 plots $A(\tau)$, $-\frac{dA}{d\tau}(\tau)$, and $i(\tau)$ for the standard set of parameters shown in Table 1. For simplicity, we assume that the resistance r is constant throughout the implosion. Unlike the examples shown in Ref. (1), there has been no attempt to "match" the implosions by choosing $\frac{di}{d\tau}(\tau=0)$ so that $i(\tau = \tau_{imp}) \approx 0$. (The implosion time $\tau_{imp}$ is the time at which $A(\tau) = a_p/a_w$.) The qualitative features of Figure 31 are reproduced over a very broad range of parameters. In the remaining examples, one of the quantities listed in Table 1 has been varied while holding the others constant.

A major factor in determining the behavior of the imploding plasma is the dimensionless initial current rise $\frac{di}{d\tau}(0)$. As can be seen from Eq. (8), this quantity can be readily varied by changing the gas density $\rho_0$. Figure 32 shows some of the effects of varying the current rise. As $\frac{di}{d\tau}(0)$ increases,

4

## Table 1

### Standard Parameters for Implosion Calculations
### (Dimensionless)

| Quantity | Value |
|---|---|
| Inductance Ratio: $L_m/L_g$ | 3 |
| Projectile radius: $a_p/a_w$ | 0.2 |
| Resistance: $r$ | 0.01 |
| Initial resistance: $\epsilon$ | 0.01 |
| Flashover width: $\delta_{flash}$ | $10^{-4}$ |
| Current rise rate: $\dfrac{di(0)}{d\tau}$ | 1.9 |

both the current $i(\tau_{imp})$ and efficiency $\epsilon_{imp}$ at $\tau = \tau_{imp}$ increase steadily. The efficiency for transfer of electrical energy to implosion kinetic energy was shwon in Ref. 1 to be

$$\epsilon_{imp} = \left[ \frac{(dA/d\tau)_{imp}}{\frac{di}{d\tau}(0)} \right]^2 \frac{\left(\frac{L_m}{L_g}\right)\left(1 + \frac{L_m}{L_g}\right)}{2(1-f) \ln \left(\frac{a_w}{a_p}\right)} \tag{9}$$

where f is the fraction of energy stored in the capacitor bank at the end of the implosion. Projectile stability considerations[1] require that $\frac{dP}{da}(\tau=\tau_{imp}) < 0$ where P is the radially-directed momentum per radian of the plasma annulus. This means that the speed of the implosion must be decreasing as $\tau \to \tau_{imp}$, or $\frac{d^2A}{d\tau^2} < 0$. Figure 32 demonstrates that the stabilizing force on the projectile is lost for $\frac{di}{d\tau}(0) > 2.0$. A more complete discussion of this point will be given later in this section.

The implosion time and implosion velocity are weakly dependent on $\frac{di}{d\tau}(0)$, as shown in Figure 33. As one would expect, a steeper rise in the current shortens the implosion time and increases the implosion velocity.

Figure 34 plots $\frac{dA}{d\tau}(\tau_{imp})$ and $i(\tau_{imp})$ as functions of the dimensionless resistance $r$. Unlike other quantities which we have varied, the plasma resistance is not actually a directly controllable parameter. For simplicity, we have assumed that it is constant, neglecting its complex dependence on plasma temperature and the degree of ionization. Increasing the resistance lowers the current and implosion velocity (and hence efficiency) although some of the energy may be recovered in the form of $I^2R$ heating of the plasma.

The ratio $a_p/a_w$ of the projectile radius to the wall radius is an easily varied parameter which is expected to change as the local projectile velocity changes. Figure 35 plots $\tau_{imp}$, $-\frac{dA}{d\tau}(\tau_{imp})$, and $i(\tau_{imp})$ as functions of $a_p/a_w$. The inductance ratio and initial current rise rate have been held constant, so some of the apparent loss in implosion velocity and efficiency, as $a_p/a_w$ increases, could be recovered by decreasing $\frac{di}{d\tau}(0)$.

Figure 36 illustrates the tradeoff between efficiency and projectile stability which was briefly discussed in connection with Figure 32. As discussed in Ref. 1, the projectile will tend to be stabilized against radial displacements if the implosion speed is decreasing as $\tau \to \tau_{imp}$. This condition is achieved in Figure 36 for $\frac{di}{d\tau}(0) = 1.6$. The thermal pressure term which was omitted from the right hand side of Eq. (5) will further decelerate the plasma. However, for $\frac{di}{d\tau}(0) = 2.1$, the implosion kinetic energy is higher, but the implosion velocity continues to increase

with $\tau$, so there may be a complete loss of projectile stability. It seems clear that projectile stability may be an important limiting factor for implosion velocity and efficiency.

# REFERENCES

1. D. A. Tidman and S. A. Goldstein, J. Appl. Phys. $\underline{51}$, 1975 (1980).

2. Proceedings of the Impact Fusion Workshop, LASL Report 8000-C (1979).

3. S. A. Goldstein, F. Sandel, D. A. Tidman, D. Massey, The MAID System, Data Base and Design Issues, Proceedings Conference on EM Guns and Launchers, November 4-6, 1980, San Diego, CA (sponsored by ARRADCOM/ DARPA).

4. D. A. Tidman, Applications of Rep-Ratable Mass Accelerators (such as MAID). Proceedings Conference on EM Guns and Launchers, November 4-6, 1980, San Diego, CA (sponsored by ARRADCOM/DARPA).
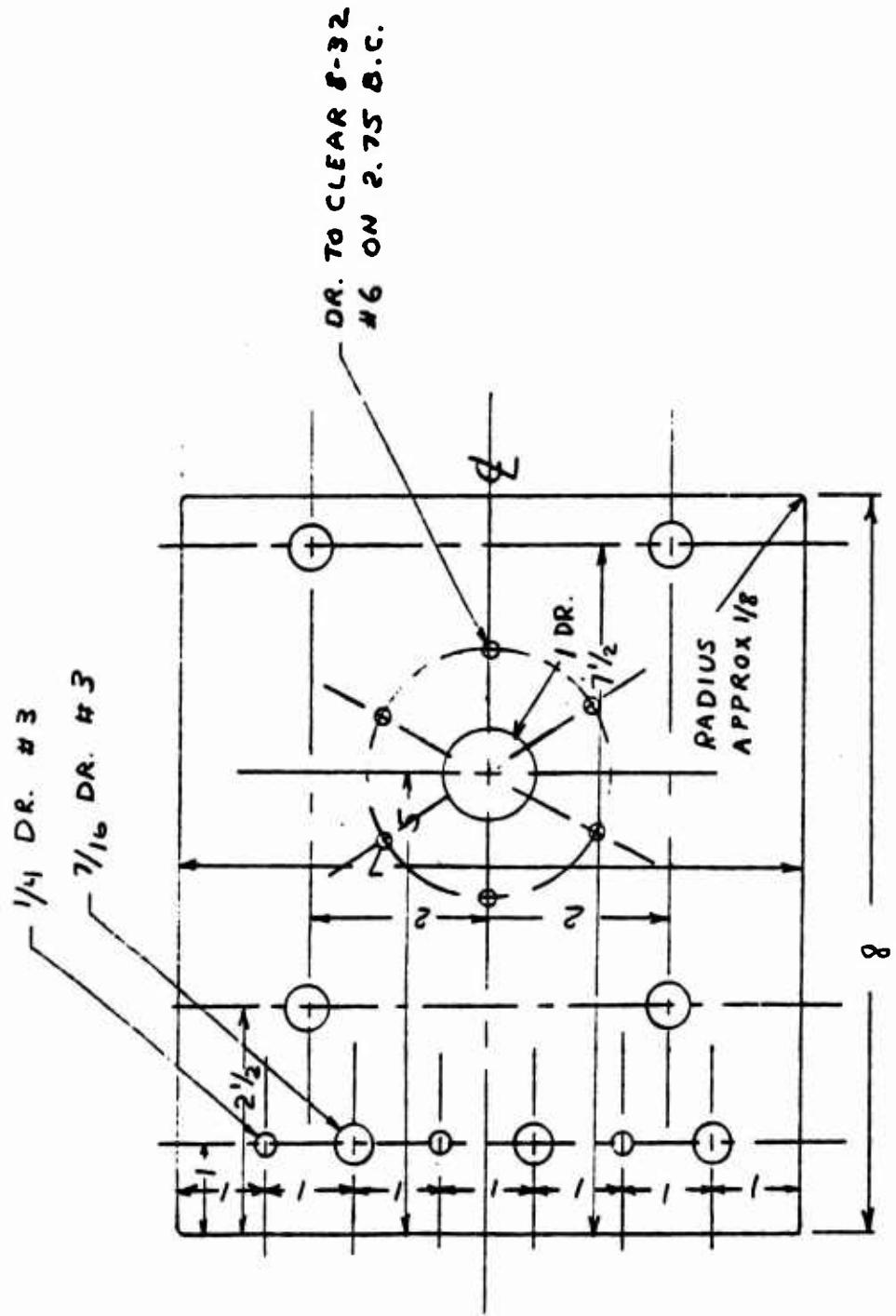
Figure 1. Inner Collector Plate
Scale: one half
Mat: 1/16 brass

9
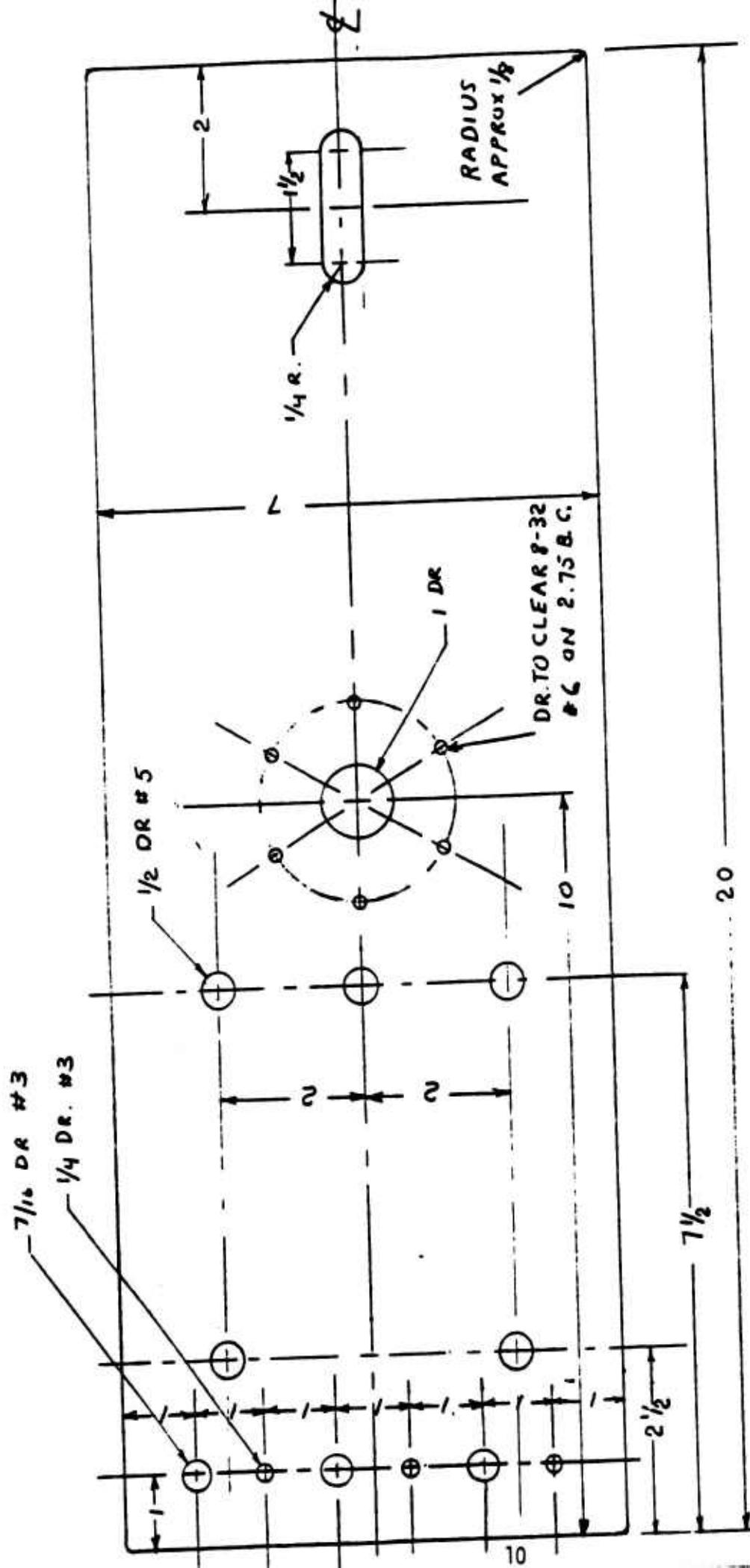
Figure 2. Outer Collector Plate
Scale: one half
Mat: 1/16 brass
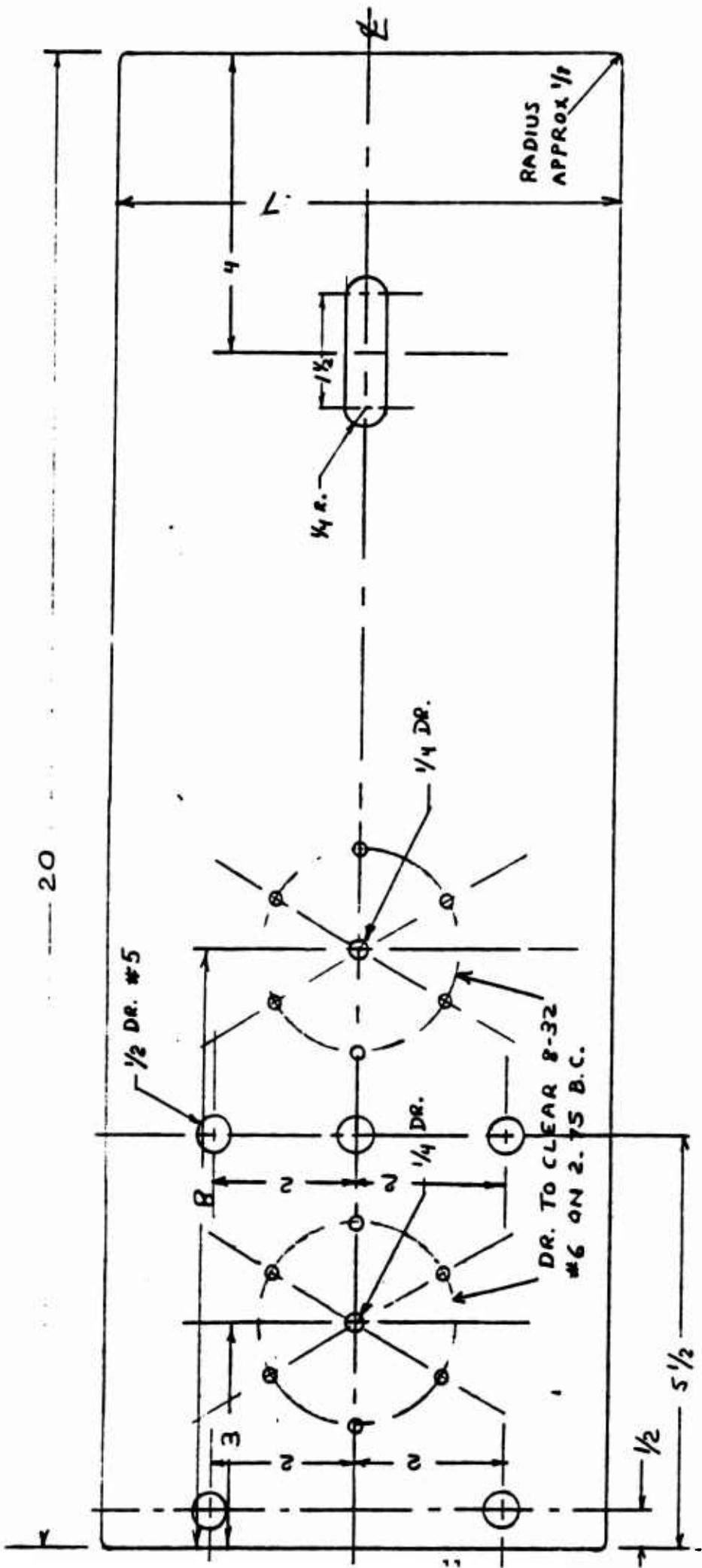
Figure 3.  Middle Collector Plate
Scale:  one half
Mat:  1/16 brass

Figure 4. Module Feed
Plate
Scale: full size
Mat: 1/16 brass
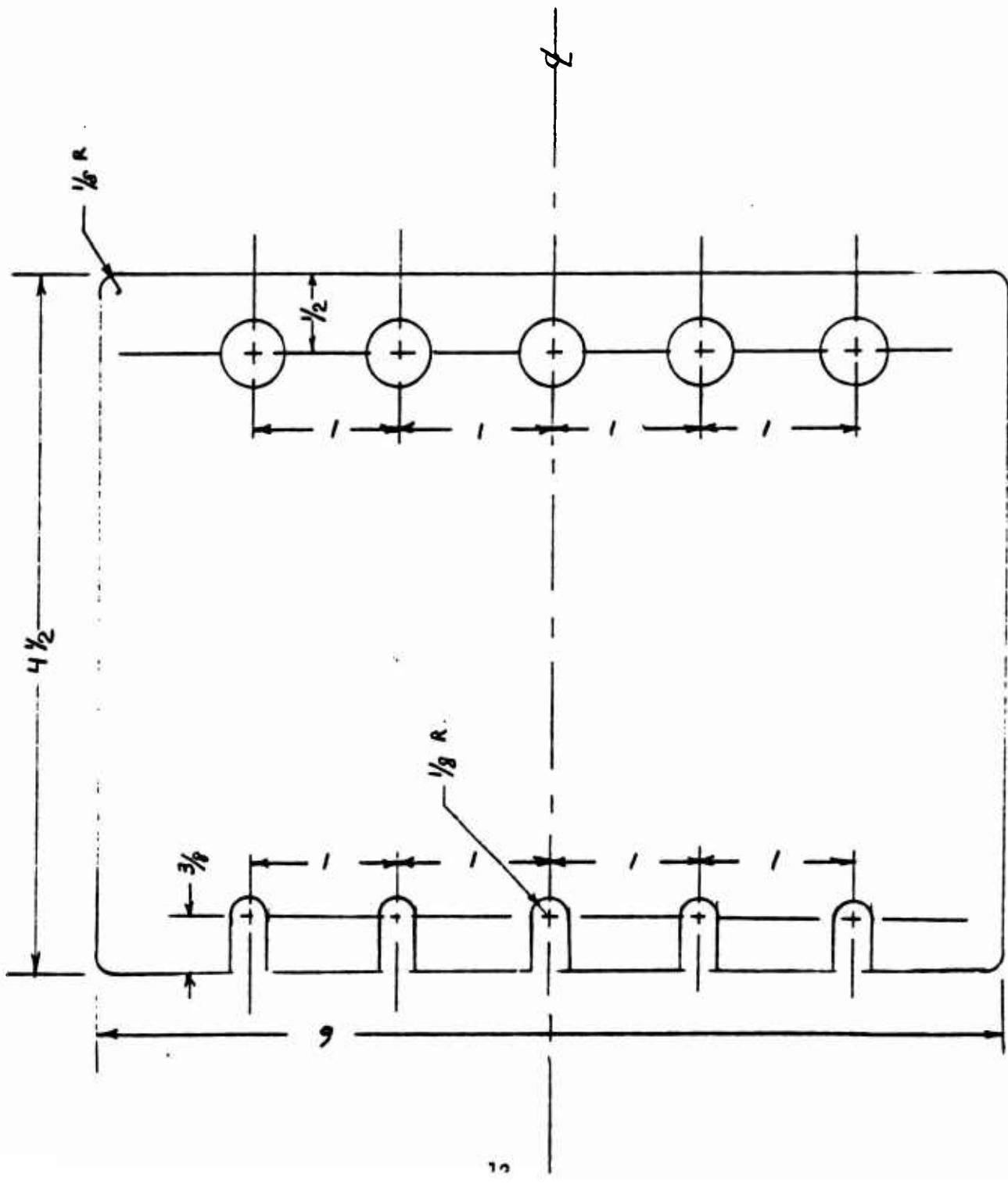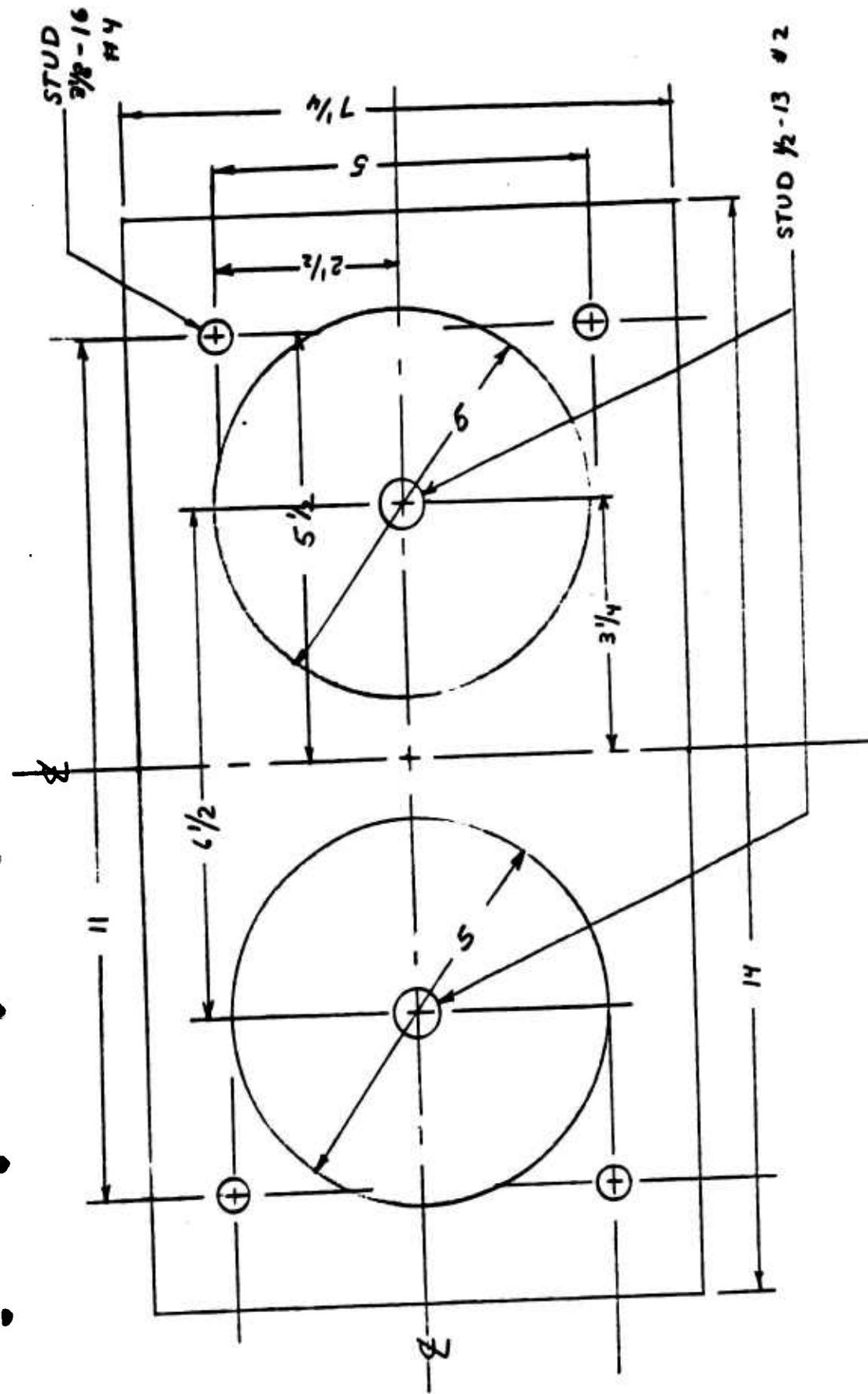
Figure 5.  Capacitor Layout
Scale: one half
Capacitor: Aerovox Type No. PX80D18
29 μf, 20 kV, 5.8 kJ

13
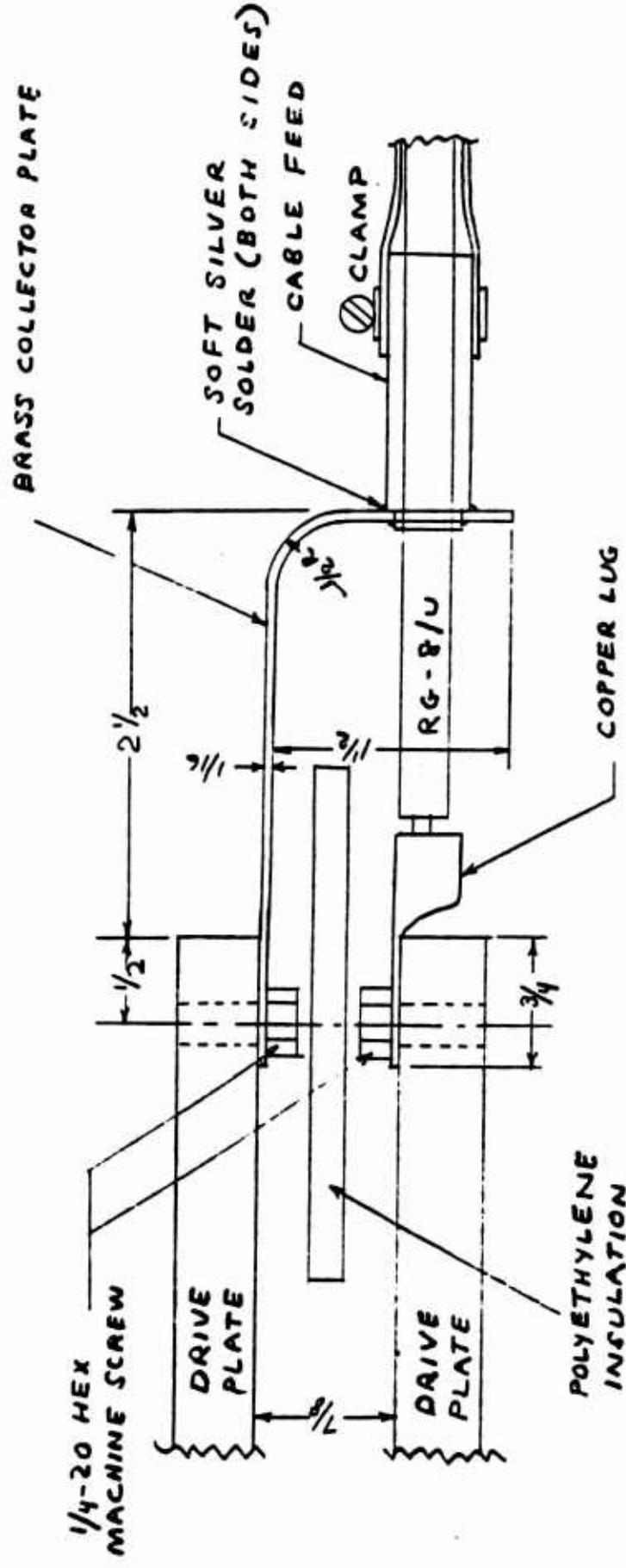
Figure 6.  Module Cable Feed Assembly
Scale:  full size

14
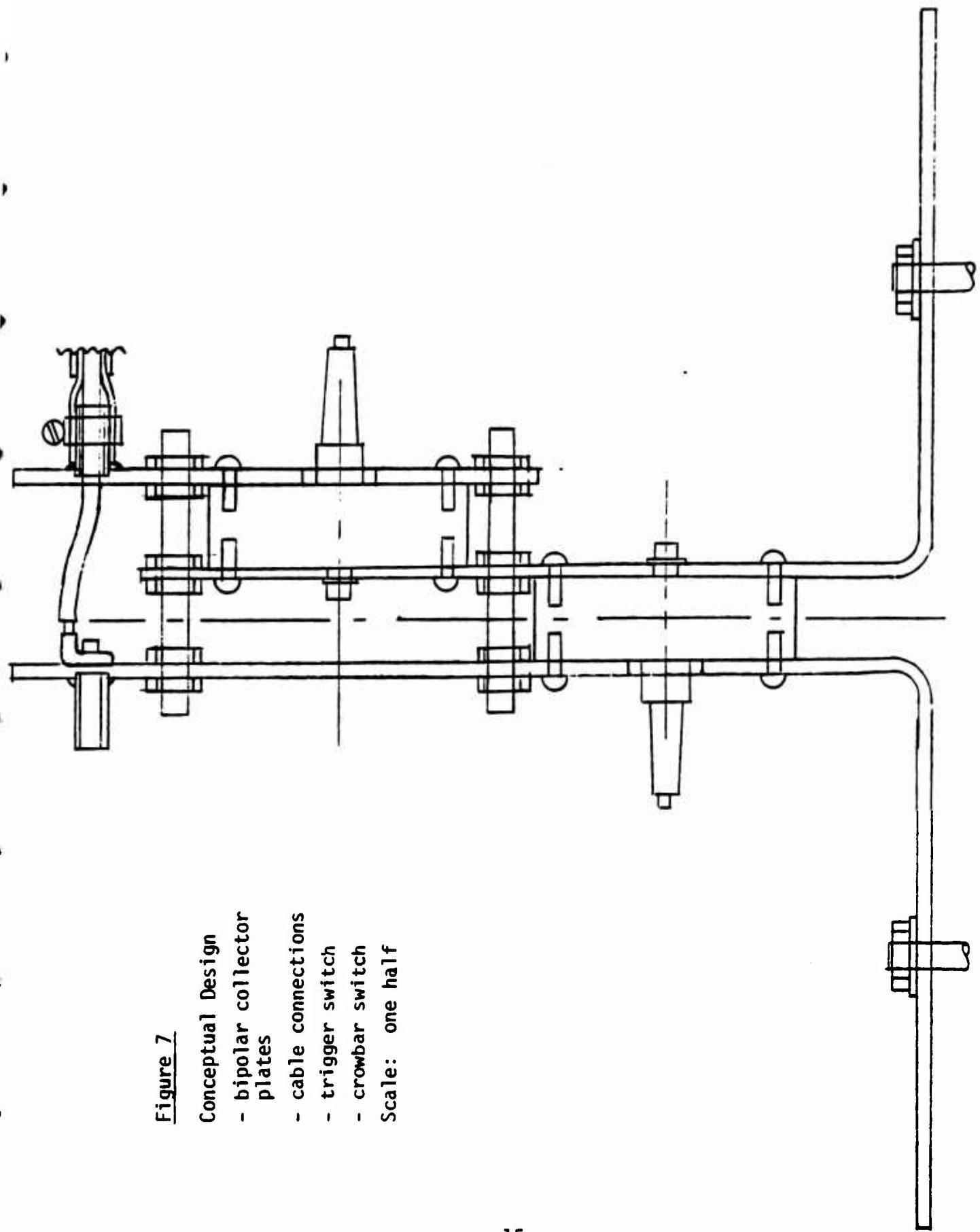
Figure 7

Conceptual Design

- bipolar collector plates
- cable connections
- trigger switch
- crowbar switch

Scale: one half

15
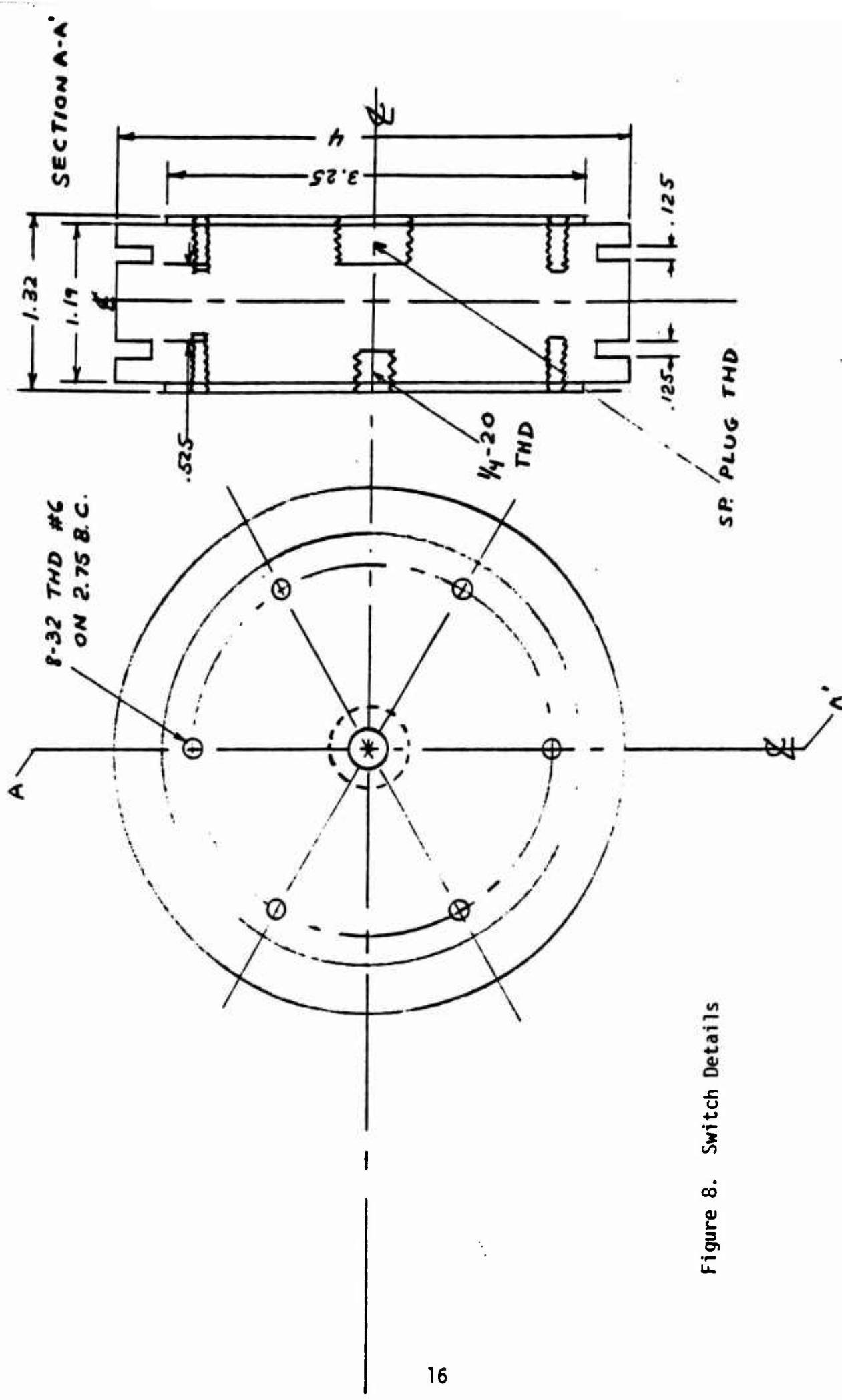
Figure 8. Switch Details

16
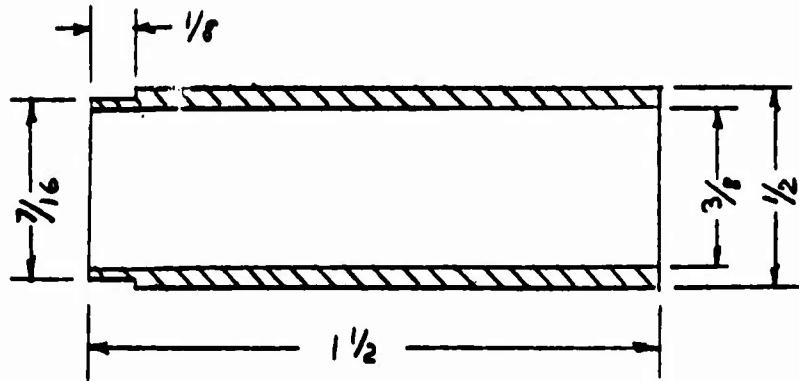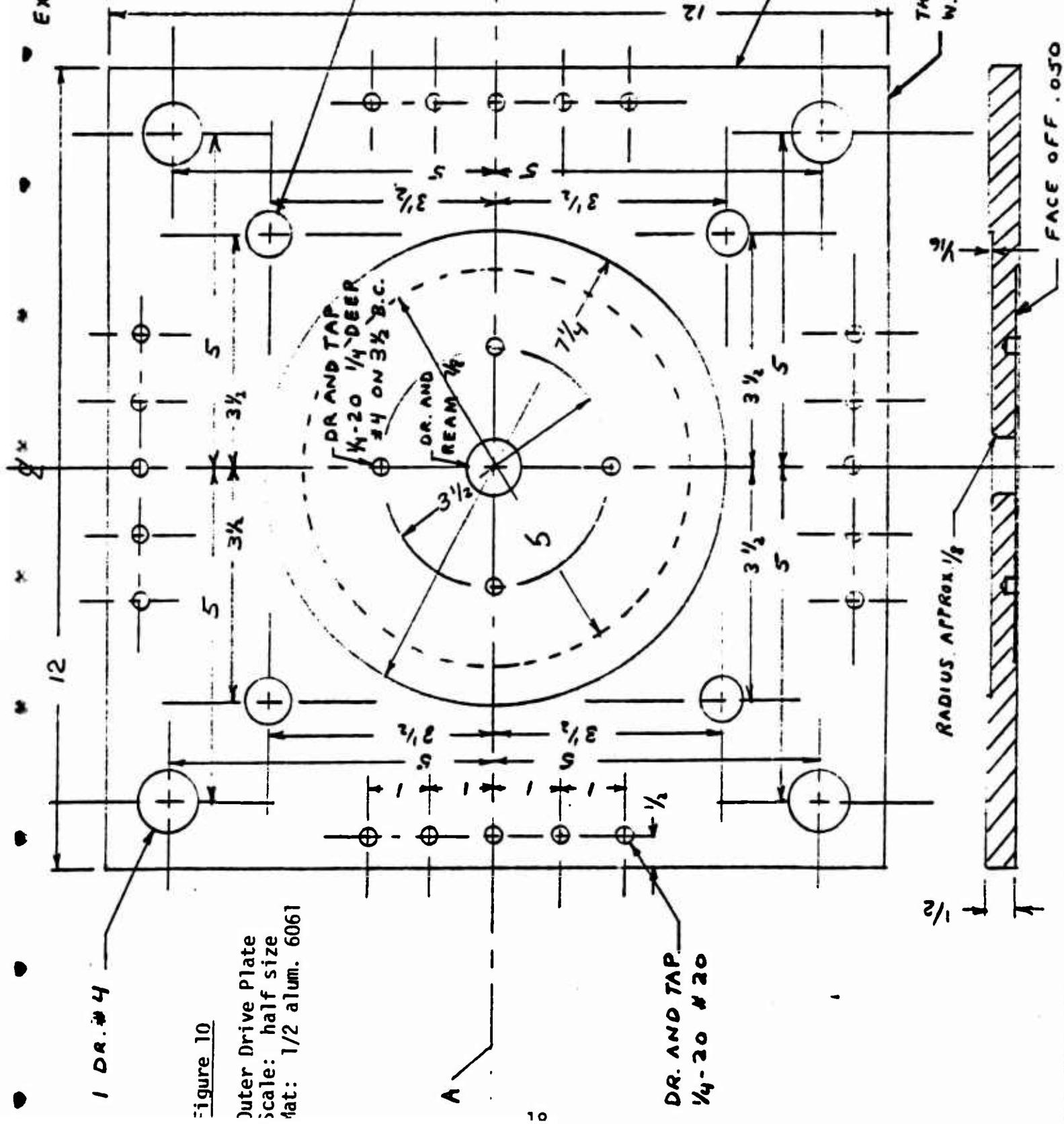
Figure 9. Cable Feed
Scale: 2:1
Mat: brass tubing

Figure 10

Outer Drive Plate
Scale: half size
Mat: 1/2 alum. 6061

NOTE: ALL HOLES
EXCEPT OUTER 1/4-20
LOCATED W.R.T. ℄
(THEY CAN BE
ALSO BUT NOT
REQUIRED)

NOTE: ON TWO
PLATES: DR. AND TAP
3/8 NC #4 — ON
REMAINING TWO
PLATES: DR 3/4 #4

SAW CUT AND
SAND REMAINING
3 EDGES

THIS EDGE ONLY: LOCATE
W.R.T. ℄ AND END MILL

SECTION A-A'

5 IN. DIA.

FACE OFF .050

RADIUS APPROX 1/8

DR. AND TAP
1/4-20 1/4 DEEP
#4 ON 3 1/2 B.C.

DR. AND
REAM 1/4

DR AND TAP.
1/4-20 #20

1 DR.#4
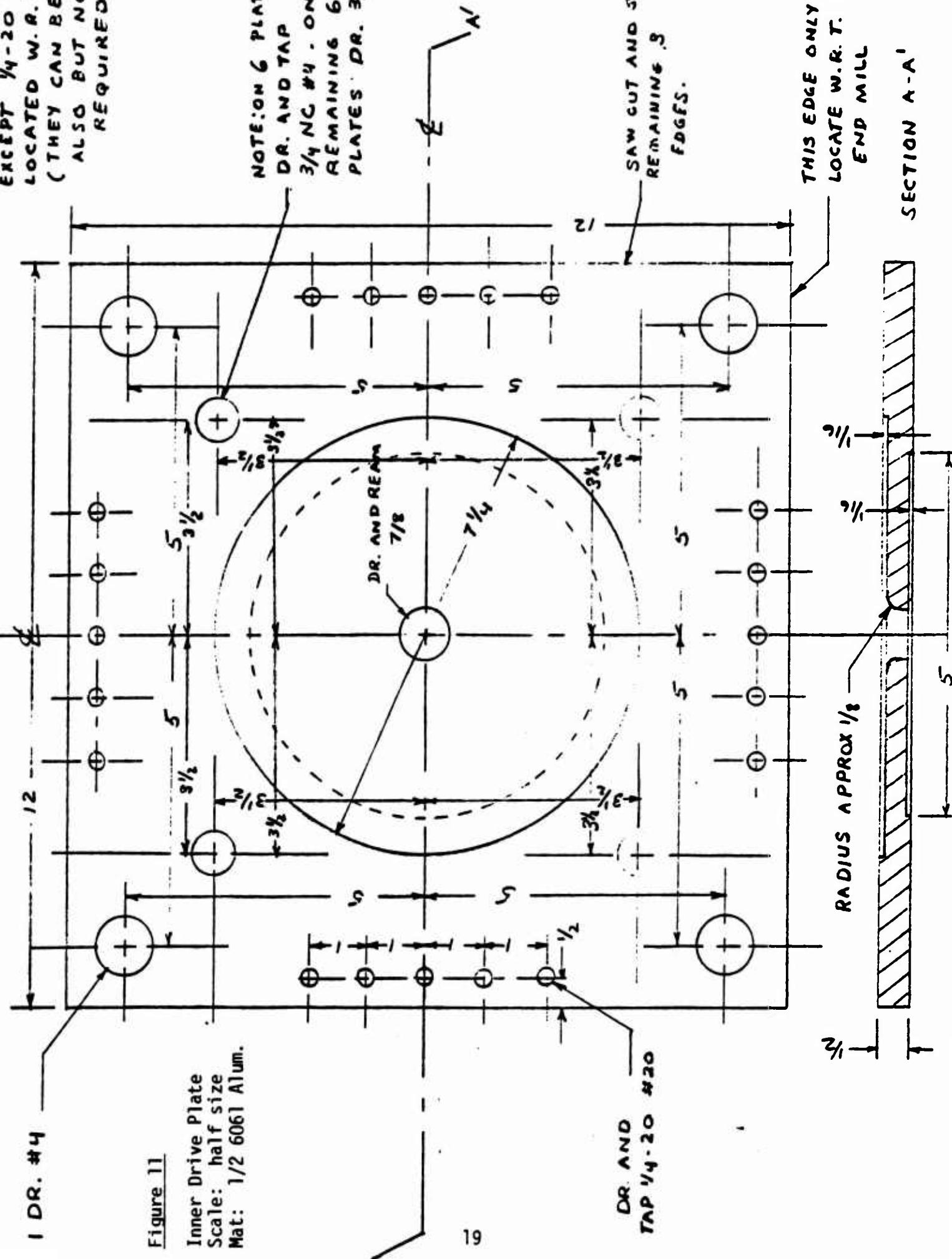
Figure 11

Inner Drive Plate
Scale: half size
Mat: 1/2 6061 Alum.

NOTE: ALL HOLES
EXCEPT 1/4-20
LOCATED W.R.T. ℄
(THEY CAN BE
ALSO BUT NOT
REQUIRED)

NOTE: ON 6 PLATES
DR. AND TAP
3/4 NC #4. ON
REMAINING 6
PLATES DR. 3/4 #

DR. AND REAM 7/8

1 DR. #4

1 DR. #4 LOCATE W.R.T. ℄

DR. AND
TAP 1/4-20 #20

SAW CUT AND SAND
REMAINING 3
EDGES.

THIS EDGE ONLY:
LOCATE W.R.T. ℄
END MILL

RADIUS APPROX 1/8

SECTION A-A'

19
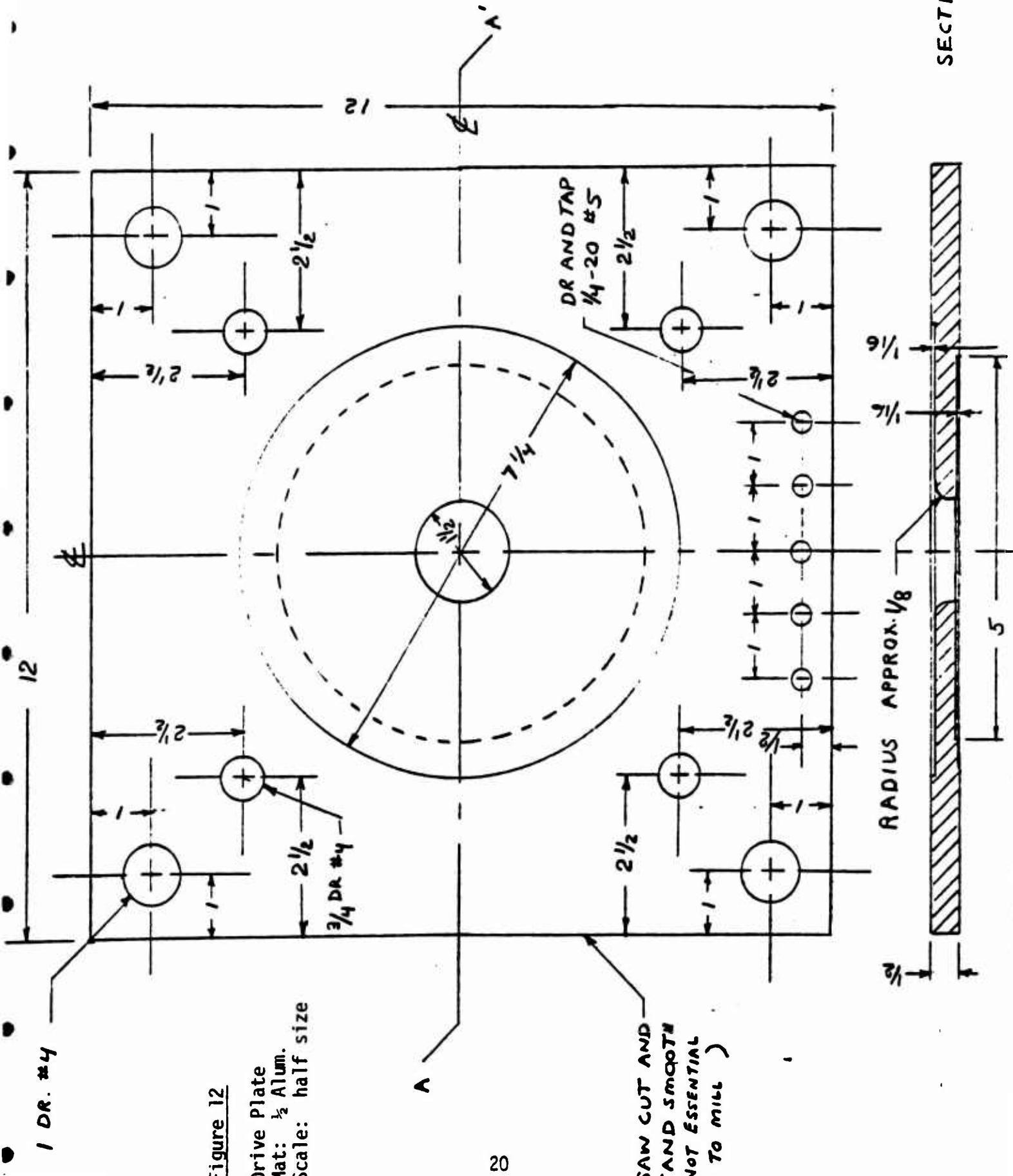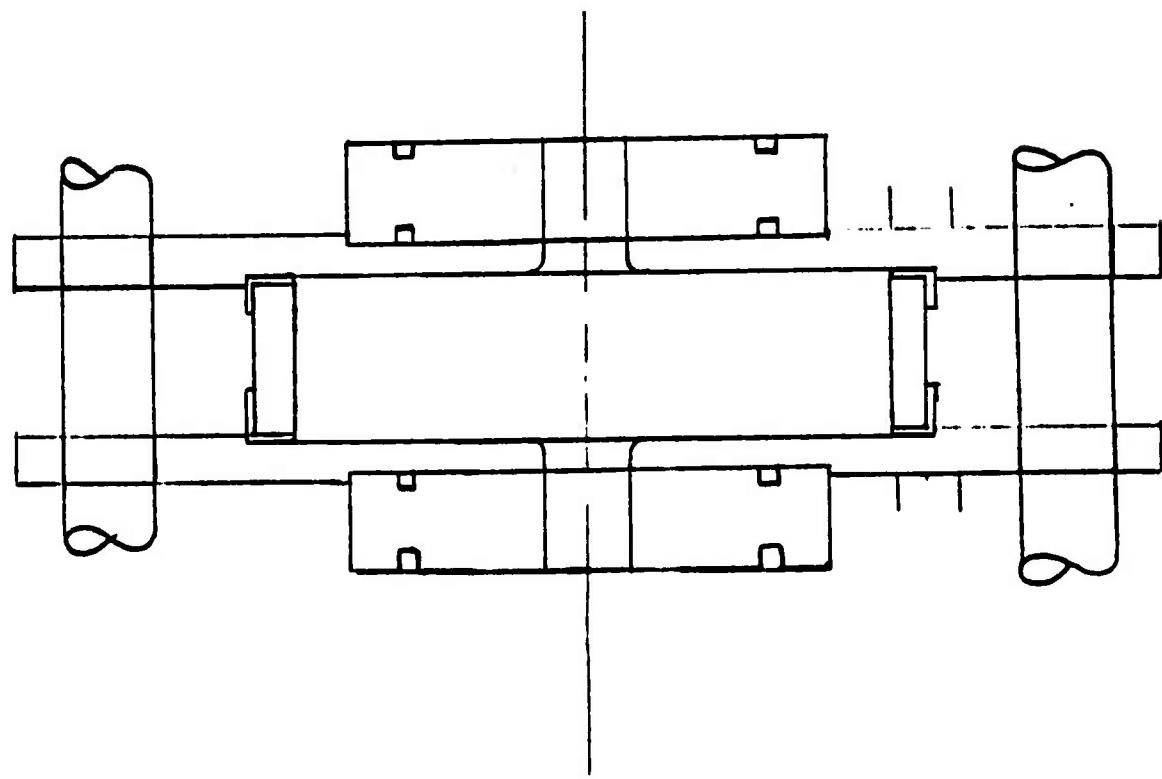
Figure 12

Drive Plate
Mat: ½ Alum.
Scale: half size

SECTION A-A'

DR. AND TAP
¼-20 #5

RADIUS APPROX. ⅛

SAW CUT AND
SAND SMOOTH
(NOT ESSENTIAL
TO MILL)

1 DR. #4

¾ DR #4

20

Figure 13. Intermodule Assembly
Scale: one half
(approx.)

21

STD. O-RING GROOVE FOR $3\frac{3}{4} \times 4$ O-RING

DR. AND REAM $\frac{7}{8}$

$\phi$

$\frac{7}{16}$

$2\frac{1}{2}$

$1$
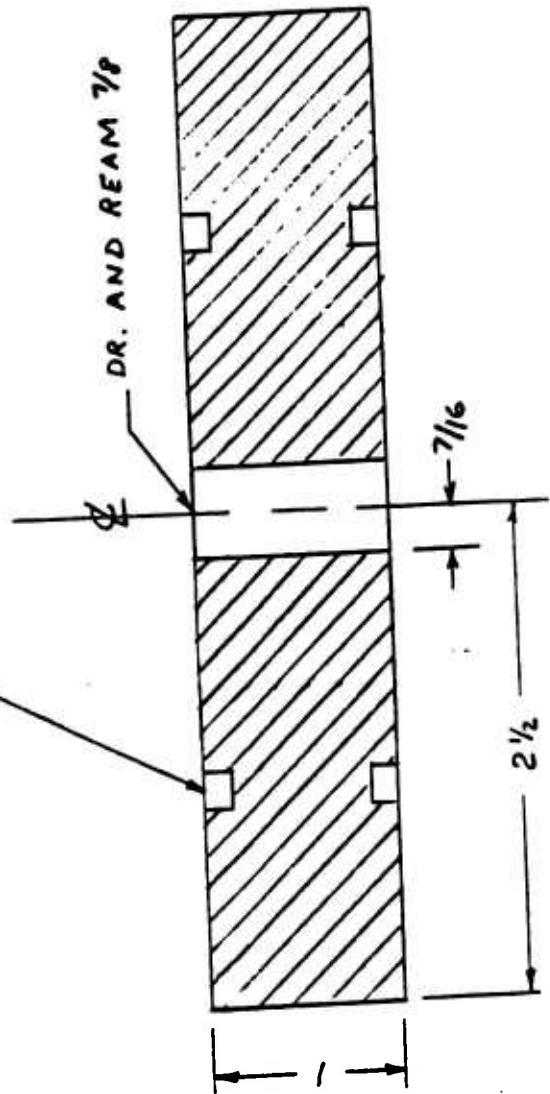
Figure 14.   Intermodule Spacer
Scale:   full size
Mat:   lucite

GRIND SQUARE

GRIND SQUARE

6 1/4

7

1

℄
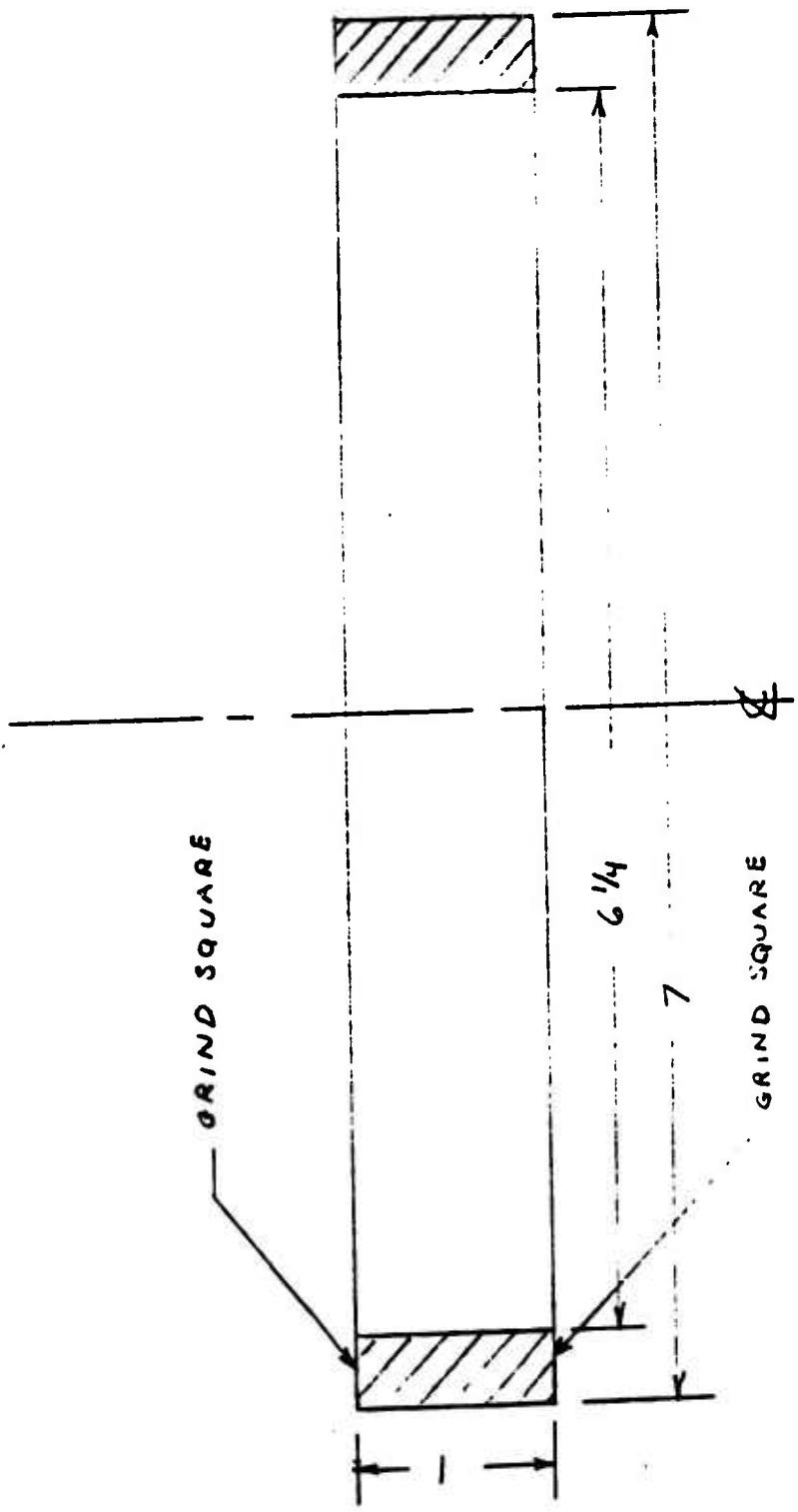
Figure 15.   Launch Wall
            Scale:  full size
            Mat:  Pyrex

For smaller module radii use thicker
lucite wall.  Azimuthal sharp breakdown
ring at inner edge of launch wall may also
also be used to assist in implosion
symmetry.
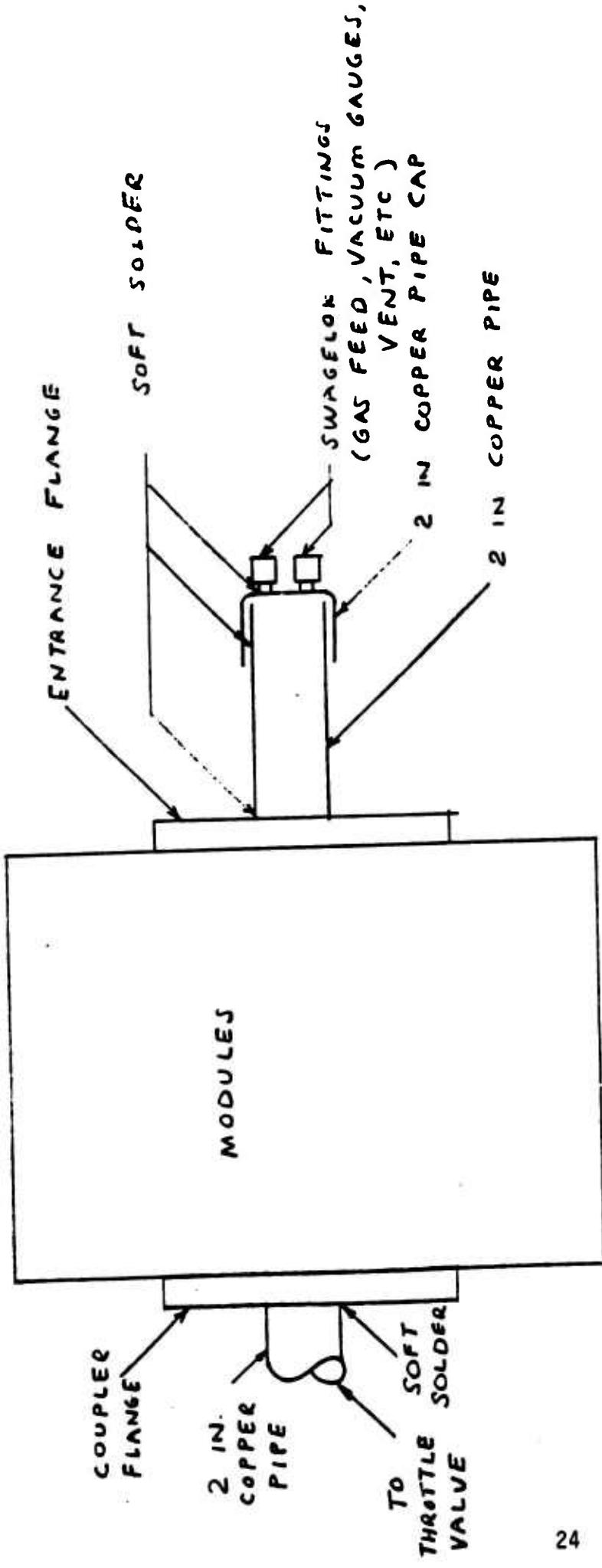
Figure 16.   Vacuum Connections

24
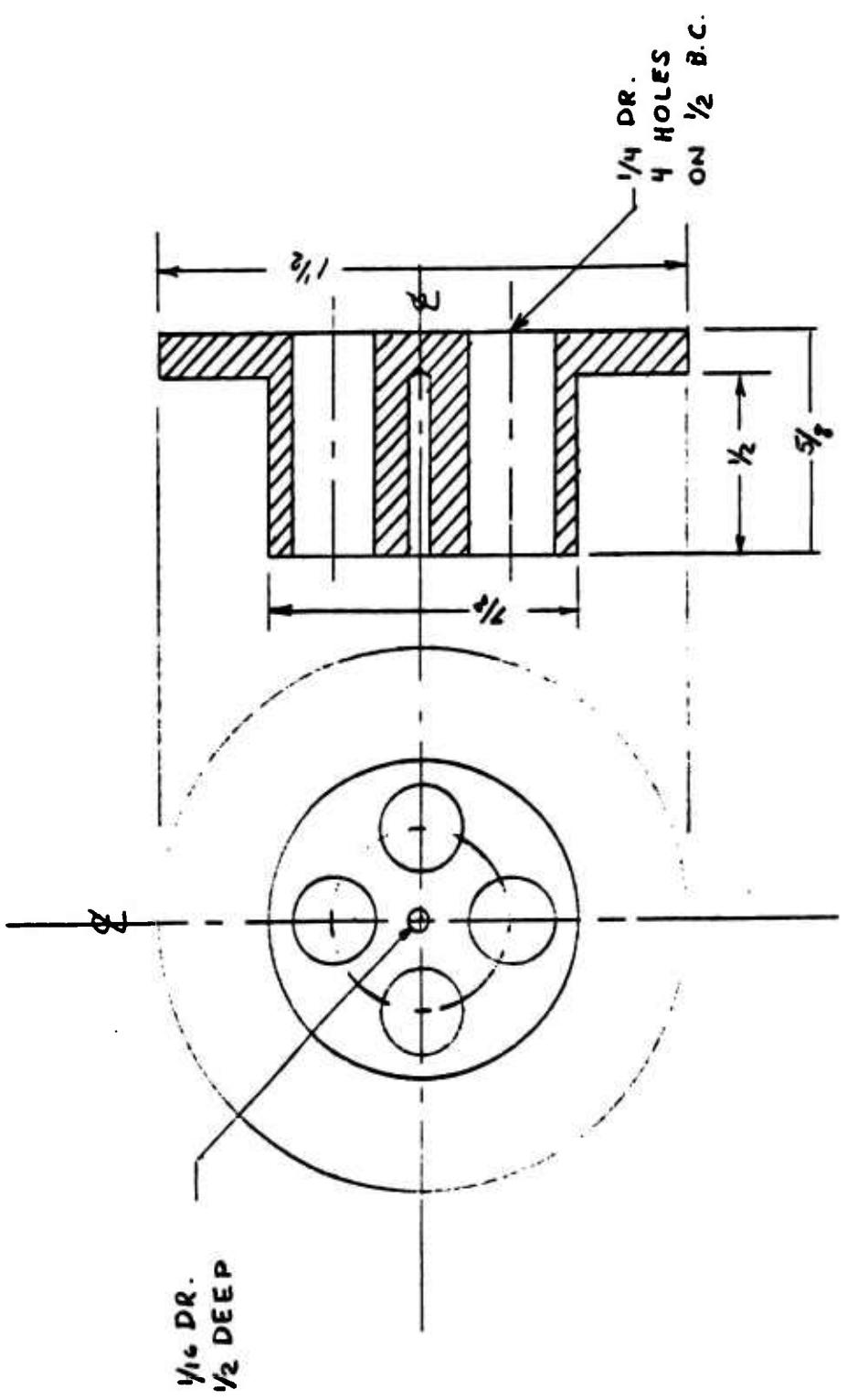
Figure 17. Projectile Support
Scale: 2:1
Mat: Alum.

25
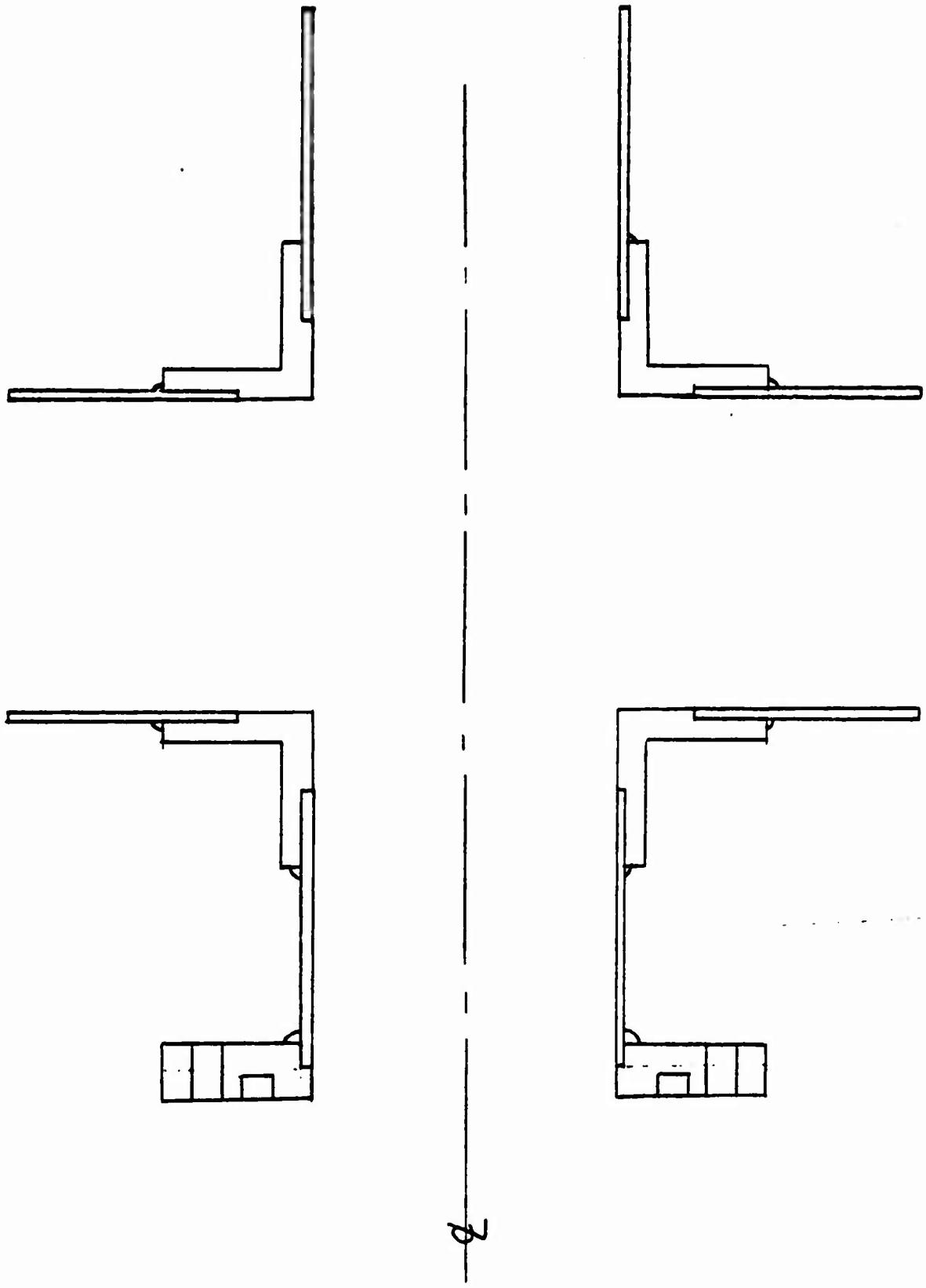
Figure 18.  Coupling Assembly
Scale:  full size
Mat:  brass
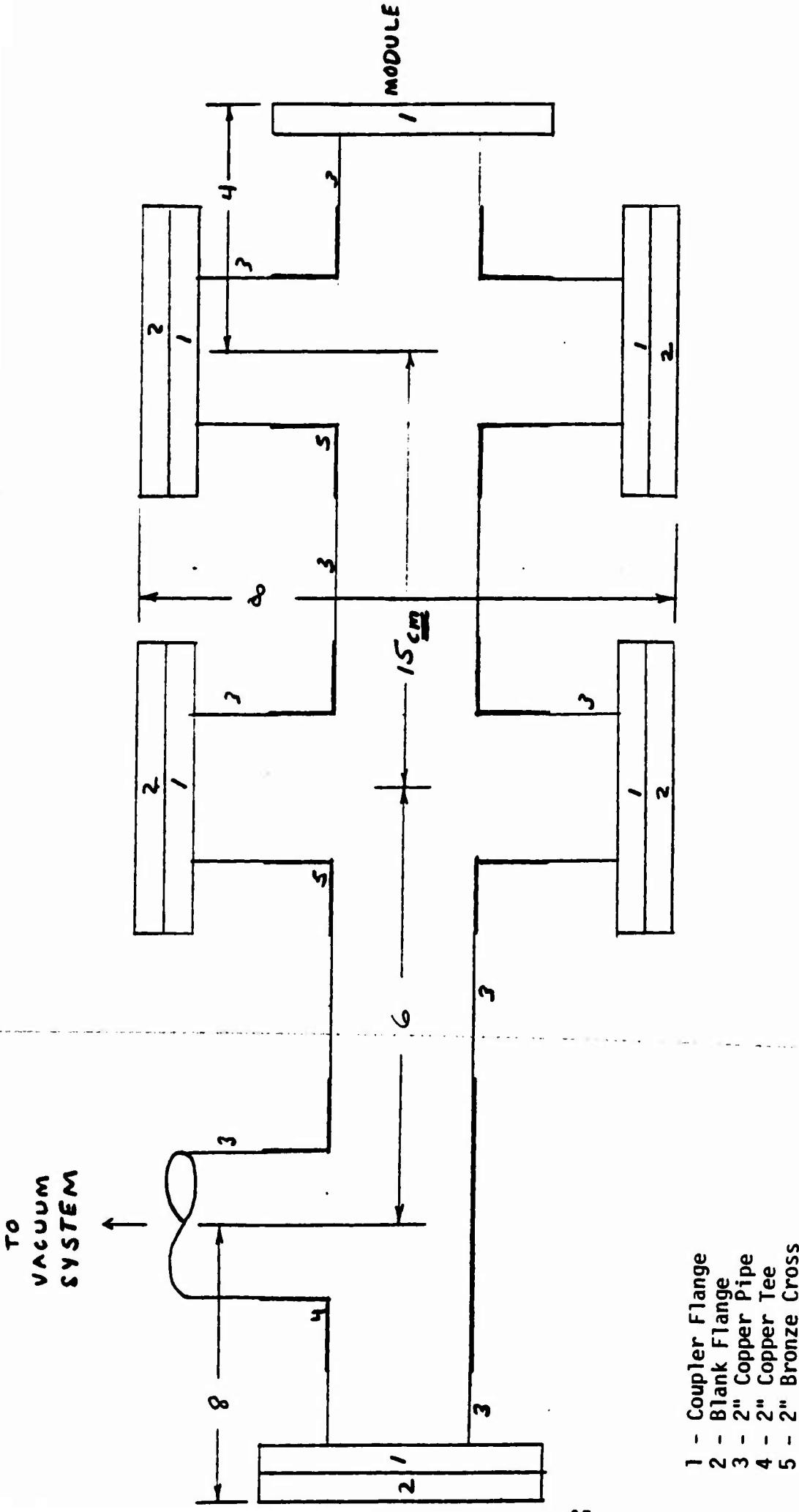
Figure 19. Diagnostic Exit Part Assembly (not to scale)

MODULE

TO VACUUM SYSTEM

15 cm

- SOFT SILVER SOLDER ALL JOINTS

1 - Coupler Flange
2 - Blank Flange
3 - 2" Copper Pipe
4 - 2" Copper Tee
5 - 2" Bronze Cross

27

DR TO CLEAR ¼-20
4 HOLES ON 3½ B.C.

STD O-RING GROOVE
FOR 2¾ x 3 O-RING

$h$

⅜
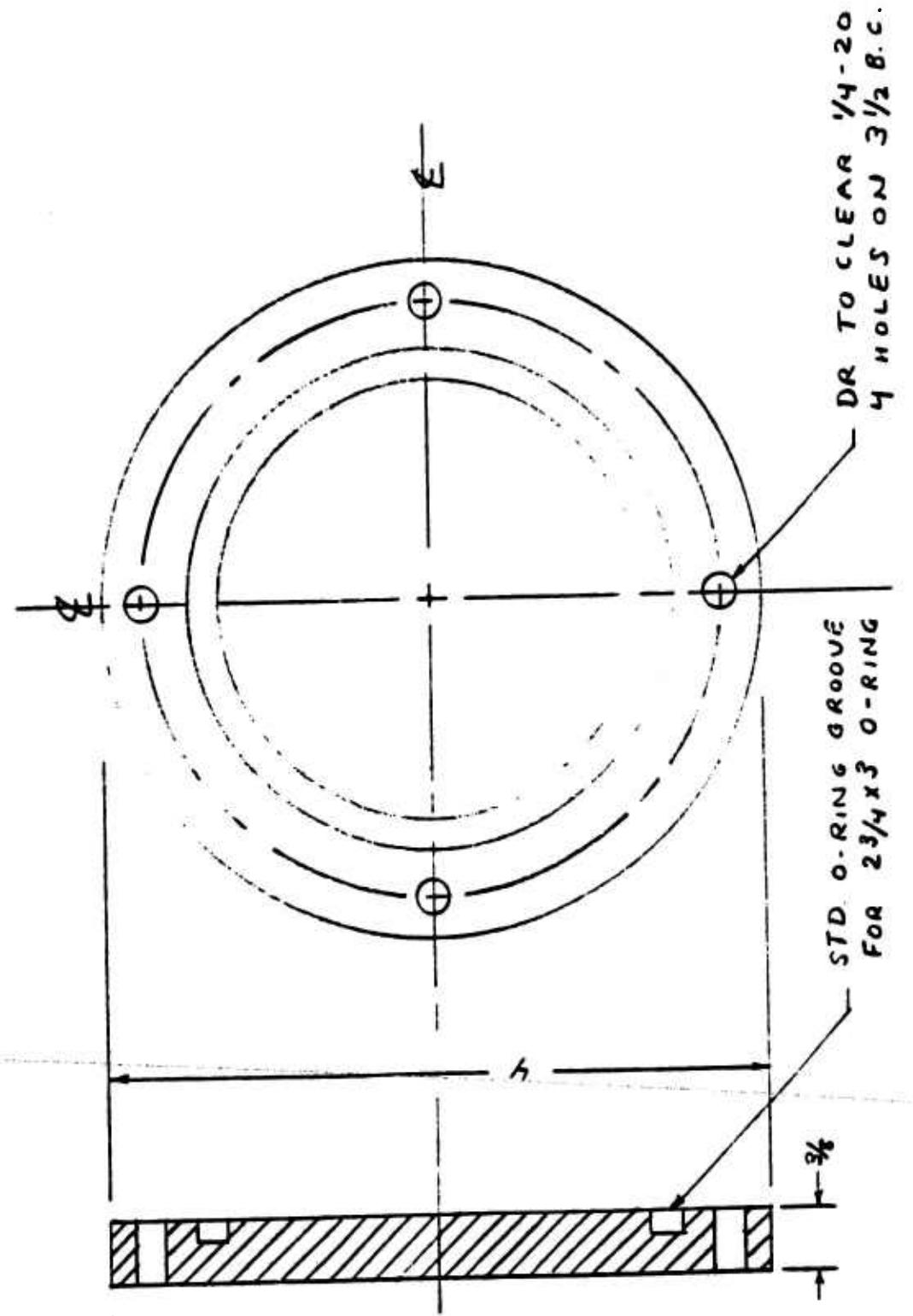
Figure 20. Blankoff Flange for Module Pumpdown and Testing
Scale: full size
Mat: Brass

28

DR. TO CLEAR 1/4-20
#4 ON 3 1/2 B.C.

STD. O-RING GROOVE
FOR 2 3/4 x 3 O-RING
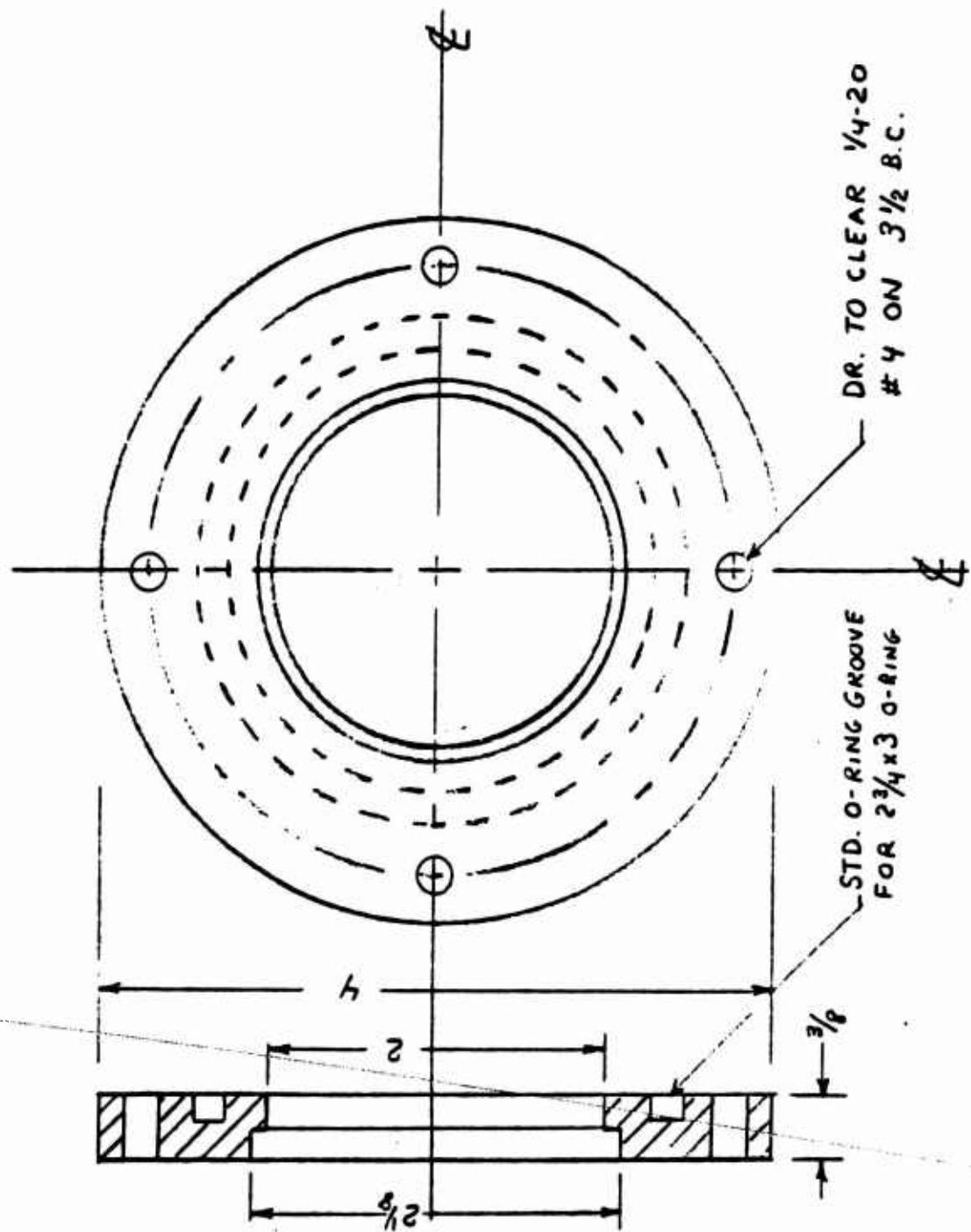
Figure 21. Coupler Flange
Scale: full size
Mat: brass
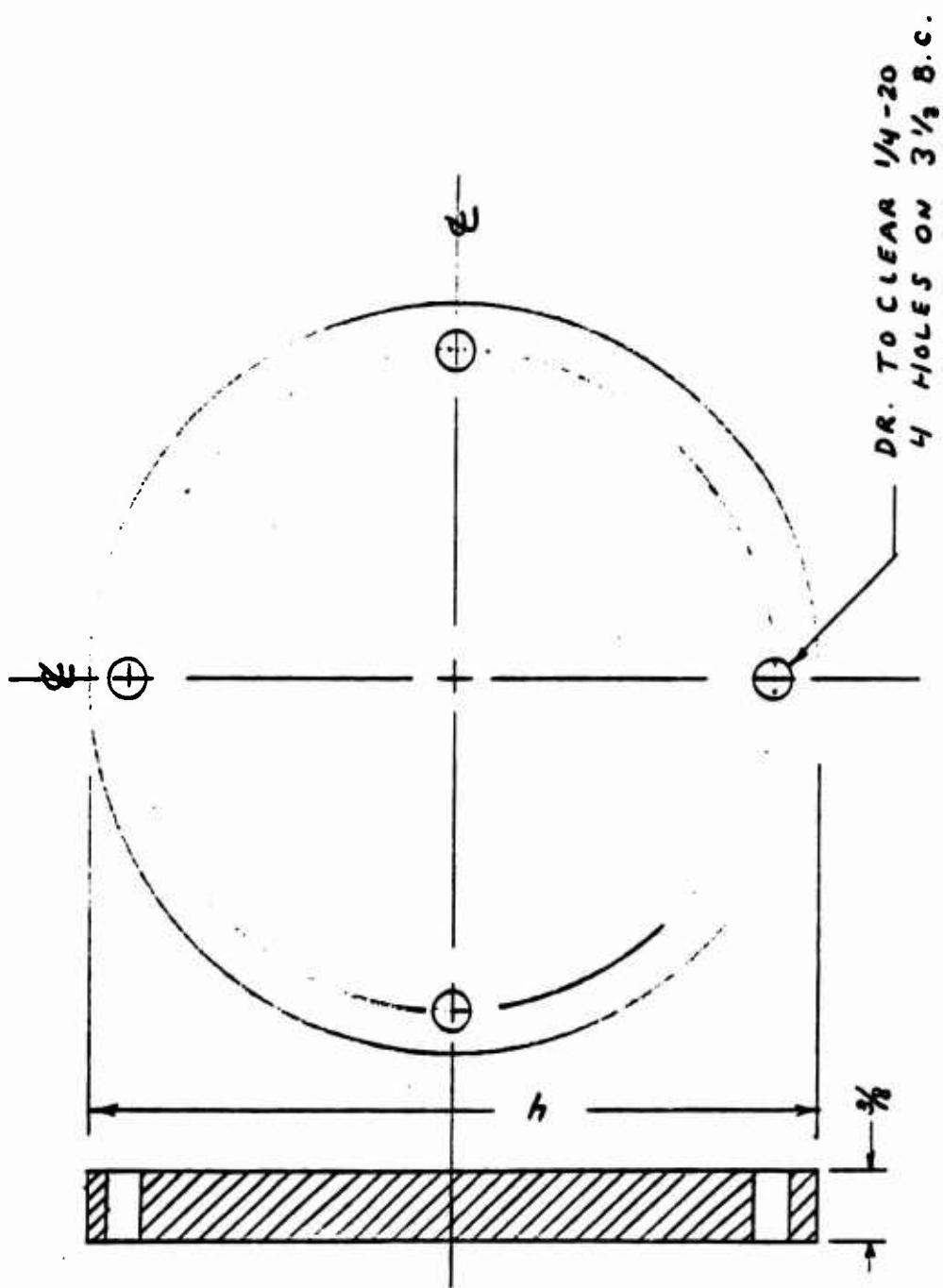
Figure 22. Blank Flange
Scale: full size
Mat: brass
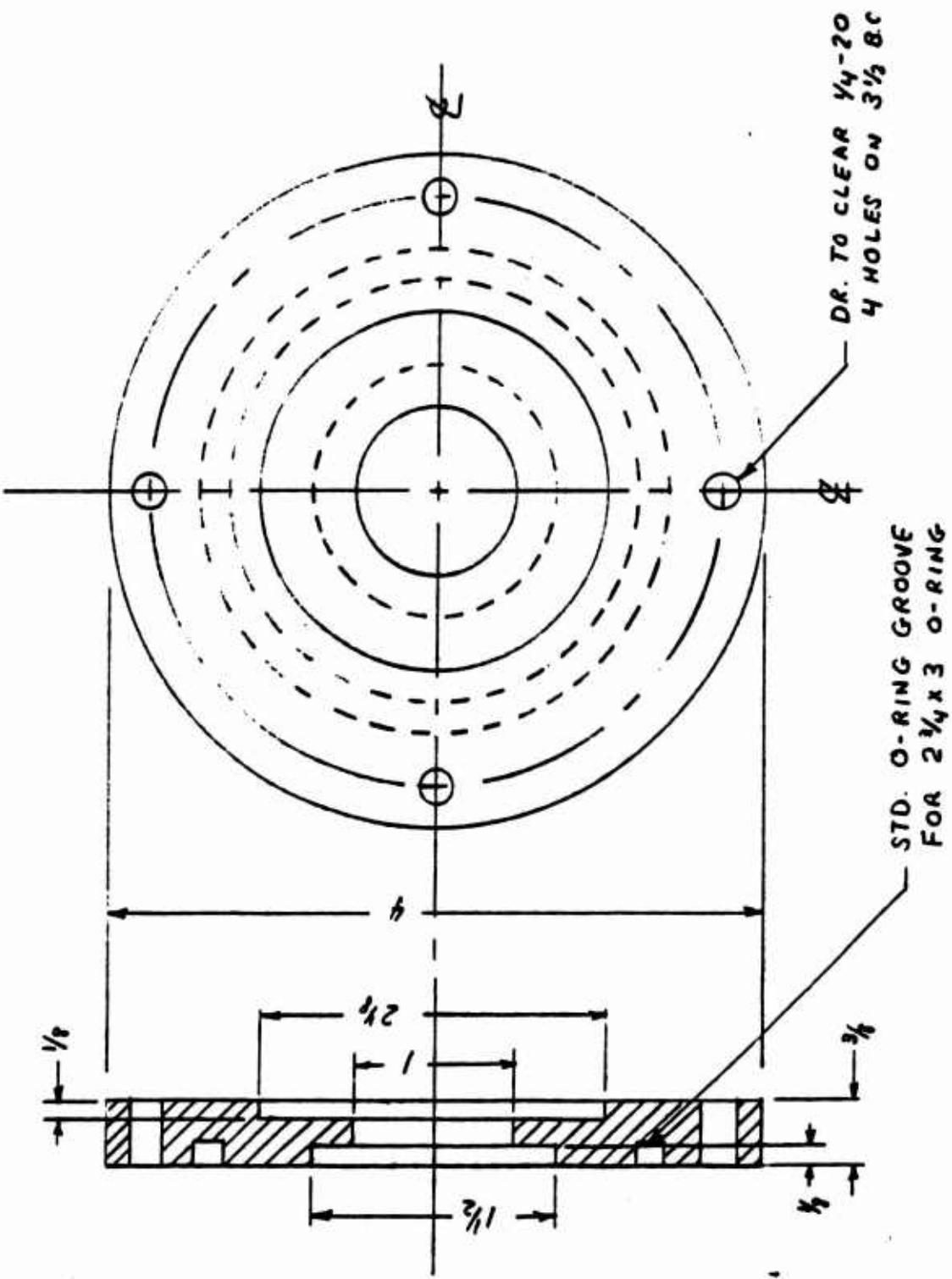
Figure 23. Entrance Flange
Scale: full size
Mat: brass

31

DR. AND TAP ¼-20
#4 ON 3½ B.C.
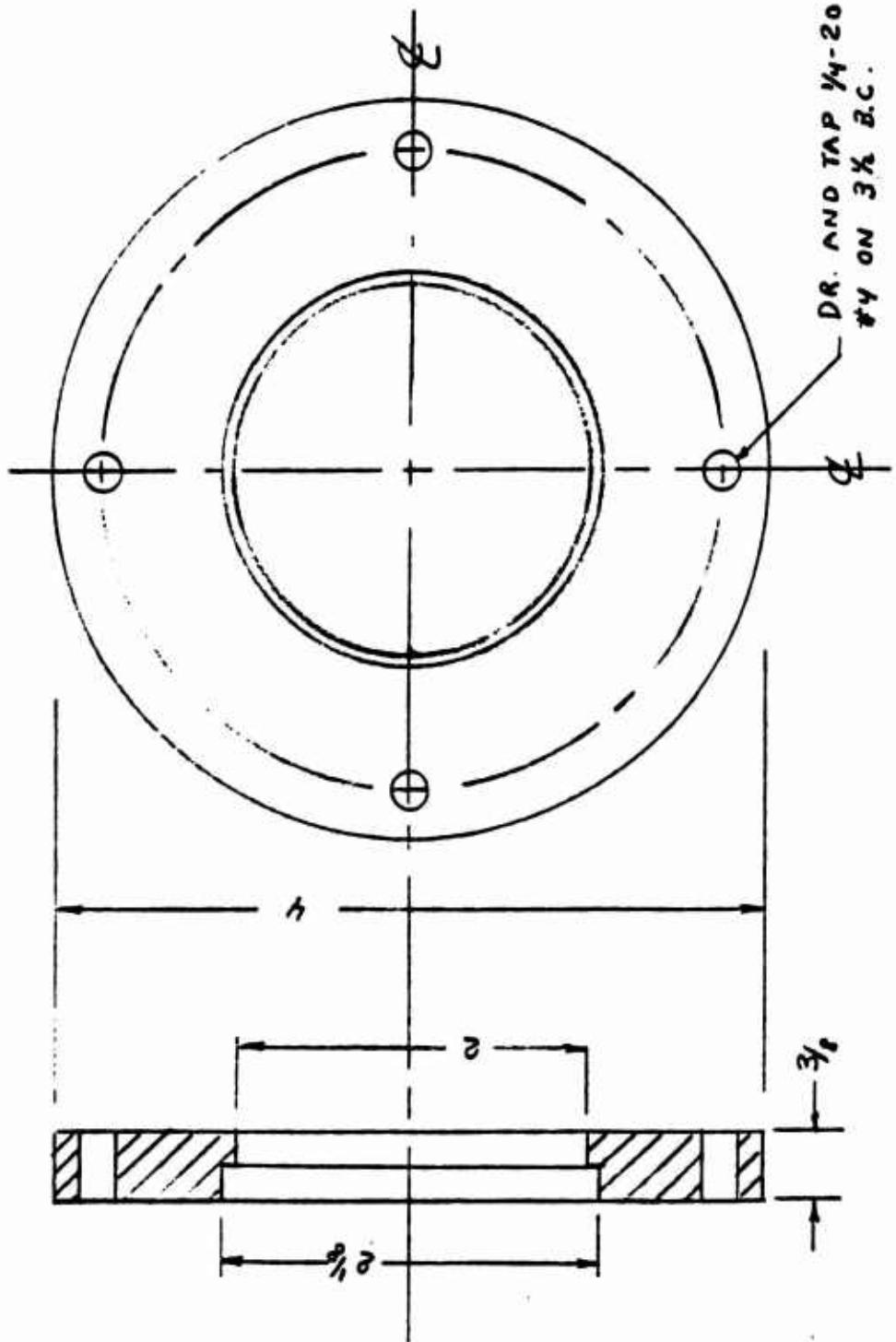
Figure 24. Cover Flange.
Scale: full size
Mat: brass
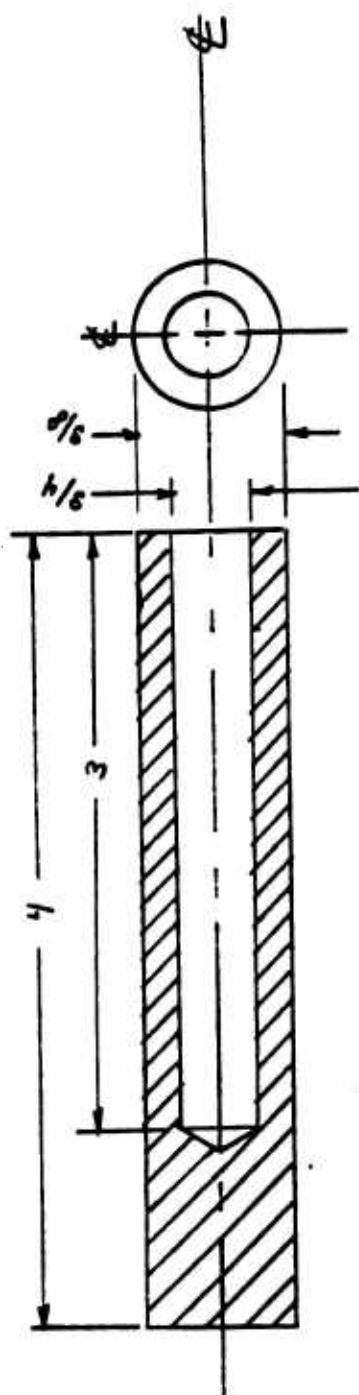
Figure 25.  Casing for Magnetic Pickup
Scale:  full size
Mat:  Lucite
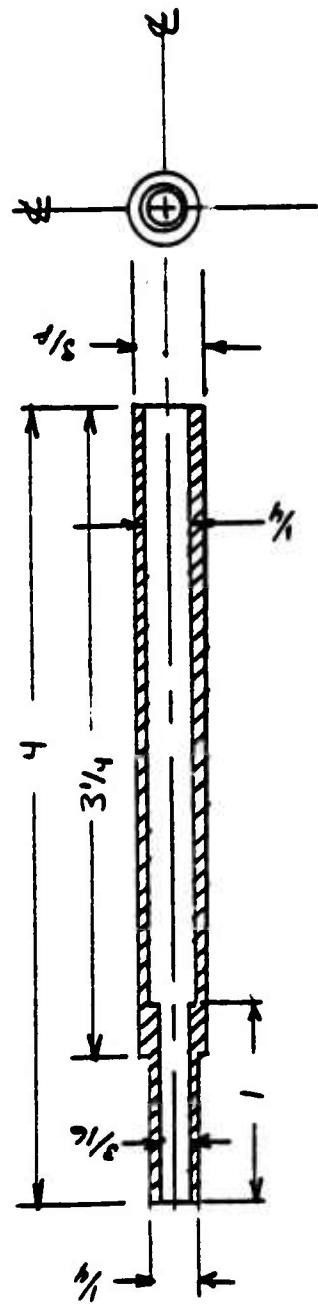
Figure 26.   Magnetic Pickup Insert
Scale:  full size
Mat:  Lucite
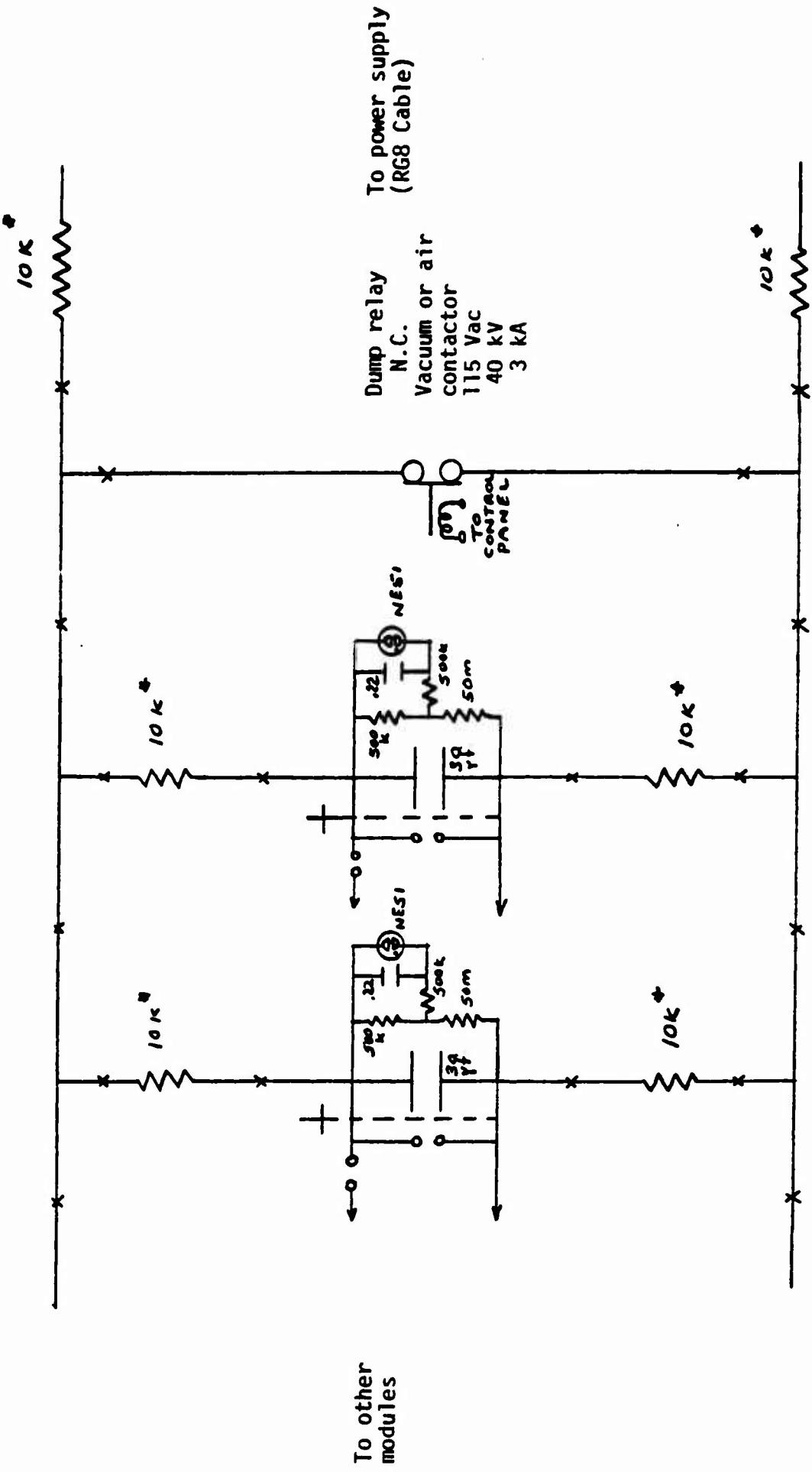
Figure 27. Module charging, discharging, monitoring, and safety system. x – denotes RG8 cable with shield removed. * – 10 1k wirebound 10W in series on circuit board.

35
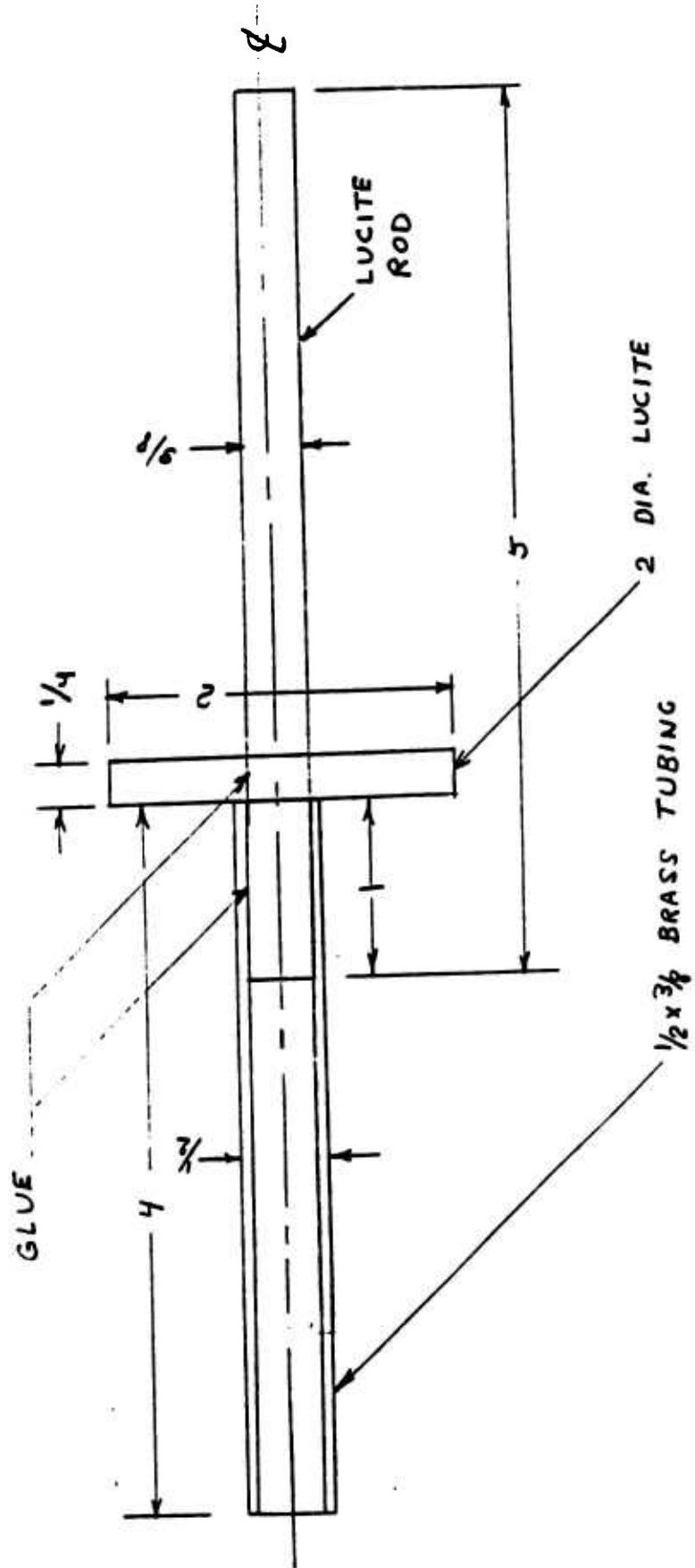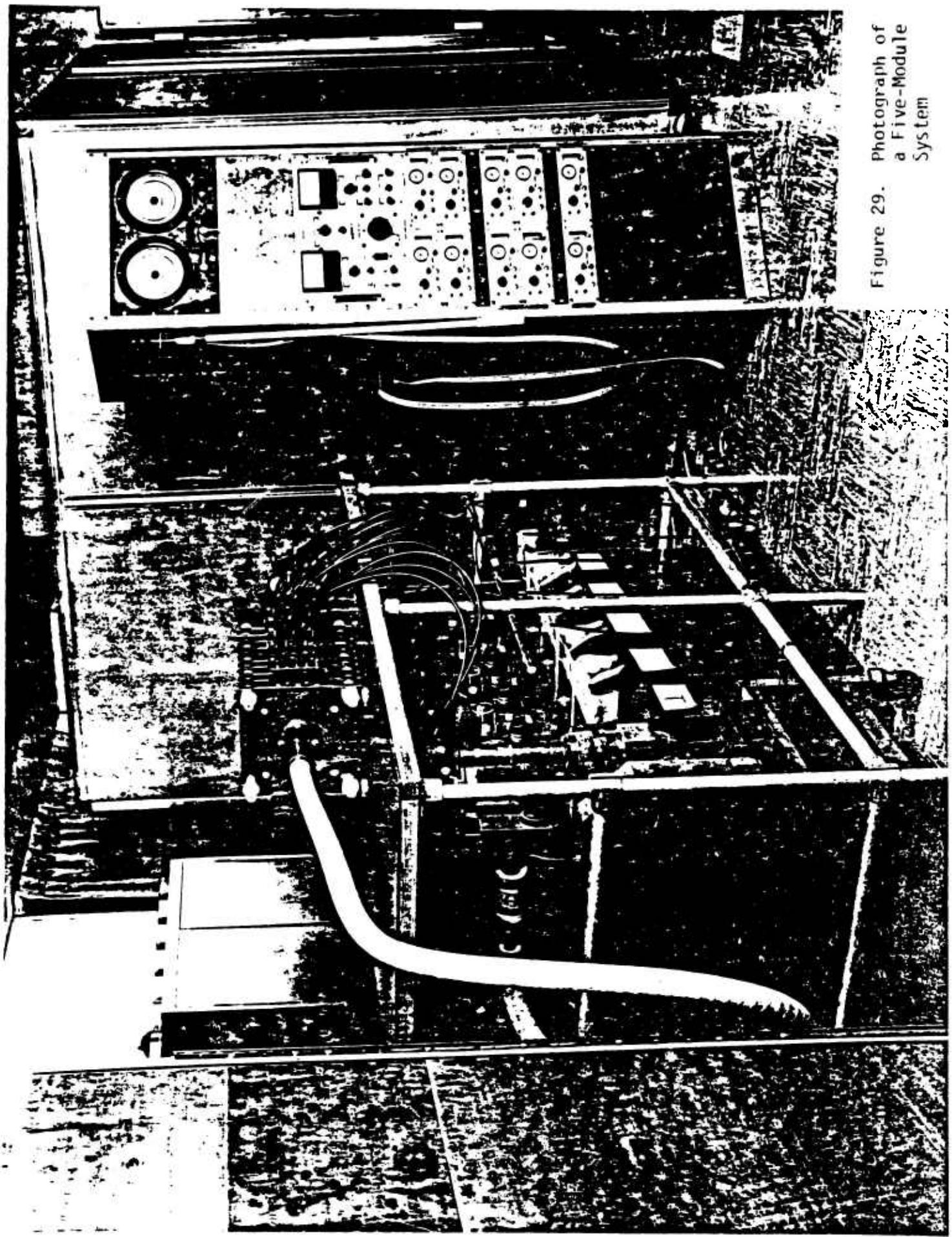
Figure 28. Shorting bar
Scale: full size
Mat: As shown

Figure 29. Photograph of a Five-Module System
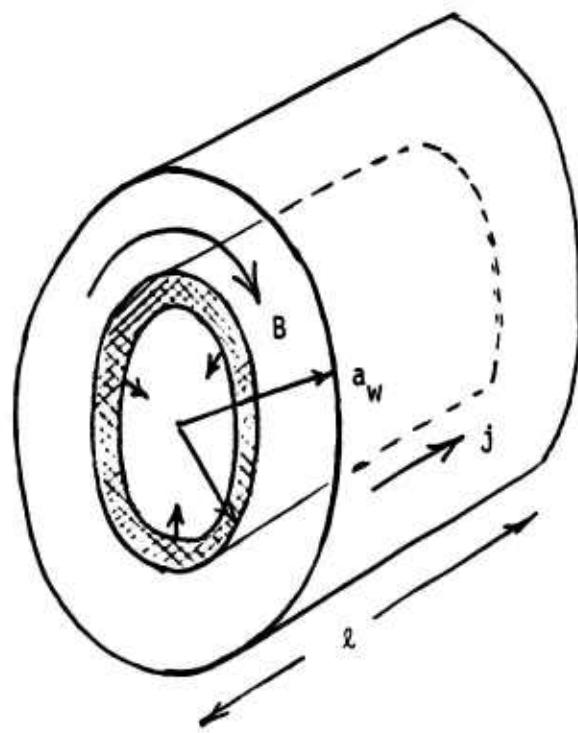
Figure 30.  Geometry of Imploding Plasma Discharge

PLOT 1
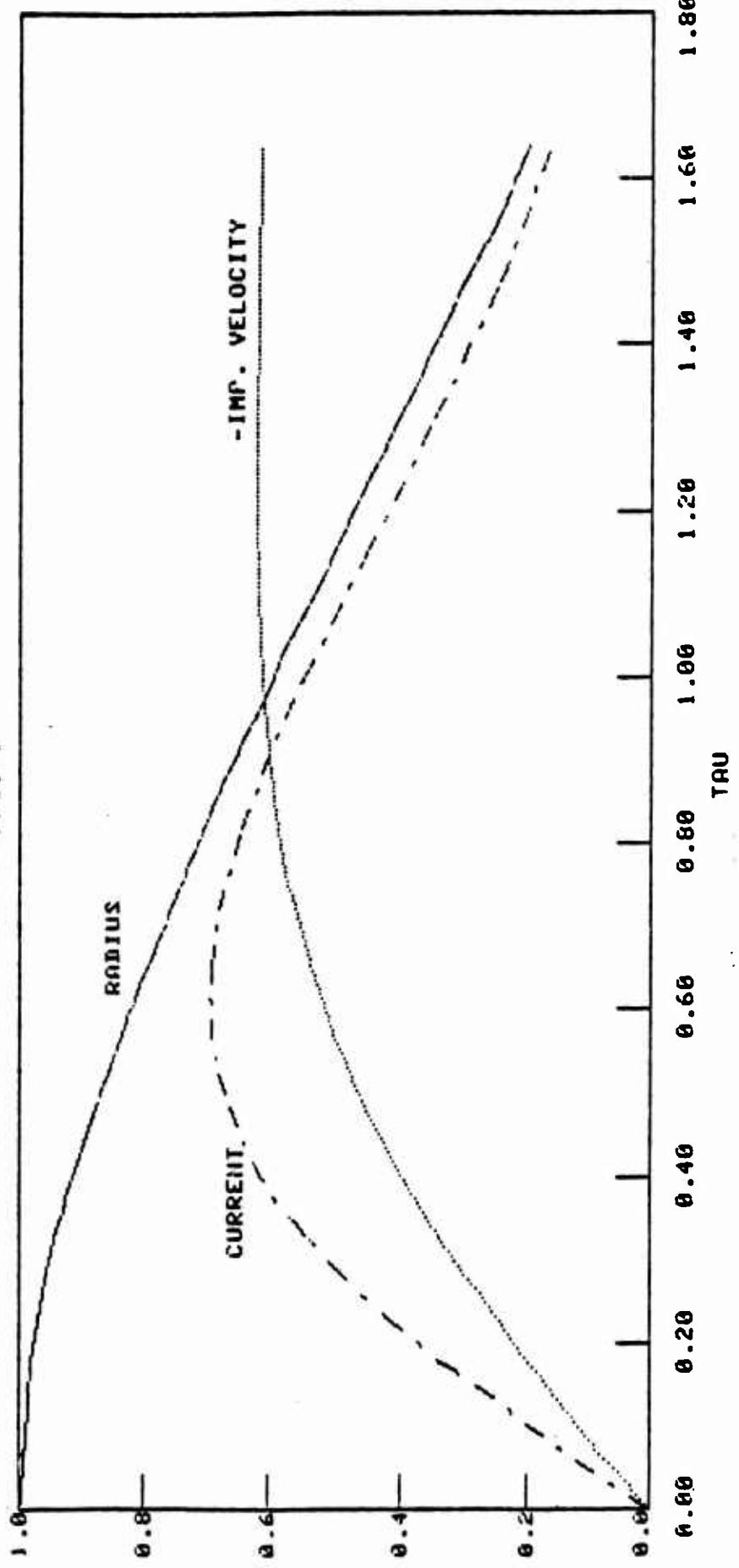


Figure 31. Plot of the dimensionless radius A, current i, and implosion velocity À as
functions of $\tau = \omega\tau$. System parameters in dimensionless units are shown in
Table 1. At $\tau = \tau_{imp} = 1.61$, the plasma radius equals the projectile radius
($a_p = 0.2$), and $\ddot{A}(\tau_{imp}) \approx 0$. Note that the current has not yet reached zero.

39
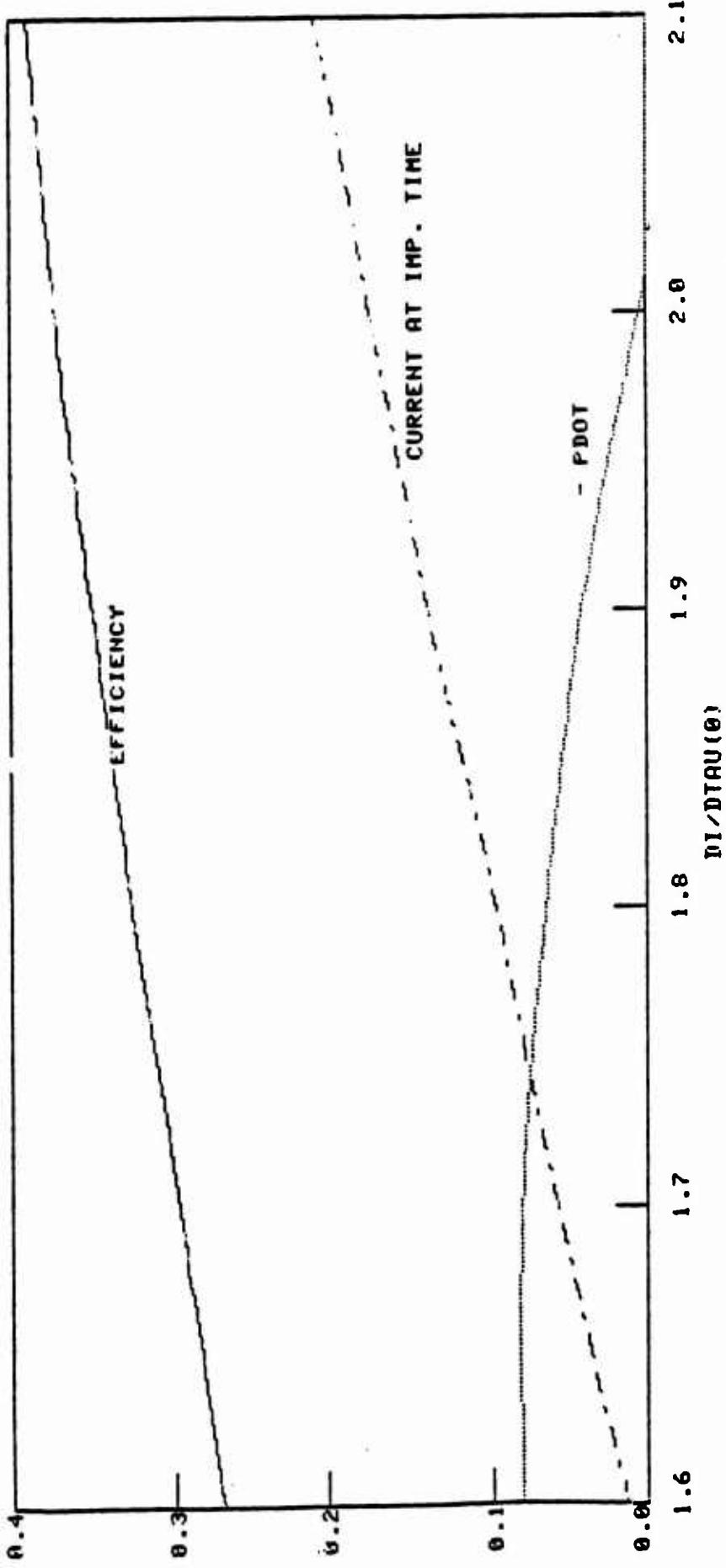
Figure 32. Plot of efficiency ε, current $i(\tau_{imp})$, and $-\ddot{A}(\tau_{imp})$ versus the initial current derivative $\frac{di}{d\tau}(0)$. Other parameters are as in Table 1. As $\frac{di}{d\tau}(0)$ increases, efficiency rises but the strength of the stabilizing potential well (which scales with $\ddot{A}(\tau_{imp})$) decreases.

40
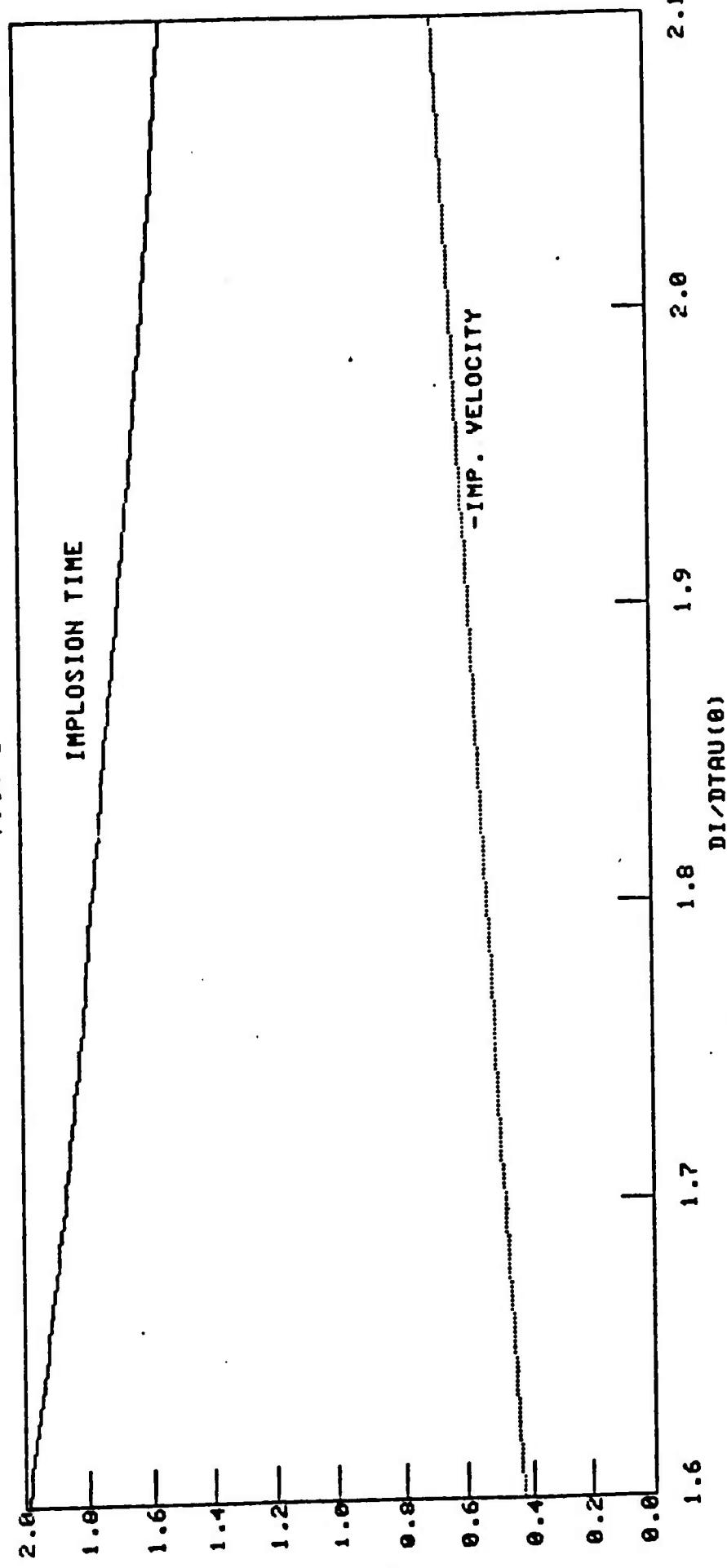
Figure 33. Variation in implosion time $\tau_{imp}$ and implosion velocity $\frac{dA}{d\tau}$ ($\tau_{imp}$) with the initial derivative in the current.

41
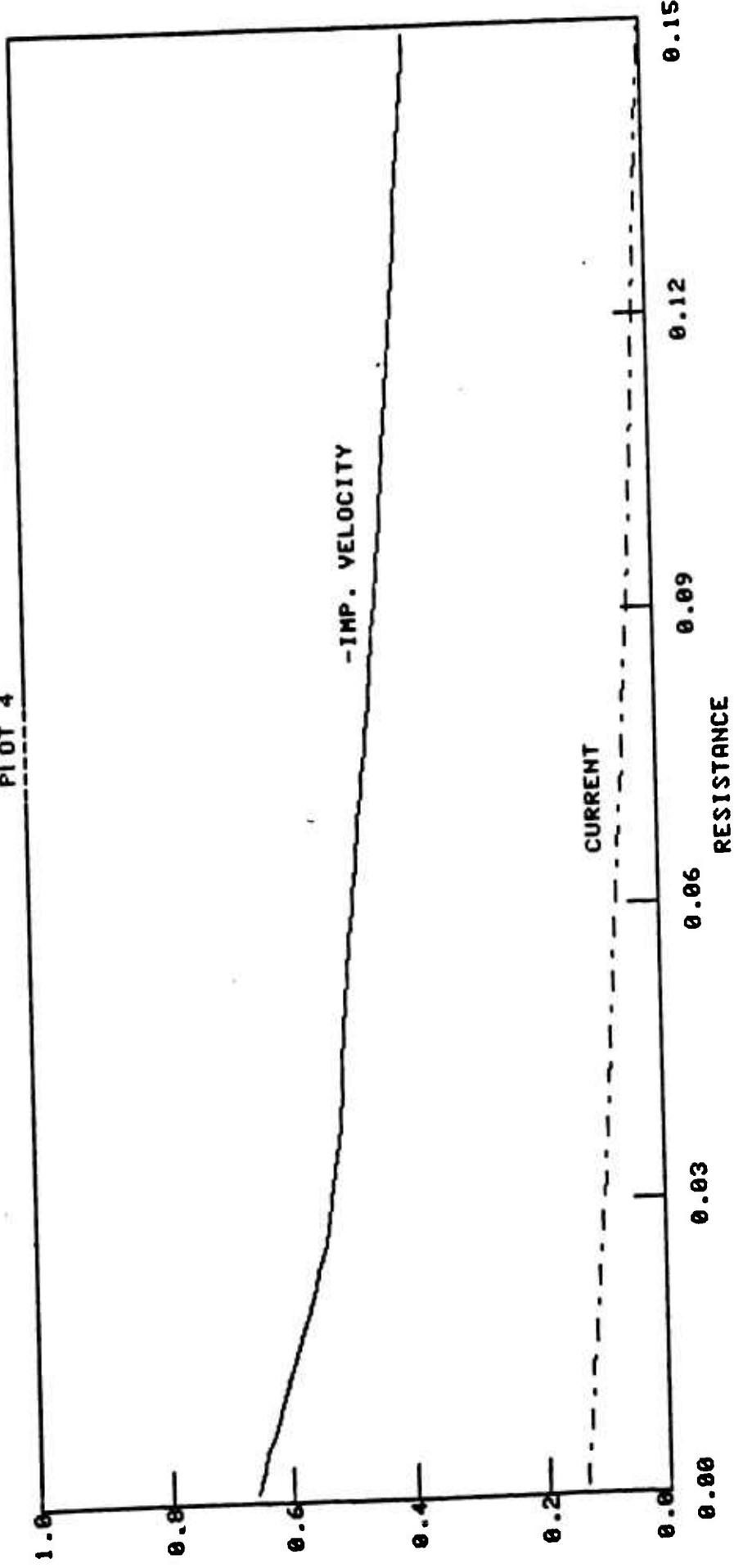
Figure 34. Variation of current $i(\tau_{imp})$ and implosion velocity $\frac{dA}{d\tau}(\tau_{imp})$ versus the dimensionless resistance r. Increasing r lowers current and implosion velocity (and hence efficiency), although some of the energy may be recovered in the form of $I^2R$ heating.
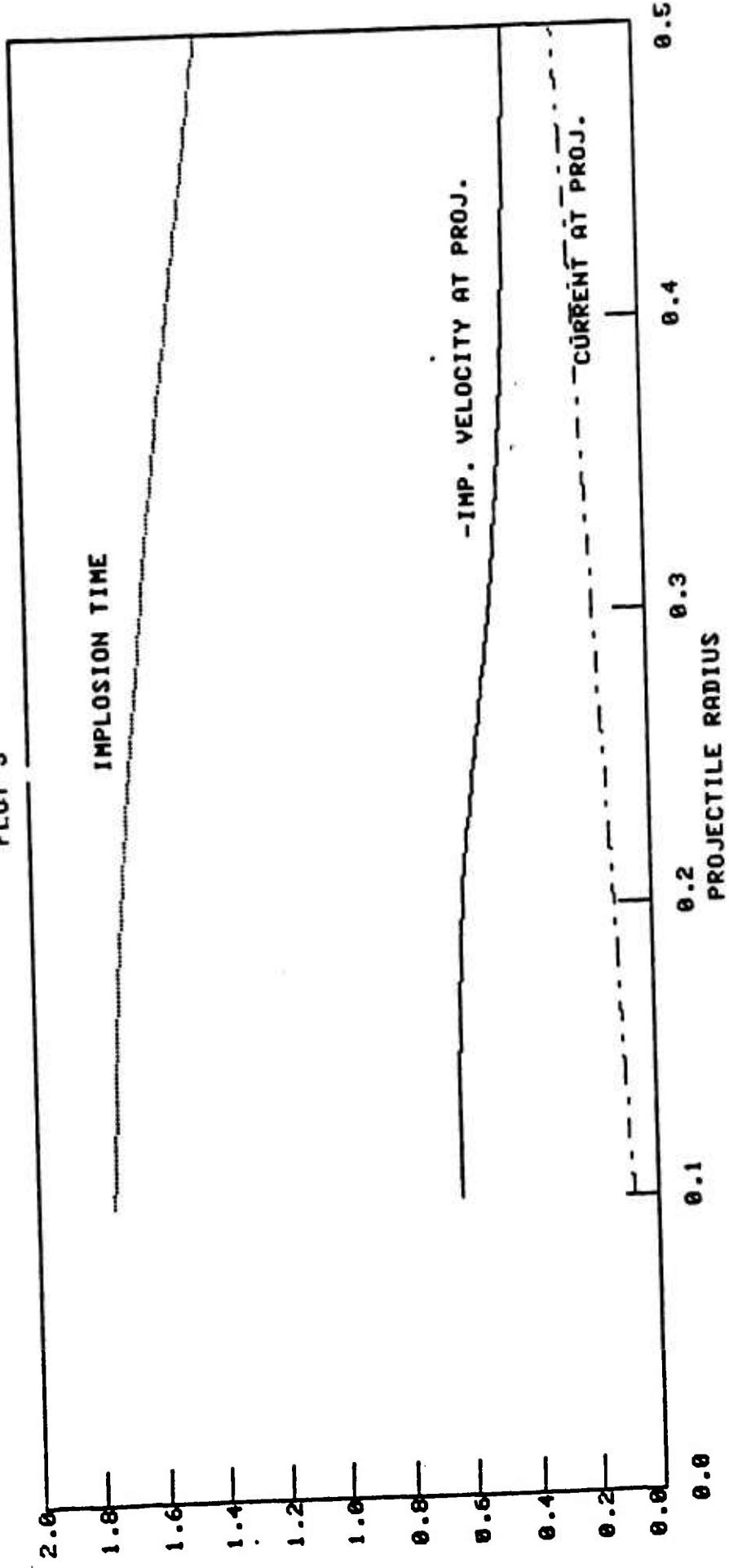
Figure 35. Plot of $\tau_{imp}$, $-\frac{dA}{d\tau}(\tau_{imp})$, and $i(\tau_{imp})$ versus projectile radius $A_p$. Some of the apparent loss in implosion velocity (or efficiency) could be recovered by allowing the initial derivative of the current to decrease.

43
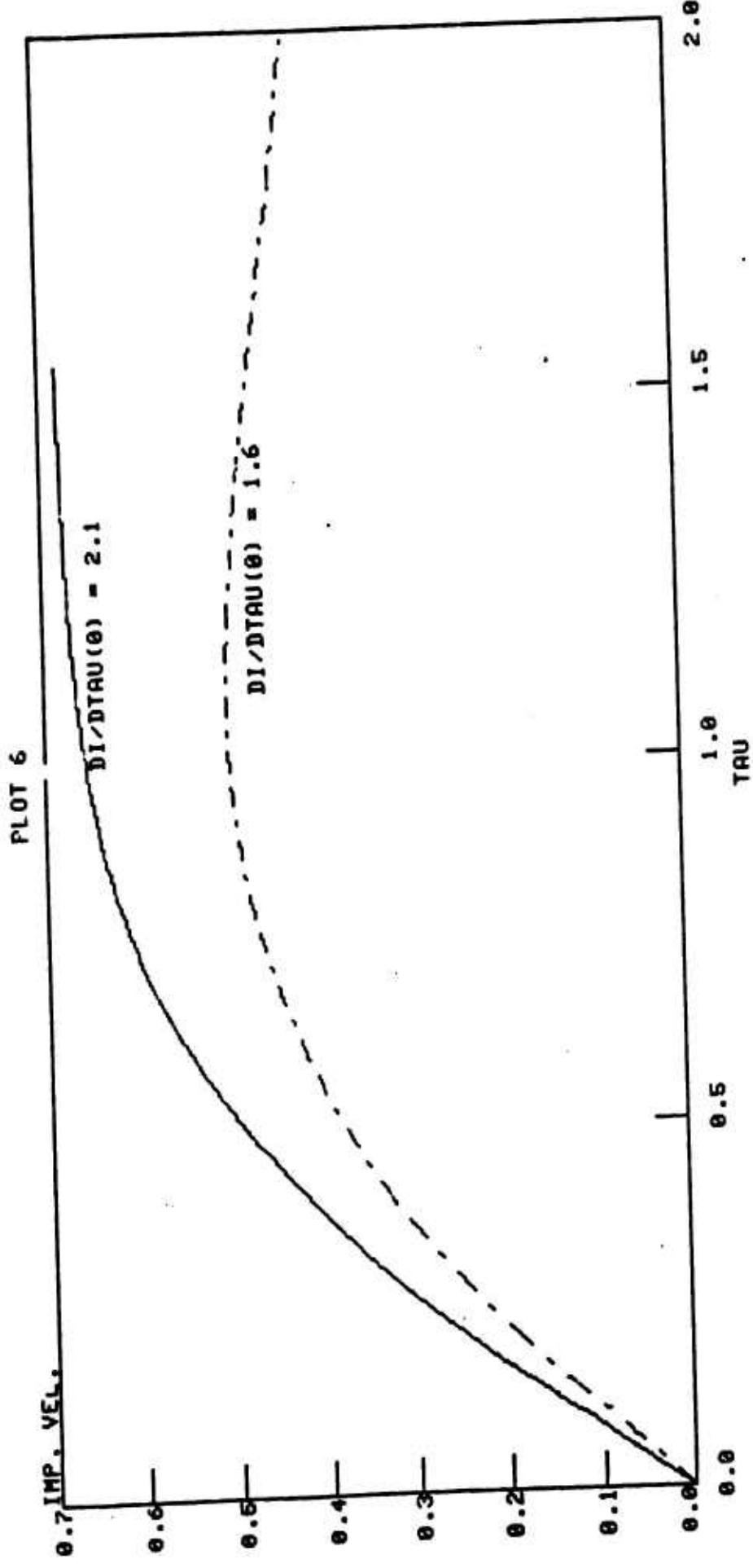
Figure 36. Plot of implosion velocity versus $\tau$ for two values of $\frac{di}{d\tau}$ (0). For $\frac{di}{d\tau}$ (0) = 2.1, the implosion velocity is higher but there is no stabilizing force on the projectile. Lowering $\frac{di}{d\tau}$ (0) reduces the implosion velocity and efficiency somewhat, but provides a potential well for projectile stability.

APPENDIX

45

The MAID System -

Data Base and Design Issues

S. A. Goldstein, F. Sandel, D. A. Tidman, D. Massey
GT-Devices (JAYCOR)*

and

I. M. Vitkovitsky, V. E. Scherrer
Naval Research Laboratory[†]

GTD80-3

Presented at the

Conference on Electromagnetic Guns and Launchers

November 4-6, 1980

San Diego, California

The MAID system stands for <u>M</u>ass <u>A</u>ccelerator using <u>I</u>mploded <u>D</u>ischarges [see J. Applied Physics <u>51</u>, 1975 (1980)]. It is designed to accelerate masses of a few grams to velocities at $\sim 10^7$ cm/s and is based on the fact that plasmas can achieve velocities in that range using very simple pulse power technology. The plasma density, $\rho$, that impacts on the moving mass and accelerates it is chosen so that the resulting pressure during plasma-solid impact ($P \sim \rho v^2$) should not exceed the crushing strength of the solid. Presently such a system is being tested at JAYCOR and we review here the basic concept, the driving mechanisms, and the features of the system. Recent experiments performed at the Naval Research Laboratory which provide data supporting the feasibility of the MAID concept will also be discussed.

In Figure A a conceptual schematic of MAID shows a set of Z-pinches at different stages of radial implosions towards a common axis. The cone shaped projectile is injected from the left and is engulfed by the collapsing plasma only on its trailing side. The center of action of the pressure pulse on the projectile lies ahead of its center of mass so that stable acceleration in the axial direction is expected (but a variety of projectile geometries will be explored). The sensing units between the modules provide information on projectile location and velocity and via a fast logical system decides on triggering times of the modules ahead of projectile location. The typical axial electrode spacing per module is a couple of cm for projectile masses near one gram. Since crushing strengths are $\sim 10^9$ dynes/cm$^2$ the expected increase in projectile velocity will be in the range of $10^3$ to $10^4$ cm/s per module. About $5 \times 10^3$ modules are needed in order to achieve $10^7$ cm/s.

The driving mechanisms on the projectile include three major contributors and each one of them can be varied in order to achieve optimum acceleration along the accelerator. These include: (i) collision of the imploding plasma with the projectile, (ii) sustained magnetic pressure due to the Z-pinch current holding on the plasma and (iii) projectile material ablation.

The first mechanism imparts momentum in the axial direction because the plasma is pushed back (lowest pressure holding against it is in the hole towards the previous module). Momentum conservation implies that the projectile velocity increase is approximately equal to the plasma velocity times the plasma-to-projectile mass ratio. Since the plasma is swept radially inwards,

1

decreasing its radius by an order of magnitude, the plasma mass can be about $10^{-3}$ g and at a velocity of $10^7$ cm/s it will impart $10^4$ cm-g/s to the projectile. Notice that the plasma density in front of the projectile is only $10^{-6}$ g/cm$^3$ so that the shock generated in front of the projectile does not give rise to a significant drag.

The sustained magnetic pressure (mechanism ii) may be important if high current persists through the Z-pinch which holds the plasma against radial expansion, thereby forcing it to expand axially backwards. The plasma mass may be increased by flow of additional gases from the conducting walls into the Z-pinch replacing the plasma that jets back. This mechanism is useful mostly at the low velocity end (v < $10^6$ cm/s).

The ablation of material (iii) of the projectile is a result of both radiation and heat transfer from the plasma to the projectile. Part of the outer layer will undergo evaporation (protecting during that process the internal parts by turning into an opaque plasma) and ablate backwards adding to the momentum transfer by rocket action. Since this mass is already moving with the projectile and it is ablated back so that its velocity is reduced in the laboratory frame (ideally to zero!) it works as a very efficient rocket.

A few simple mathematical models treated show that a combination of the above mechanisms can result in efficiencies of ~ 20% for the overall system. In particular, high efficiency is obtained at the high velocity end while dropping, roughly linearly, with velocity at low velocity (~ $10^5$ cm/s). The basic reason for this result is that MAID is a momentum driver, imparting a fixed momentum increase. The energy increase of the projectile is mv$\delta$v and for fixed m$\delta$v the energy efficiency goes up with v.

The major advantages of the MAID system relate to its use as a long lived device. The projectile has no contact with the walls but is confined radially by the dense plasma. The Z-pinch plates can thus be used for many shots where the lifetime is limited by low current plasma effects and not by the projectile wall interaction. It is thus of major importance to study long lifetime Z-pinch systems for currents of the order of 2 to 3 $\times$ $10^5$ A.

The projectile survives since no current is driven through it. The distributed power is a very natural consequence of the concept and while the system as a whole can deliver a few tens of megajoules it does so in a time of

2

order $10^{-3}$ s and the separate units overlap each other in time (recall the Z-pinches are in various stages of collapse) so that very simple and low power units $\sim 10^8$ W can be employed. Existing, cheap units having long life can be employed in such a system including a combination of capacitor banks and small homopolar generators.

The geometry of the elongated system allows ease of access, replacing parts, cooling of the system, redundancy in diagnostics and finally, simple, low tolerance requirements. The pressure of $\sim 10$ Torr allows both a simple vacuum system and no attention to plasma contamination issues, and the system thus recovers fast enough to allow a high rep-rate (1 to 10 Hz are very easy). The aiming of the projectile is achieved by both the centering action of the Z-pinches and by fine tuning plasma puffs that will be distributed with sensing systems over a few meters of post acceleration to aim $\delta\theta < 10^{-4}$. Lengths vary from a few tens of meters for $10^6$ cm/s and hundreds of meters for $10^7$ cm/s for the applications discussed in the next paper and are in accordance with needs for maintenance, etc.

Presently a five module system (shown in Figure B) has been built using large flat plates with glass insulators to provide Z-pinches from $r \simeq 6$ cm down to 1 cm. The pinches are driven by capacitor banks and gas switches (shown in Figure C). The system could accelerate projectiles to a few $10^4$ cm/s. The physics of plasma-projectile interaction will be studied using this system. We now discuss the NRL experiments using a single Z-pinch that provides a data base for MAID.

3

## Figure Captions

Figure A.  Mass Accelerator using Imploded Discharges

Figure B.` The five module Z-pinch units assembled.

Figure C.  Overview of the lab and the capacitors.

Fig A

MAID

MASS ACCELERATOR USING IMPLODED DISCHARGES
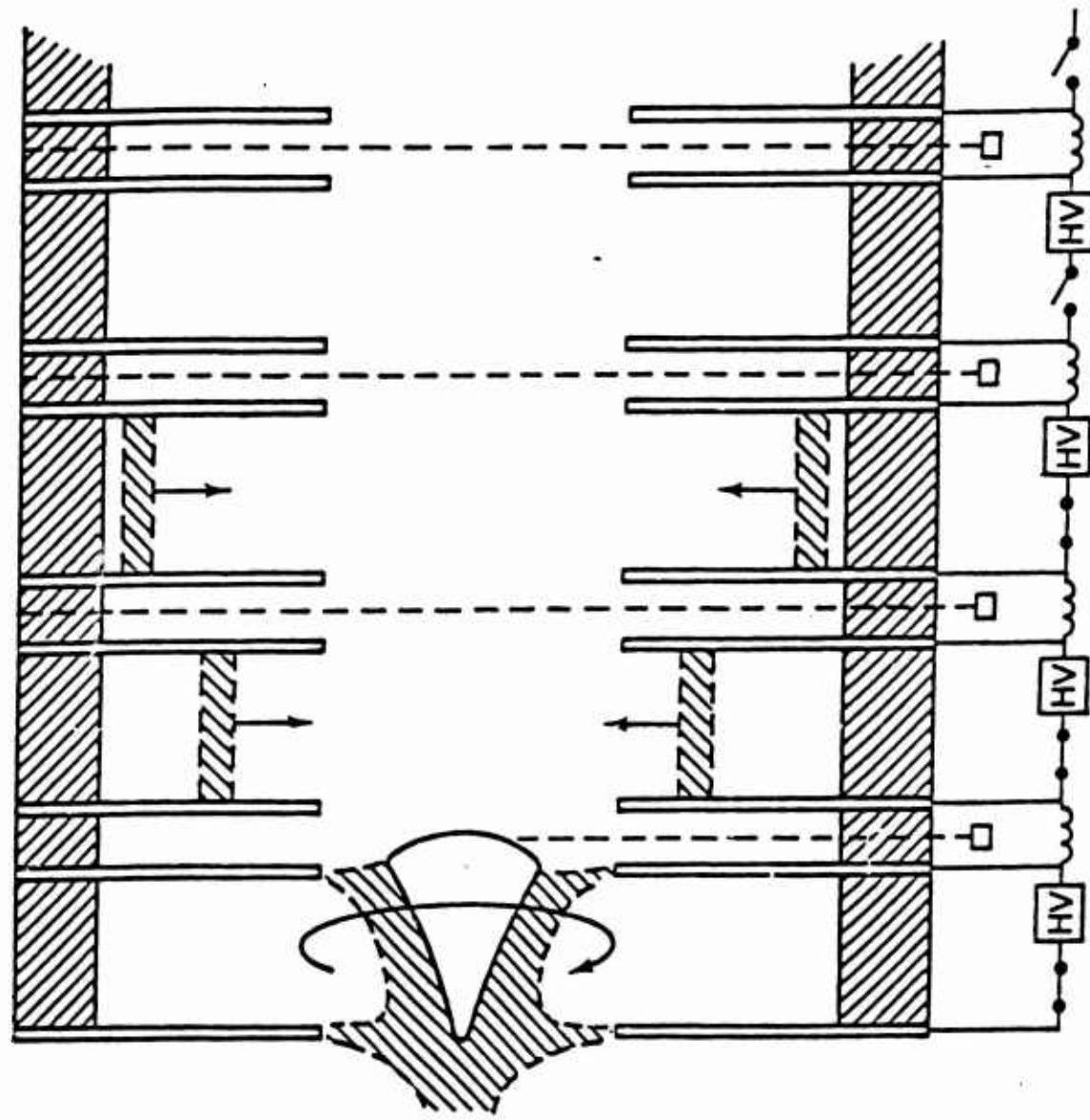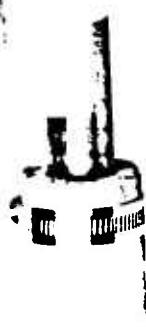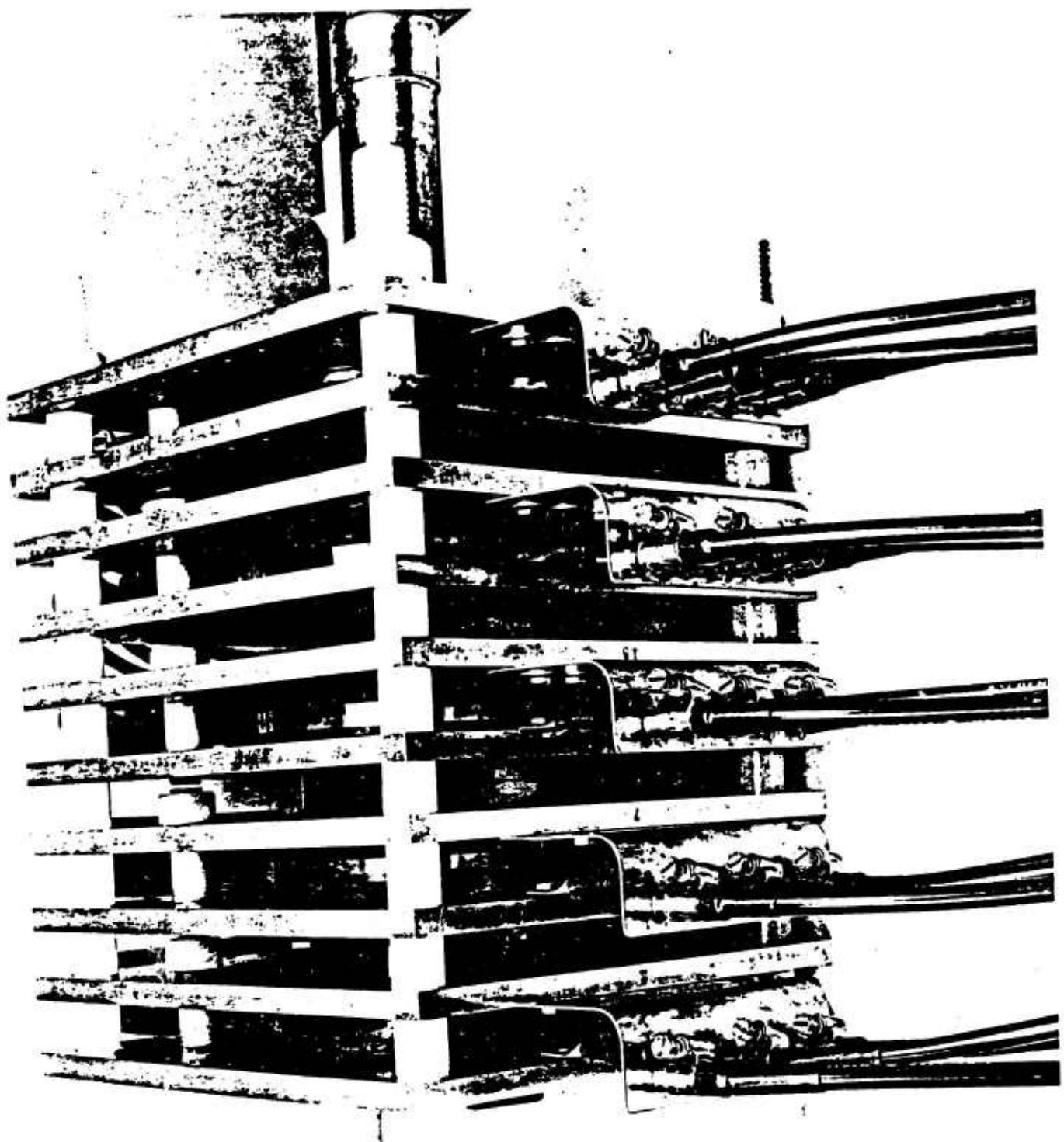
Fig 5.

Fig. 5.
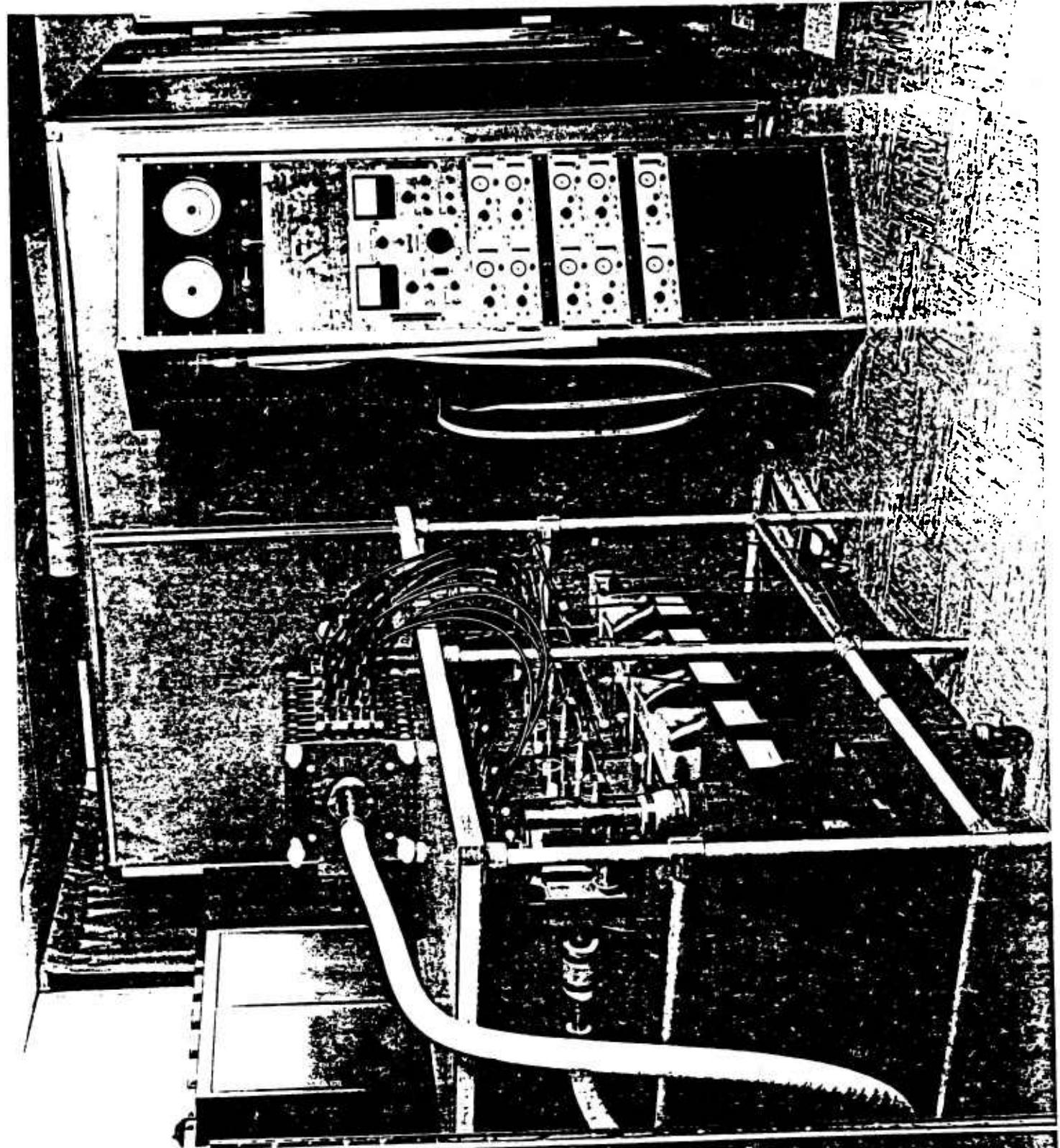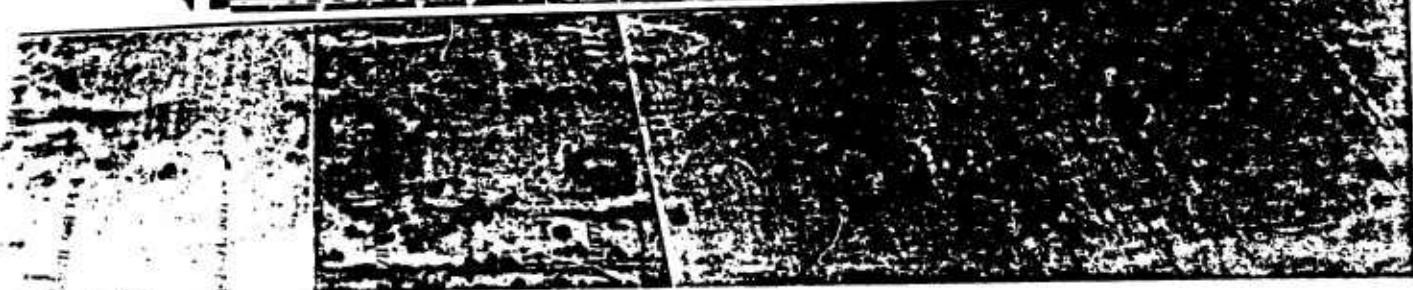
## Plasma Implosions Driven by Fuse-Steepened
## Current Pulses

## I. Introduction

In past years, when plasma facilities operated in the submegajoule range, capacitors were favored over inductive storage systems. Recently, with the need for large systems to generate multi-terawatt submicrosecond pulses, the inductive storage techniques[1-4] have been revived to improve performance at lower cost.

The objectives of this research were to model the AFWL Shiva-II inductive storage system with smaller current and power while duplicating rise-time characteristics. The model system was used to study the interaction between inductive storage and the load, such as the time-dependent partition of current between a pulse-steepening fuse and a realistic plasma load. Fast-rising (200 ns) current pulses generated by such techniques produce a more stable, faster moving plasma which, when thermalized, can be expected to yield a more intense, shorter duration, and higher temperature thermal pulse. The faster moving plasma sheath with closely coupled current would generate a larger rate of change of load inductance, L, so that the load current will not be short-circuited through the fuse. To optimize further the improved coupling of energy to the plasma, various methods of matching implosion time to current rise time by selection of fuse and implosion chamber parameters were also investigated.

## II. The Facility

A circuit diagram and tabulation of circuit parameters is shown in Fig. 1. 50 kJ were initially stored in a capacitor bank,C, when $V_o$ was 60 kV. The

system consisted of two current loops which shared a common element, the fuse. The fuse was vaporized by current $i_1$, when the low inductance rail-gap switches S1 were triggered. As the fuse vaporized in a time interval of 200-300 ns, the voltage $V_{FUSE}$ increased by $L_1 \frac{di_1}{dt}$, and the solid dielectric switch S2 broke down by overvoltage, conducting the current $i_2$ through the load circuit. The imploding plasma load changed its resistance and inductance during the current pulse, leading to a complex interaction with the fuse.

To attain the inductance values tabulated in Fig. 1, to keep the current distribution uniform, and to duplicate other features of the Shiva-II facility, the laboratory layout shown pictorially in Fig. 2 was used. Four identical capacitor banks were coupled to parallel transmission plates by low inductance rail-gap switches. The collector plates, immersed in pure water, connected the capacitors to the fuse and to the implosion chamber at the center.

The arrangement of the $i_2$ circuit is illustrated in detail in Fig. 3. The fuse was a coaxially symmetric wire array, nominally 100 aluminum wires, each 0.0125 cm in diameter. Each wire was 10 cm long wound coaxially on a torroid having the cross-section shown. It was concentric with the implosion chamber in the center. The output switch S2 was a solid dielectric with multiple pinholes extending part way through; it broke down due to over-voltage at a preselected level.

The implosion chamber geometry and dimensions are presented in Fig. 4. The length was 4 cm and the nominal diameter was 5 cm. Sharp circular electrodes were located 3 mm from the walls to initiate the discharge without vaporizing wall material. The uniformity of initial breakdown appeared to be improved compared to initiation along the insulator surface. One end-electrode was rendered semi-transparent for optical viewing by use of a copper screen

2

electrode and lucite window. A high speed streak/framing camera was used to view the implosion in visible light. Small (1 mm diameter) $\frac{dB}{dt}$ loops were located at various radii within the implosion chamber to measure the distribution of current flowing there. The currents $i_1$ and $i_2$ (shown in Fig. 1) were measured as a function of time with $\frac{dB}{dt}$ loops and Rogowski coil (for $i_2$). Low inductance resistive dividers were used to measure voltages. The response of one of these dividers is illustrated in Fig. 5 where the output-pulse is superimposed on the signal into the divider. Pulse distortions are minimal even for pulses with 20 nsec risetime.

III. Fuse Design for Current Steepening

For some time, exploding wires and foils[1-5] have proven to be effective circuit breakers for generating electrical pulses with magnetic energy storage systems. More recently high power pulses with rise times in the tens of nanoseconds have been investigated[6,7] with success. The inductive storage technique has recently[7,8] been extended to operate with capacitor banks in the megajoule range. In the study of wire array fuses for inductive storage,[7] it has been found that the rise time and amplitude of the output voltage depends upon the number of parallel elements for a given fuse cross-section when wire array fuses are immersed in water. The time-to-explosion increases as the number of parallel wires is increased for constant cross-section. This result indicates that, the larger the number of wires the more energy is lost to the surrounding water, and the rise time of the output voltage is thereby increased. On the other hand, a minimum of 10 wires are needed in the fuse to retain symmetric current flow around the Z-pinch so that uniform breakdown and implosion are obtained. The skin depth is also a factor in determining the maximum wire radius. If the wire radius is larger than the skin-depth for the charging

3

frequency of the storage inductor, one would expect the time-to-burst to increase because of non-uniform radial distribution of wire heating.

We have adopted a procedure in which numerical methods of circuit analysis[10] were used to determine the circuit currents, voltages, and output power as a function of time for a given constant load inductance and resistance, fuse cross-sectional area, and fuse length. One computer run was required for each set of input parameters. From a number of such computer runs, optimum fuse parameters were determined. Experiments were then performed in which the diameter, number, and length, of fuse wires were varied. The experimental results were compared to computer calculations, and those of other experimenters[7,11] to confirm our choice of optimum fuse parameters.

The schematic diagram which illustrates the computer calculations is presented in Fig. 6. Input to the computer program include $L_1$, $L_2$, $L_3$, $i_1$ the peak current in $L_1$, the fuse length, and cross-sectional area, and $V_s$ the voltage at which switch S2 closed. Each of the above parameters was varied separately. The computer output was $i_1$, $i_2$, $V_{LOAD}$, load power, and fuse resistance $R_F$, as a function of time for each set of circuit parameters, fuse cross-section and length. In this analysis the characteristic time $t_o$ is defined as:

$$t_o = 6 \times 10^{16} \frac{S^2}{i_1^2} \quad \text{(sec)} \qquad \text{(Eq. 1)}$$

where S is the cross-sectional area of the fuse in $m^2$ and $i_1$ is the peak charging current in amperes; $t_o$ is the "time-to-burst" of the fuse determined from data given in Ref. 9, for Al foils exploded in water with a time to explosion of 200 μsec. For the example of Fig. 7, the value of $R_2$ was chosen to correspond to the case having a negligible value of $\frac{dL}{dt}$, leaving only the resistivity of the imploding plasma. The other input parameters were:

4

100 fuse wires, each $12.7 \times 10^{-3}$ cm in dia., 20 cm long Al wires. This results in $t_o = 2.4 \times 10^{-8}$ sec. When the following quantities are used,

$L_1 = 31$ nh $\qquad L_2 = 25$ nh $\qquad L_F = 10$ nh

$i_1 = 10^6$ amps $\quad V_s = 50$ kV $\qquad R_2 = 0.01 s$ .

The calculated quantities $i_1$, $i_2$, $V_L$ and fuse conductivity plotted in Fig. 7 as a function of time are obtained. The switch S2 was assumed to close early in the rise of $V_F$, at about 50 kV, allowing current $i_2$ to flow through the load. As the fuse conductivity approached zero causing the current $i_1$ to decrease, $V_{FUSE}$ increased rapidly by an amount $V = V_1 L \dfrac{di_1}{dt}$ also causing $i_2$ to rise. When the fuse conductivity reached zero all of the circuit current was flowing through the load and $i_1 = i_2$.

Similar computer runs were made in which the number of 5 mil. diameter fuse wires were varied from 40 to 500. Other input parameters were the same as the example plotted in Fig. 7. That is, the load resistance was small compared to the inductive reactance. Another set of computer calculations indicated similar results when the load resistance was increased to 0.5 Ohm when it was large compared to the inductive reactance. The curves of Fig. 8 indicate that power and voltage are optimized for 100 wires. This fuse wire array however transfers less than optimum energy. It has been shown[2] that optimum energy is transferred from the capacitor to the load when:

$$\frac{W_o^{3/2}}{V_0 L_1^{\frac{1}{2}} S} = k_1 a \qquad\qquad\qquad \text{(Eq. 1)}$$

where: $V_o$ = Capacitor Voltage

$\qquad W_o$ = Stored Energy

$\qquad L_1$ = Storage Inductance

$\qquad S$ = Fuse Cross-Sectional Area $(m^2)$

$$1 < k_1 < 3$$

$$a = 2.2 \times 10^{16} \text{ Joules/kG for Al.}$$

When:   $V_o = 40$ kV

$W_o = 24$ kJ

$L_1 = 26$ nh

$k_1 = 2$ (kV/micron)

From Eq. 2, $S = 2.4 \times 10^{-6}$ m$^2$.

This corresponds to 280, 5 mil diameter wires. Since the computer calculations were based on experimental data accumulated under different conditions (200 μsec charging time) than the present ones, experimental fuse data was needed to compare, first with an experiment in which multiple wire fuses were exploded[11] in air and then one in which similar arrays were exploded in water.[7] In a later section, our present experimental results are compared with computer runs where a "dummy load" of fixed inductance and zero resistance was used.

The effect of the surrounding medium on fuse vaporization has been investigated by Kosalyn, et al.,[11] for wires exploded in air. They found that the initial rate-of-rise of fuse resistance was described by the following formula:

$$\frac{dR}{dt} = \frac{16 \ell v \rho}{\pi n d^3} \qquad \text{(Eq. 3)}$$

where $\rho$ is the cold resistivity, $\ell$ is the wire length, n is the number of parallel fuse wires, d is the diameter of each wire, and v is the velocity of the vaporization wave.[12] The only quantity in Eq. 3 that should be affected by the environment surrounding the fuse is the vaporization velocity v. The only data[12] available for v were the wires exploded in air at atmospheric pressure. If we assume that the vaporization wave velocity is the same for wires exploded in air and water, we can compare experimental values with those calculated using Eq. 3. This has been done for arrays of copper and aluminum wires and the results are presented in Table I where the ratio

of our experimental data to that calculated using Eq. 2 is shown in the last column.

### TABLE I: SUMMARY OF FUSE PERFORMANCE

| Wire Material | Number of Wires | Diameter (MILS) | Length (CM) | Maximum Fuse Resistance | Experimental dR/dt | Calculated dR/dt | Experimental Calculated |
|---|---|---|---|---|---|---|---|
| CU | 70 | 5 | 5 | 0.10 | $5.2 \times 10^3$ | $6.2 \times 10^3$ | 0.8 |
| CU | 70 | 5 | 5 | 0.60 | $1.0 \times 10^4$ | $6.2 \times 10^3$ | 1.7 |
| CU | 100 | 5 | 10 | 0.75 | $2.5 \times 10^4$ | $0.86 \times 10^4$ | 3.0 |
| CU | 400 | 1.8 | 10 | 0.11 | $4.0 \times 10^4$ | $4.5 \times 10^4$ | 0.9 |
| AL | 100 | 5 | 10 | 0.70 | $5.0 \times 10^4$ | $2.5 \times 10^4$ | 2.0 |

The table summarizes results for several shots using copper and aluminum fuses, with tabulations of the number of wires, diameter, length, and maximum fuse resistance. The experimental dR/dt was taken from the initial straight-line portion of the resistance-time curve (about 200 ns). When a comparison is made between the experimental dR/dt values and those obtained by substituting values into Eq. 2, they agree within a factor of 3, and we conclude that our data for fuse wires exploded in water do not differ significantly from those of a simple model that was developed for explosions in air. The "time-to-burst" is defined as the time interval between initial current flow in the exploding wire, and when current cut-off occurs due to wire vaporization. It was previously established[7] that:

$$t_0 = 0.0094 \ (N-1)^2 + .37 \qquad \text{(Eq. 4)}$$

where $t_0$ is the time to burst and N = the number of 1 mil diameter copper wires immersed in water. Eq. 3 was confirmed for the range $(1 < N < 24)$.

7

In Fig. 9 for our experimental data "time-to-burst" ($t_o$) is plotted versus the number of 5 mil diameter copper wires (40 < N < 80) immersed in water. Our data also support the variation described by Eq. 3.

The build-up of fuse resistance as a function of time is illustrated for three different wire fuse arrays in Fig. 10. The peak resistance recroded during any of the events was 0.7 Ohm for a 5 mil diameter aluminum wire.

## IV. Transfer of Current to an Inductive Load

The calculations of fuse performance by computer analysis of circuit constants described previously and shown schematically in Fig. 6 can be checked experimentally by placing a short circuit in the implosion chamber in place of the plasma arc. Then the load inductance is 15 nH and the load resistance is approximately zero. A typical example of experimental results obtained with such an arrangement are shown in Fig. 11 where oscilloscope signals of fuse currents are shown in the upper picture and output current is reproduced in the bottom. $I_1$ was 1 MA; $I_2$ reached 600 kA in 200 ns. Experimental results obtained with aluminum fuse wires and a fixed inductive load are compared with theory in Fig. 12. The significance of this comparison is that for the same wire array parameters $I_2/I_0$ experimental exceeds $I_2/I_0$ theoretical nd has a slightly faster risetime. We conclude that the fuse works as predicted.

## V. Transfer of Current to an Imploding Plasma Load

When the "dummy load" described above was replaced with a Z-pinch, the interaction between fuse and load plasma were much more complex, and experiments with plasma diagnostic measurements were required. Streak/framing photography and dB/dt probes were used.

An example of such an implosion driven by the capacitor bank without a fuse, is presented in Fig. 13. The chamber was filled with hydrogen having an ambient pressure of 0.38 Torr; current at minimum plasma radius was 500 kA. A streak picture displays radius versus time and two-dimensional pictures

were obtained at the times indicated. The leading edge of the plasma sheath imploded in a time $t_{cl}$ = 700 ns. In the frames shown, part of the field-of-view was obscured by vacuum and dB/dt loop connections. The framing pictures show that the plasma formed and imploded uniformly.

Since some of the details of the implosion are lost in photo-reproduction a schematic representation of the streak picture has been sketched in Fig. 14. This illustrates that the plasma sheath was initiated uniformly at the sharp electrodes and retained this form as it accelerated inward. The leading edge of the plasma appeared to continually accelerate and collapse to the center line, where an expanding or reflected shock wave was immediately generated. The following plasma in the sheath appeared to slow down before interacting with the expanding shock, and the process of plasma thermalization was "stretched out" in time.

In contrast to the previous example, Figs. 15 and 16 illustrate a plasma driven by a fuse-steepened current pulse. The chamber of Fig. 4, filled with hydrogen having an ambient pressure of 0.38 Torr, was used. The nominal fuse contained 100-5 mil diameter, 10 cm long aluminum wires. As indicated in Fig. 15, the load current reached 500 kA in 200 ns. The streak picture in Fig. 16 shows that the leading edge imploded to the center line in 160 ns. In comparing the two examples with and without fuse, we note that the fuse driven plasma imploded more than twice as fast and the sheath thickness was less by more than a factor of two. The picture of Fig. 16 shows wall heating due to radiation, indicating possible electrical breakdown. Values of r and $\frac{dr}{dt}$ were derived from the leading edge of the plasma and are plotted as a function of time in Fig. 17. The curves show that most of the acceleration occurred in the final few millimeters of travel and that the leading edge

9

reached a $\frac{dr}{dt}$ of $5 \times 10^5$ m/sec as r approached zero. If we assume that $Z_p = dL/dt$, it is possible to calculate the effective radius of current flow versus time from measurements of dr/dt and $V_L$.

$$Z_p = \frac{V_L}{i_2} = dL/dt = -2 \times 10^{-7}\, \ell\, \frac{dr/dt}{r}$$

$$\frac{d}{dt}(\ell n\, r) = \frac{V_L/i^2}{2 \times 10^{-7}\, \ell}$$

$$r = r_o \ell^{\frac{V_L/i^2\ t}{2 \times 10^{-7}\, \ell}} \qquad\qquad\qquad \text{(Eq. 5)}$$

In Fig. 18, we plot r(t) for the leading and trailing edges of the imploding plasma. Shown also in the graph is a plot of r(t) calculated by using Eq. 5 and the measured quantities $V_L$ and $i_2$. A correction was made to $V_L$ for the $L_p$ di/dt voltage drop within the implosion chamber. This graph shows that the effective radius of the current lags behind the plasma for most of the implosion time but catches up during the last 1 cm of travel. Measurements obtained with dB/dt probes placed at two radial positions also indicate that current lags behind the current sheath. This subject will be discussed in detail later.

The performance of the inductive storage system depends upon the fuse resistance versus time characteristic and its ratio to the load impedance. The fuse resistance is plotted against time for the previous example in Fig. 19. Resistance increased from zero to 0.36 Ohms in 160 ns. This is approximately equal to the risetime of load current. For the application of model data to Shiva it is important to understand the role of fuses in transferring current from the inductive store to the load. We expect this transfer to be optimized when $Z_L/R_F$ is much less than 1. The previous example is completed by presenting this data.

The ratio of load and fuse impedances $Z_L/R_F$ is plotted as a function of time for the above example in Fig. 20. The ratio is much less than 1 during the critical final compression time. This is a very important result, since the ratio must be small for efficient energy coupling to the load. We do not presently know the effects of the higher ratio at early times on the coupling.

In order to understand the mechanisms of energy absorption in imploding plasmas, we would like to know the distribution of mass and current as a function of time during the Z-pinch implosion. It is generally assumed that the snowplow model of the Z-pinch[13] applies and that the mass is swept up and contained within the plasma sheath. The current would also follow the ionized channel defined by the plasma sheath. However, measurements in conventional Z-pinches[14] indicate that at times current flows elsewhere in the implosion chamber. Since the current distribution determines dL/dt, including its final value, we decided to measure the current at two positions in the chamber and to correlate the current measurements to the plasma sheath position. Small loops 1 mm in diameter were mounted 1.2 and 3.2 cm from the center line of the chamber midway between electrodes. The results are shown for a no-fuse experiment in Fig. 21. The plasma profile, extracted from the streak image, is plotted at the top, and currents are plotted on the same time scale at the bottom. The results show that for each dB/dt loop, current begins to flow immediately when the leading edge of the plasma passes, as expected. However, the current is small at this time and at $t_c$ is only 50 kA, 14% of the load current. Only 10 kA flows inside dB/dt. A similar result is obtained when a fuse steepened current drives the Z-pinch as shown in Fig. 22.

These results confirm that current distribution of imploding plasma systems have a substantial thickness in comparison to initial plasma radius. Additionally, most of the current does not appear to flow in the imploding

11

plasma sheath as predicted by early theory.[13] There are several possible
explanations. First, there may be a basic measurement problem with dB/dt
loops in the plasma. They may substantially perturb the plasma flow. Second,
radiation induced ionization at the walls may produce a conducting path that
"short circuits" the plasma sheath and finally, an imcomplete ionization at
early times may cause gas to be left behind, later becoming conducting.

It is not certain that radiation induced breakdown along the walls is
detrimental. It has been shown[17] that wall breakdown causes circulating cur-
rents within the implosion chamber. That is, the wall breakdown acts like a crow-
bar, trapping energy inside the chamber. If this breakdown can be timed to
occur at peak current, energy present in the implosion chamber may be dissipated
in the imploding plasma. Our current traces shown in Figs. 21 and 22 also
indicate circulating currents. The dB/dt 1 and dB/dt 2 currents exceed the
circuit current when $t \cong 2.8$ μsec (Fig. 21).

Despite the apparent problem of current distribution, it is evident that
current steepening fuses greatly increase power flow in imploding systems.
This is illustrated in Fig. 23 which compares streak images for implosions with
and without fuse steepening. The ambient pressure of hydrogen was the same in
both cases and load current at $t_{ci}$ was 500 kA in both cases. The fuse
steepening decreased the implosion time from 340 ns to 160 ns while the sheath
thickness was decreased by more than a factor of 2. These results are shown
more quantitatively in Fig. 24 where radius of the leading edge is plotted
against time for the two cases.

In general, the implosion time follows the classic relation for Z-pinch
implosion time:

$$t_c = K(m/\ell)^{\frac{1}{4}}(di/dt)^{-\frac{1}{2}}10^{-8} \text{ sec.} \qquad\qquad \text{(Eq. 6)}$$

where K is a constant and $\ell$ is the length of the implosion, M is mass/unit
length and di/dt is the current rise at $t = 0$. This linear dependence has
been published[15] for $t \geq 3$ μsec and is reproduced as a solid line in Fig. 25.

Shown also in the figure are points obtained at NRL with and without fuses. The dotted line extension of data from Ref. 15 passes through the NRL points. Although Eq. 5 was fitted to gas Z-pinches it is interesting that Shiva imploding foil data[16] have $t_c$ values less than those predicted by Eq. 5.

In general, the technique using fast-opening fuses to increase the power flow a storage system to the imploding plasma has been proven to be successful. The wire array fuse immersed in water performed as predicted when precision drawn wires were used. The measured load current and rise-time agreed with values calculated by circuit analysis. The time-to-burst agreed with previously published[7] semi-empirical formulas for wires exploded in water. The initial rise fo fuse resistance dR/dt, agreed with calculated values using a published formula[11] for wires exploded in air. The implosion time for gas Z-pinches powered by inductive energy storage is proportional to $(dI/dt)_{t=0}^{-\frac{1}{2}}$ in agreement with published results.[15] The plasma sheath thickness decreased and and was reduced by use of the wire fuses, indicating the possibility of increased radiation output during final plasma thermalization. Major difficulty in optimizing the heating of the plasma was indicated by dB/dt loop measurement at various radii in the implosion. They showed only a small fraction of the load current to flow through the plasma sheath, as has also been observed by others.[14] To understand this problem fully would require additional research studying the methods to restrict the current flow to a thin plasma sheath for better assembly as well as methods to further increase the speed of implosions to obtain higher thermal output pulses.

Our measurements show that during the later stages of the implosion most of the output current flows through the load and not the fuse.

References
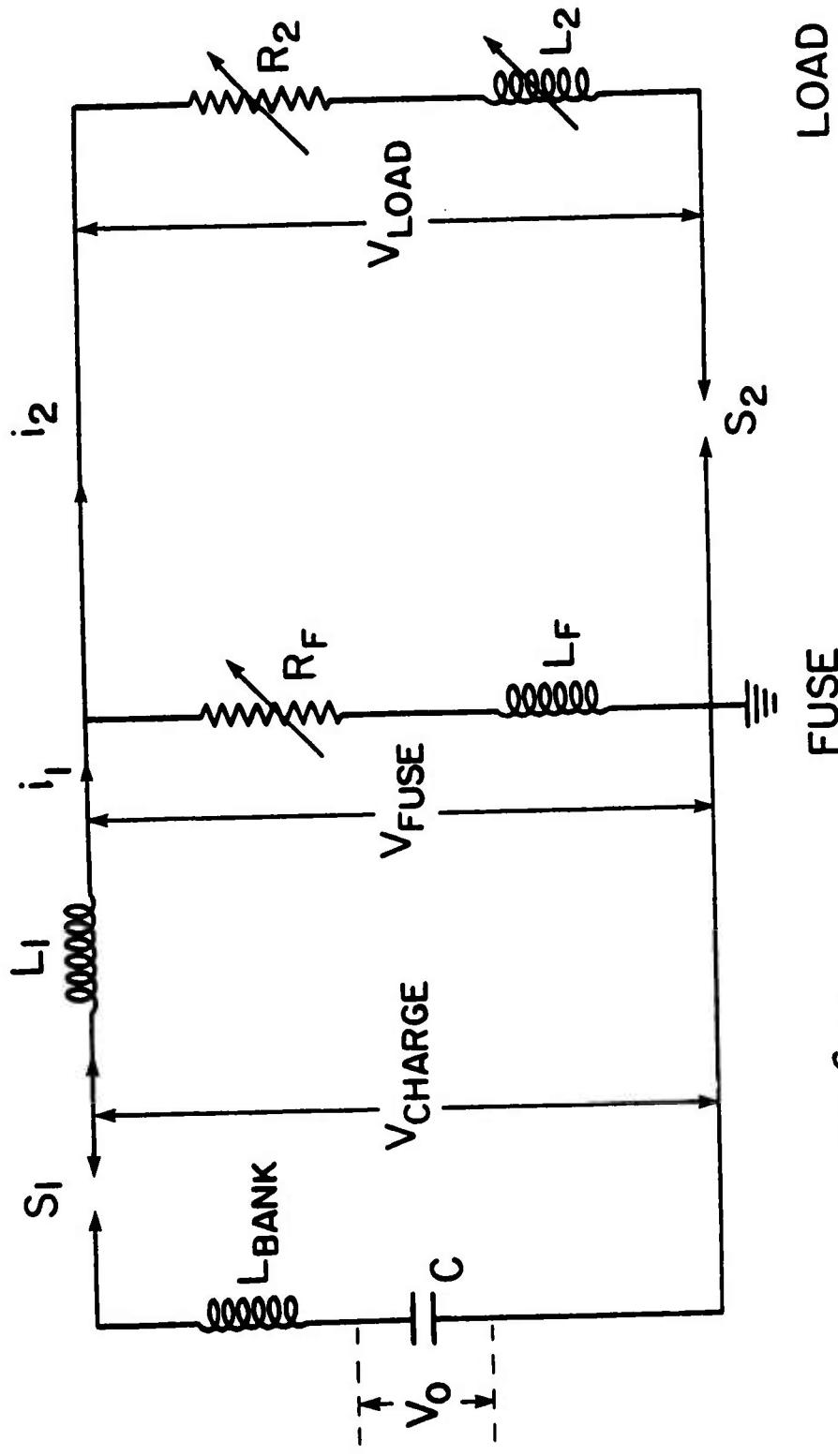
1. H. C. Earily and F. J. Martin, RSI $\underline{36}$, 7, 1000 (1965).

2. C. H. Maisonnier, J. G. Linhart, C. Gourlan, RSI $\underline{37}$, 10, 1380 (1966).

3. L. Liebing, Z. Eng. Physics $\underline{26}$, 345 (1969).

4. S. A. Nasar et al., Proc. of the Sixth Symposium of Engineering Problems of Fusion Research, IEEE Pub. No. 75CH1079-5-NPS (Includes extensive bibliography).

5. Ch. Marjannia, J. G. Linhart, C. Gourlas, RSI $\underline{37}$, 1380 (1966).

6. Yu. A. Kotov, N. G. Kolganov, V. S. Sedor, B. M. Kovaltchuc, and G. A. Mesyats, Proc. International Pulsed Power Conference, Lubbock TX, 1976, PIAI.

7. D. Conte, R. D. Ford. W. H. Lupton, and I. M. Vitkovitsky, Prod. of the Seventh Symposium on Engineering Problems of Fusion Research, Knoxville, TE, 1977, Vol. II, p. 1066.

8. D. L. Smith, R. P. Henderson, R. E. Reinovsky, 2nd IEEE International Pulsed Power Conference, Lubbock, TX, 1979, p. 287.

9. D. Conte, R. D. Ford, W. H. Lupton, I. M. Vitkovitsky, 2nd IEEE International Pulsed Power Conference, Lubbock, TX, 1979, p. 276.

10. W. Lupton, NRL-unpublished work.

11. Article in Russian, B. M. Kosalyn et al. (1972).

12. F. D. Bennett and G. D. Kohl, in Exploding Wires, Vol. 4, p. 1, ed. by W. G. Chace and H. K. Moore, Plenum Press, NY (1968)

13. M. Rosenbluth et al., USAEC Report LA-1850 (1954).

14. I. F. Kvartshava et al., Nuclear Fusion $\underline{11}$, 385 (1971) (Additional references given)

15. L. A. Artsimovich, "Controlled Thermonuclear Reactions", p. 115, Gordon Research Science Publishers, NY, NY, 1964.

16. William L. Baker, Miles, C. Clark, James H. Degnan, Gerald F. Kluttu, Charles R. McClenahan, and Robert E. Reinovski, JAP $\underline{49}$ 4694 (Sep 1978).

17. T. Oppenlander, IAEA VII Conf. Int. Physique Plasmas et al Recherche Concurnant la Fusion Nulearre Controlee, Innsbruck, 1978.

Fig. 1 SCHEMATIC DIAGRAM OF SHIVA MODEL

$C = 30 \times 10^{-6}$ fd

$L_{BANK} = 5$ nh

$L_1 = 16$ nh

$L_F = 10$ nh

$L_2 = 15$ nh

FIGURE 2

CAPACITOR BANK

RAIL GAP SWITCH

WATER TANK

FUSE AND IMPLOSION CHAMBER

COLLECTOR PLATES

FIGURE 3   IMPLOSION CHAMBER AND CURRENT-STEEPENING FUSE

FIGURE 4    SCHEMATIC OF IMPLOSION CHAMBER

Fig 5 RESPONSE OF RESISTIVE DIVIDER TO A FAST
INPUT PULSE DIVIDER IV (UNSHIELDED)

DIVIDER OUTPUT PULSE IS SUPERIMPOSED
ON INPUT PULSE



50 ns/DIV
INPUT 2V/DIV
OUTPUT 100 mV/DIV



20 ns/DIV
INPUT 2V/DIV
OUTPUT 100 mV/DIV

FIGURE 6

FIGURE 7

COMPUTER SIMULATION
CASE II
$t_0 = 96$ ns
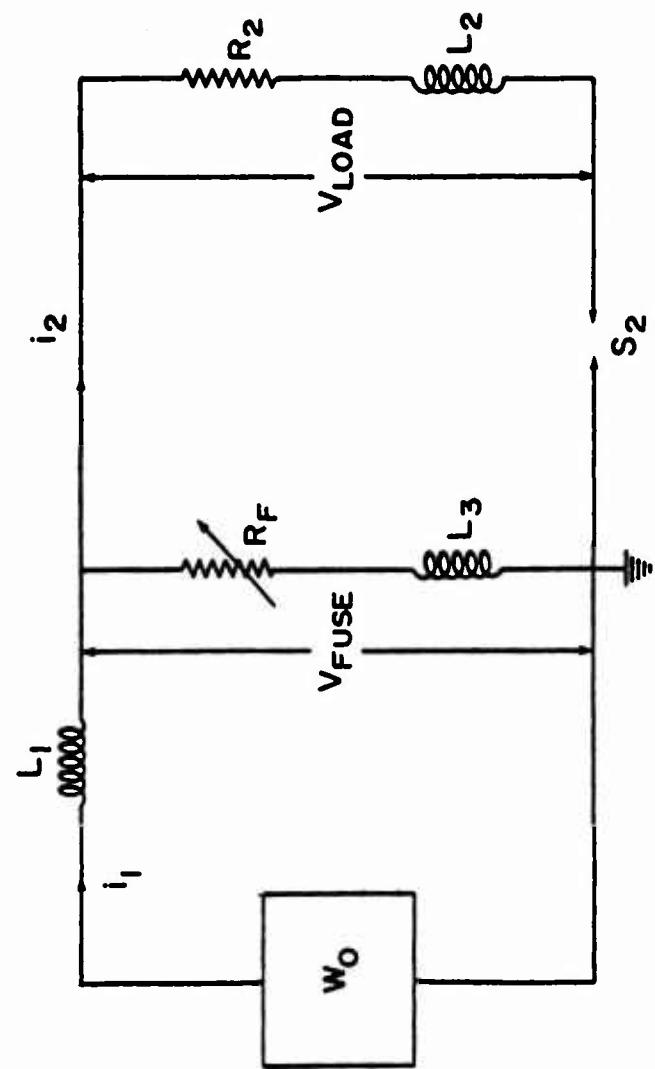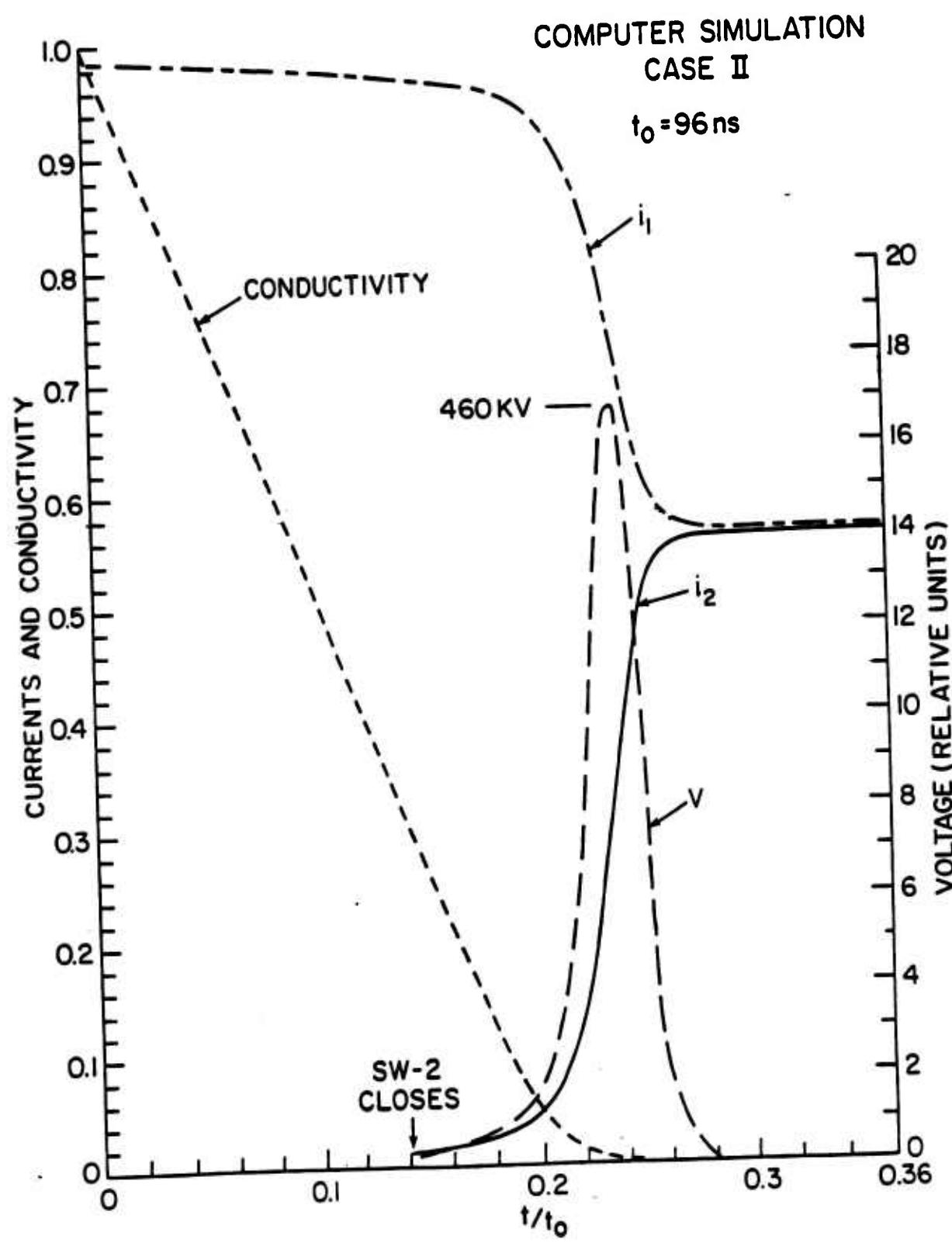
FIGURE 9    VARIATION IN NUMBER OF 5 MIL AL. FUSE WIRES (EACH 10 cm LONG)
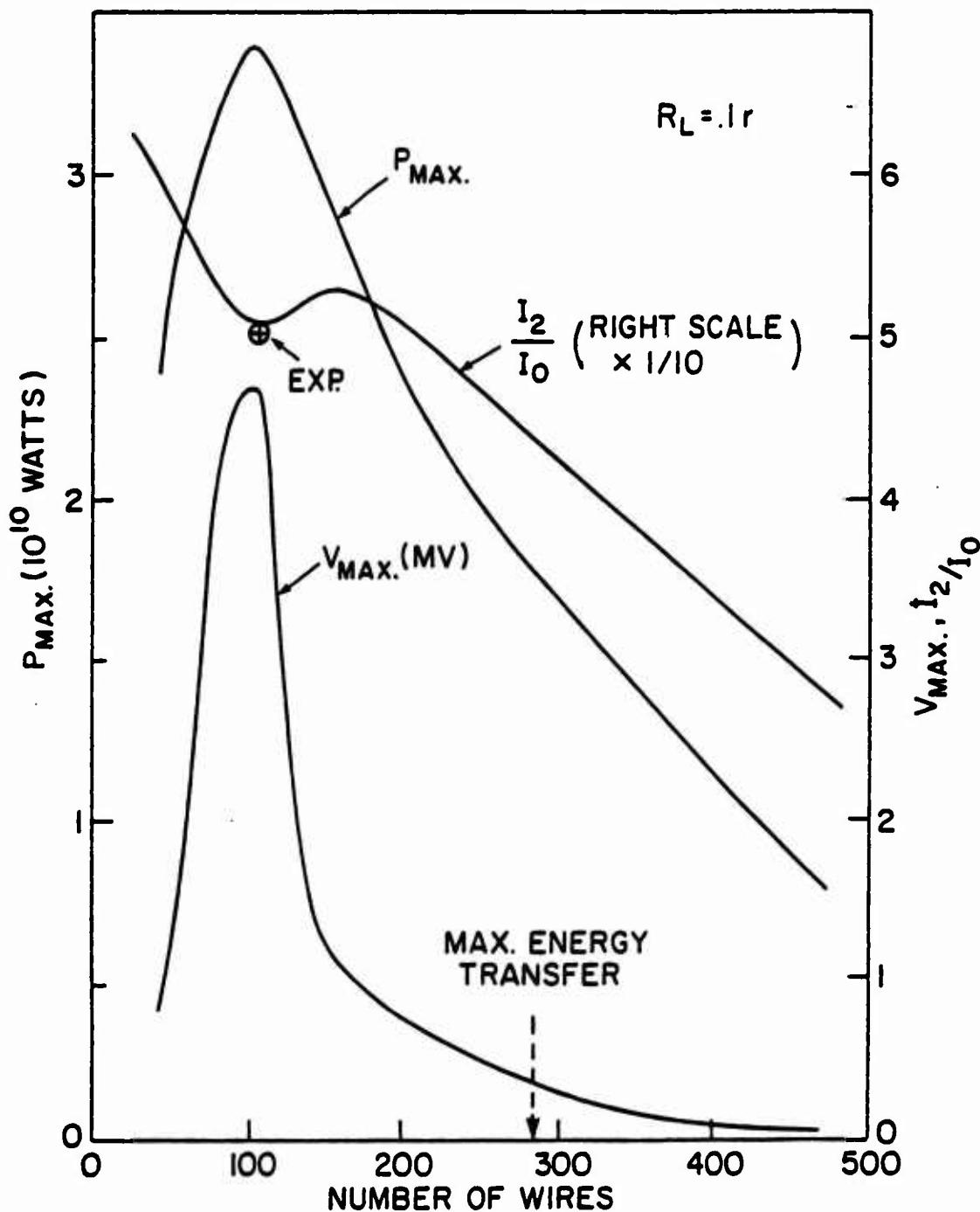
Fig 7 TIME TO BURST ($t_o$) vs. NUMBER OF WIRES
5 MIL DIA. CU  IOCM LONG
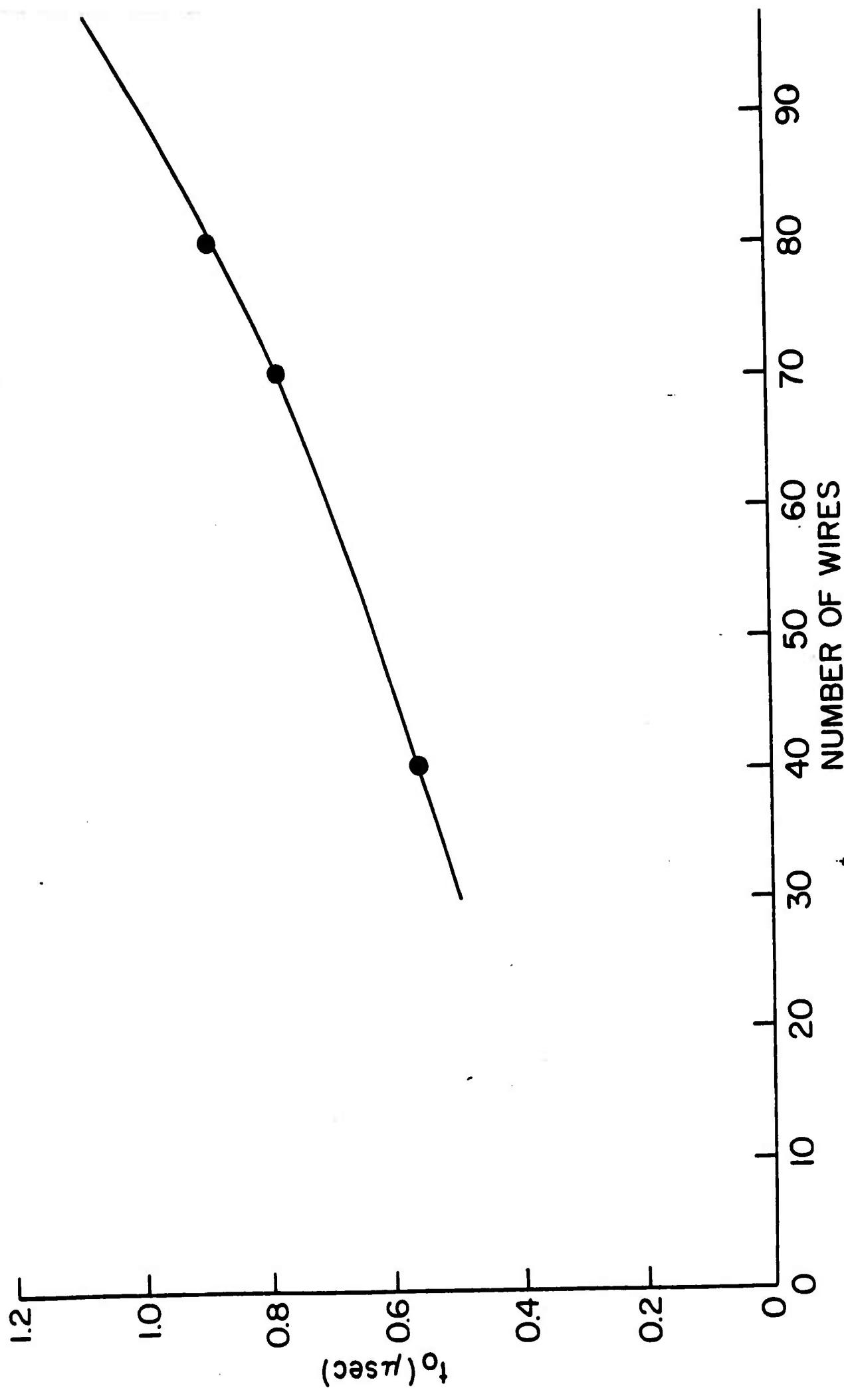
FIGURE 10
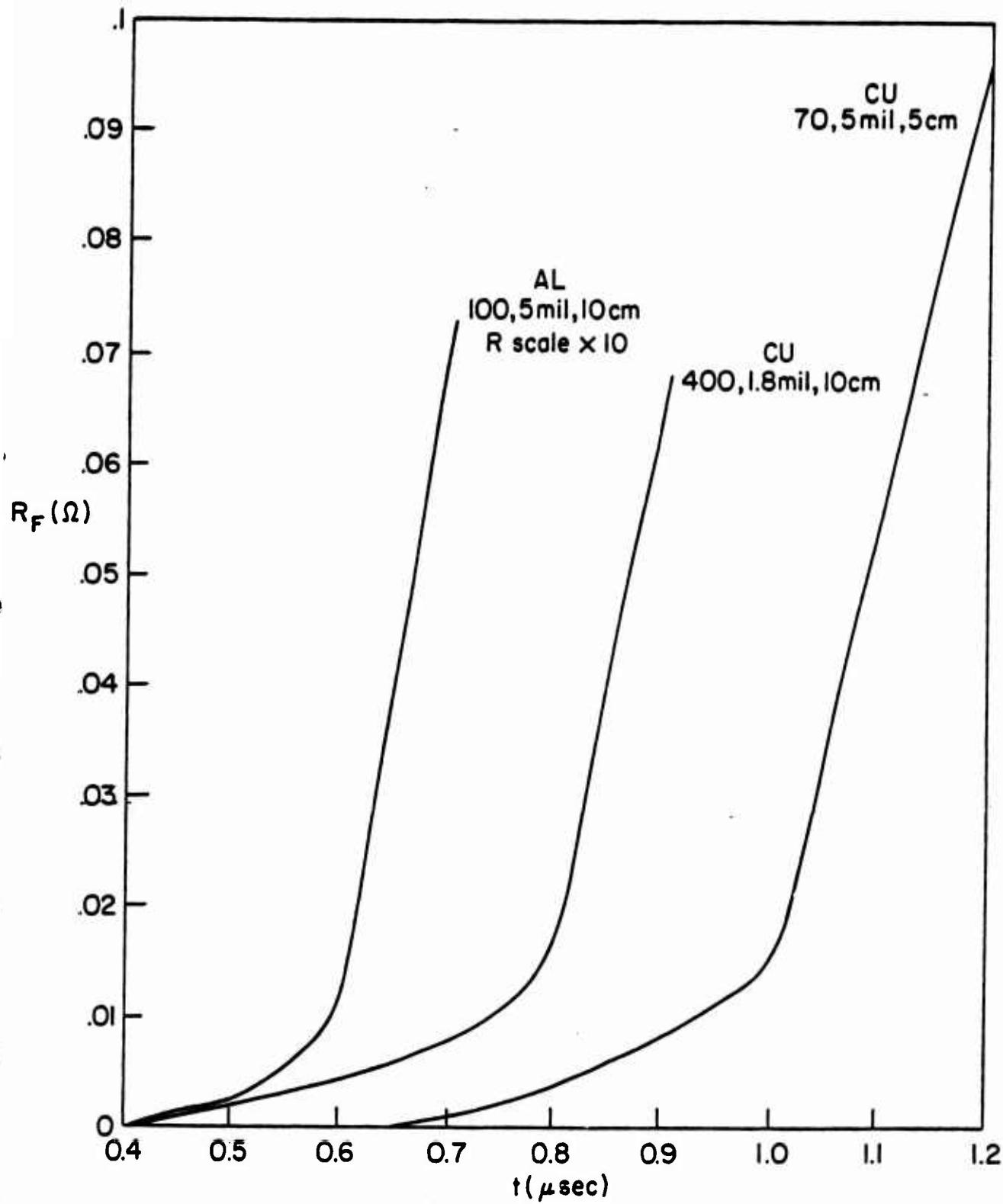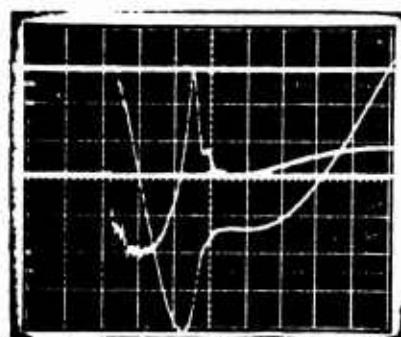
FIGURE 11 TRANSFER OF CURRENT TO AN INDUCTIVE
LOAD. (S-2 FUSE, SHOT 1)

FUSE: 70, 5MIL DIA., 5CM LONG, COPPER WIRES
SWITCH: S-2 THICKNESS = 6 MILS OF POLYETHYLENE
$V_{BANK}$ = 25KV
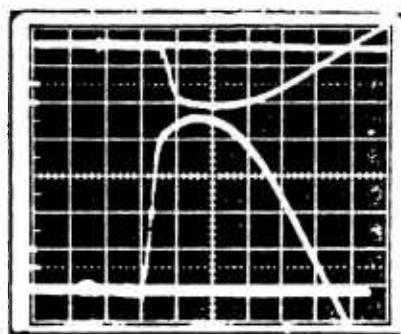
FUSE CURRENT

SWEEP = 500 ns/DIV
TOP TRACE I(t)
LOWER TRACE di/dt

LOAD CURRENT

SWEEP = 500 ns/DIV
TOP TRACE - ROGOWSKI
LOOP I INTEGRATED
LOWER TRACE - ROGOWSKI
LOOP 2 INTEGRATED

FIGURE 12    COMPARISON OF EXPERIMENT AND THEORY

I₁ EXPERIMENTAL
I₁ THEORETICAL
I₂ EXPERIMENTAL
I₂ THEORETICAL

I (RELATIVE UNITS)

t (μsec)
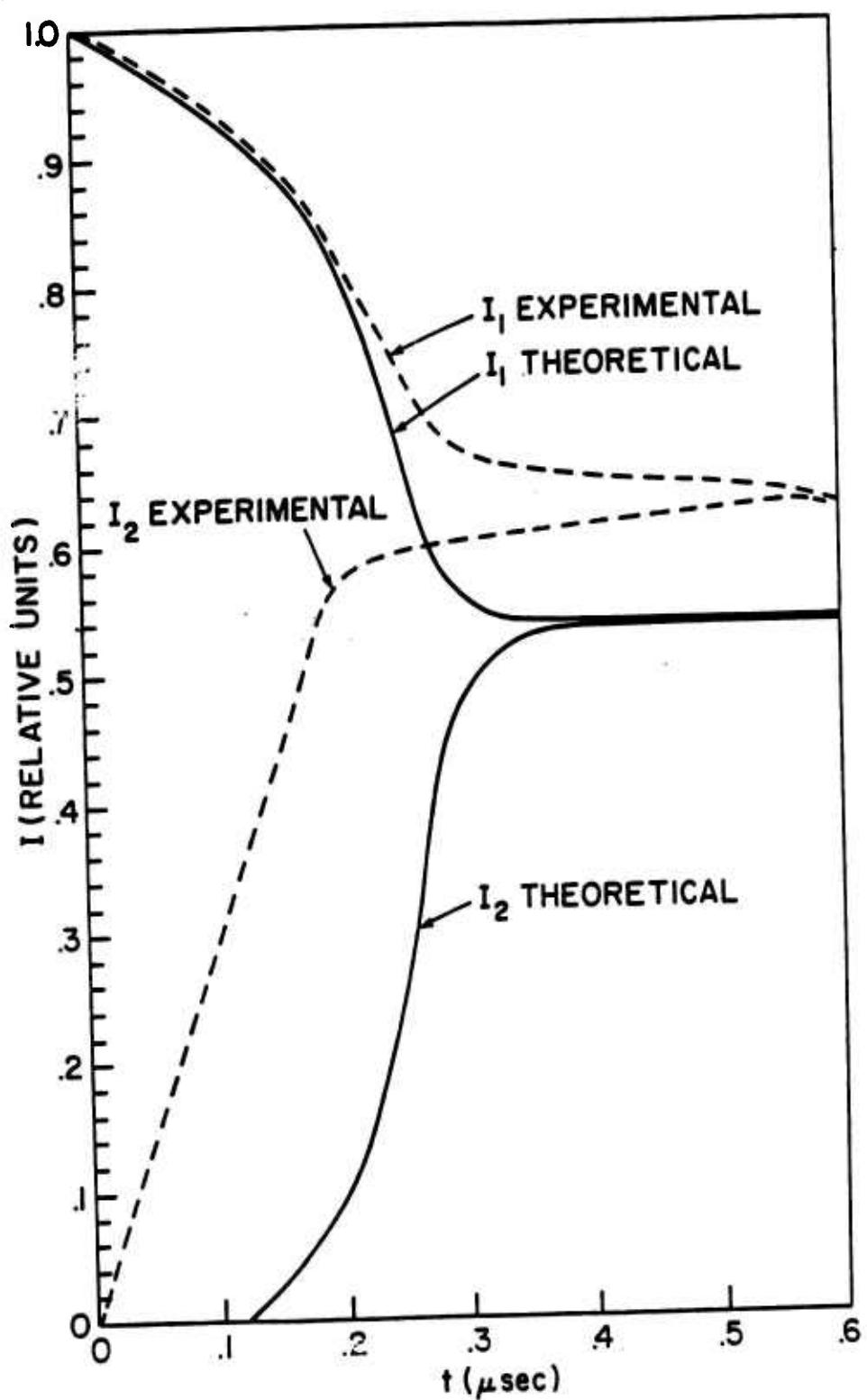
FIGURE 13 STREAK/FRAMING PICTURES OF PLASMA IMPLOSION
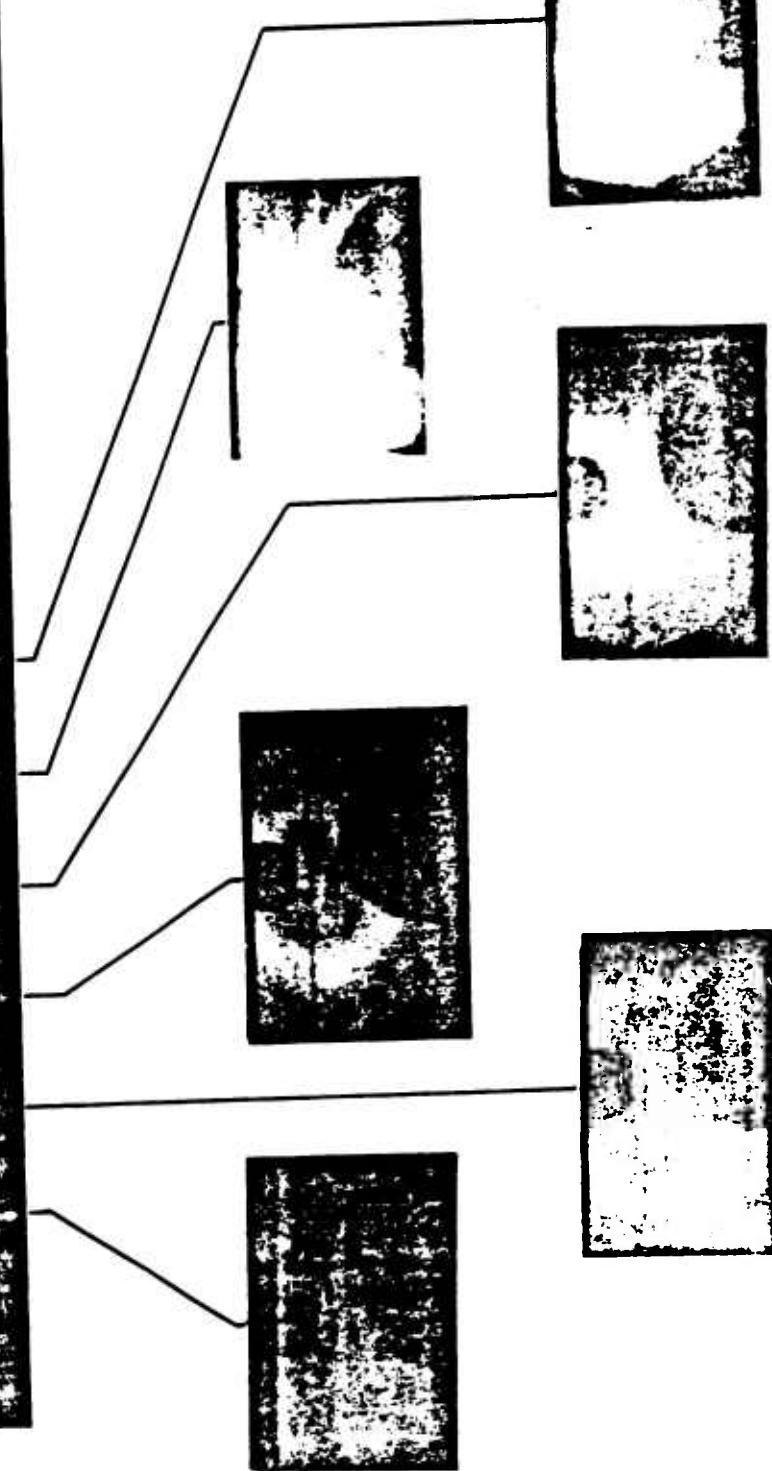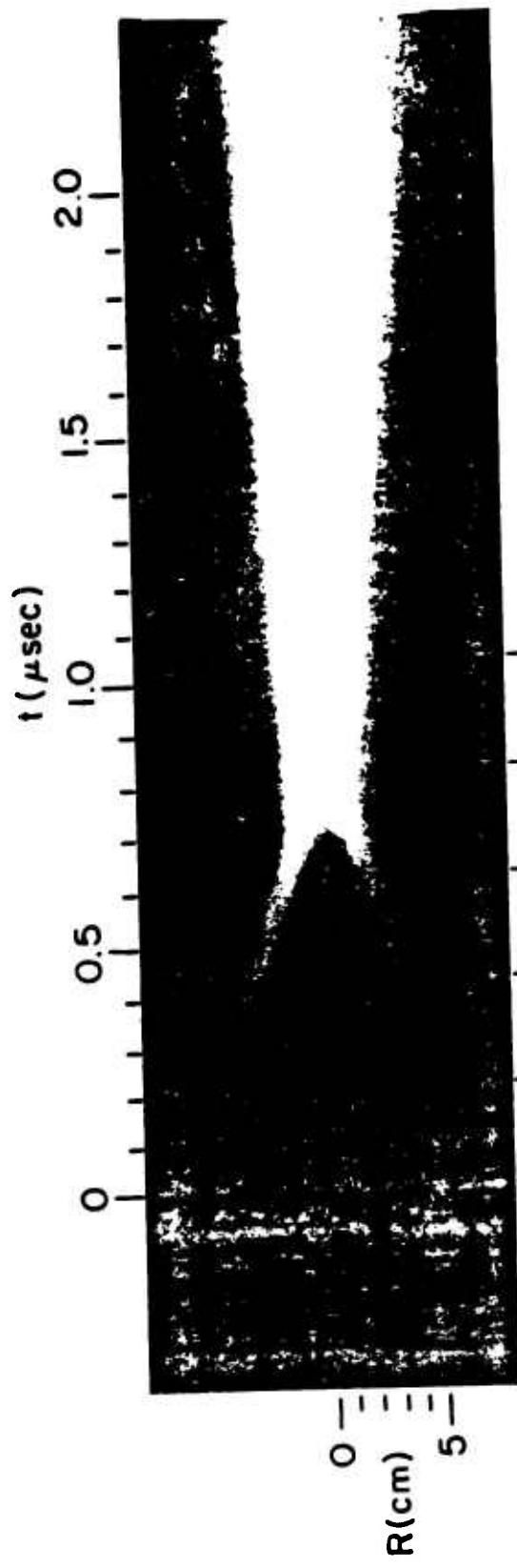
FIGURE 14 SCHEMATIC DIAGRAM ILLUSTRATING FEATURES OF STREAK PICTURE OF IMPLODING PLASMA IN A FAST Z - PINCH (NO FUSE)

FIGURE 15

RADIATION
HEATED WALL

REFLECTED
SHOCK

t (ns)

r (CM)
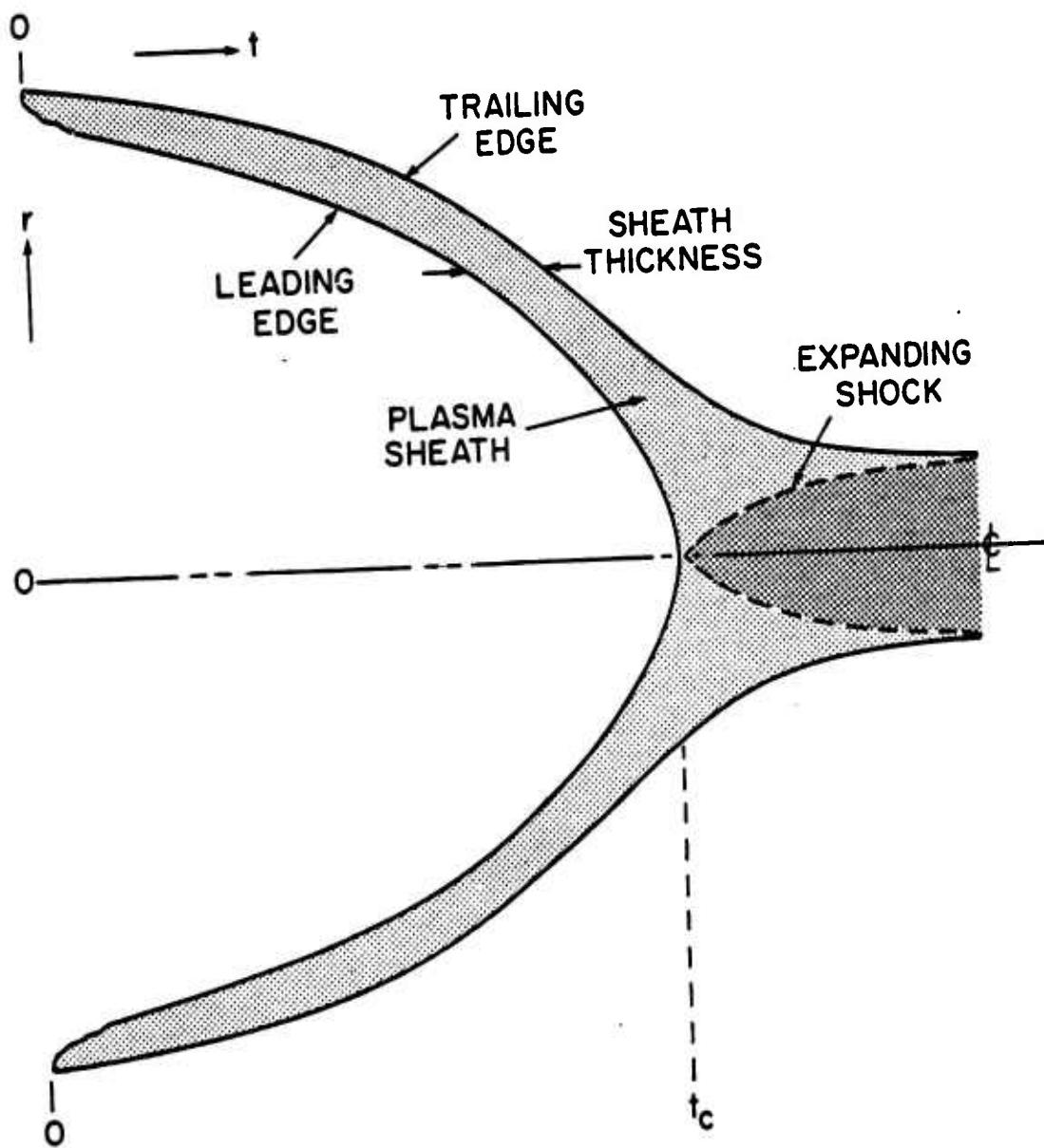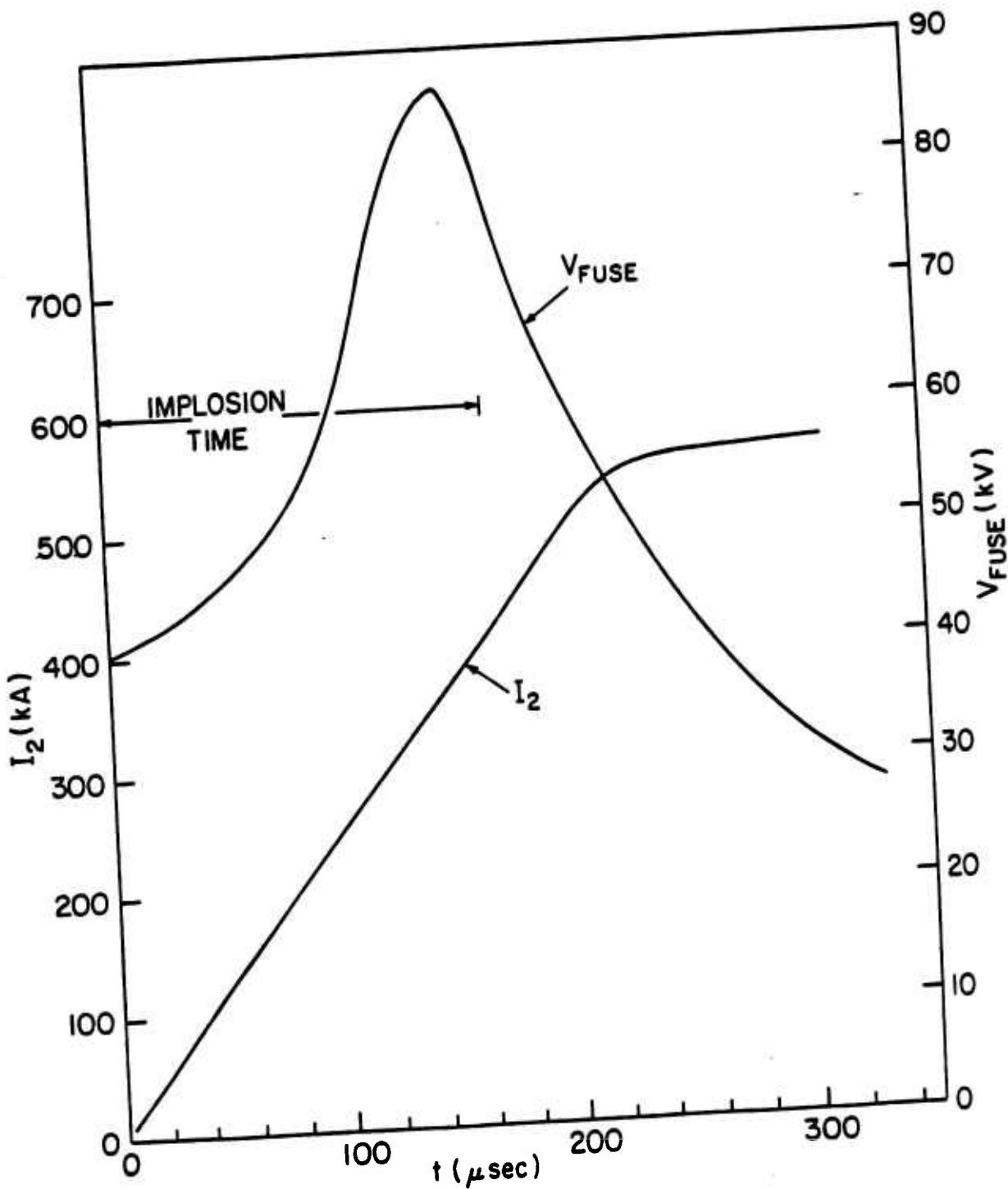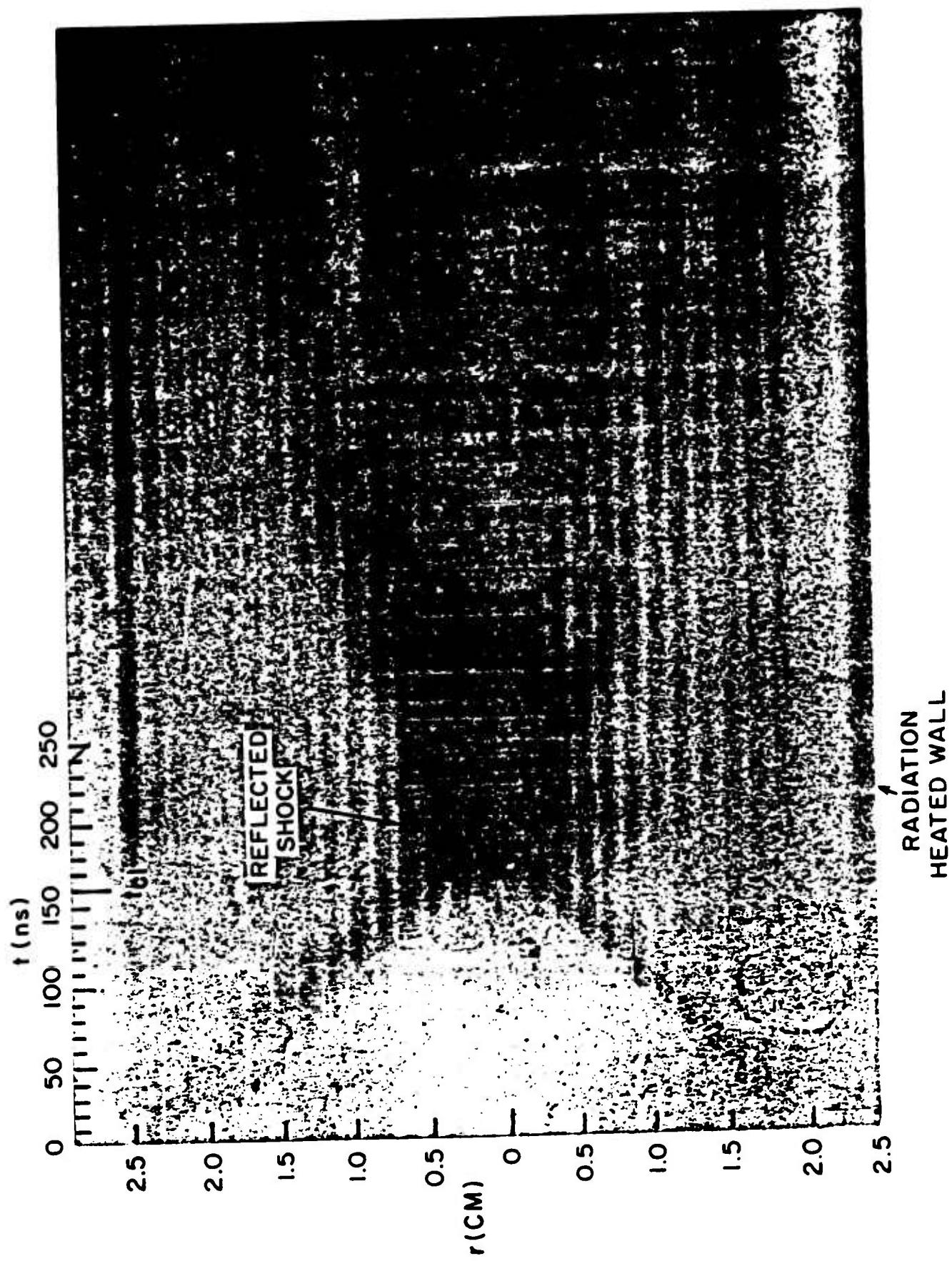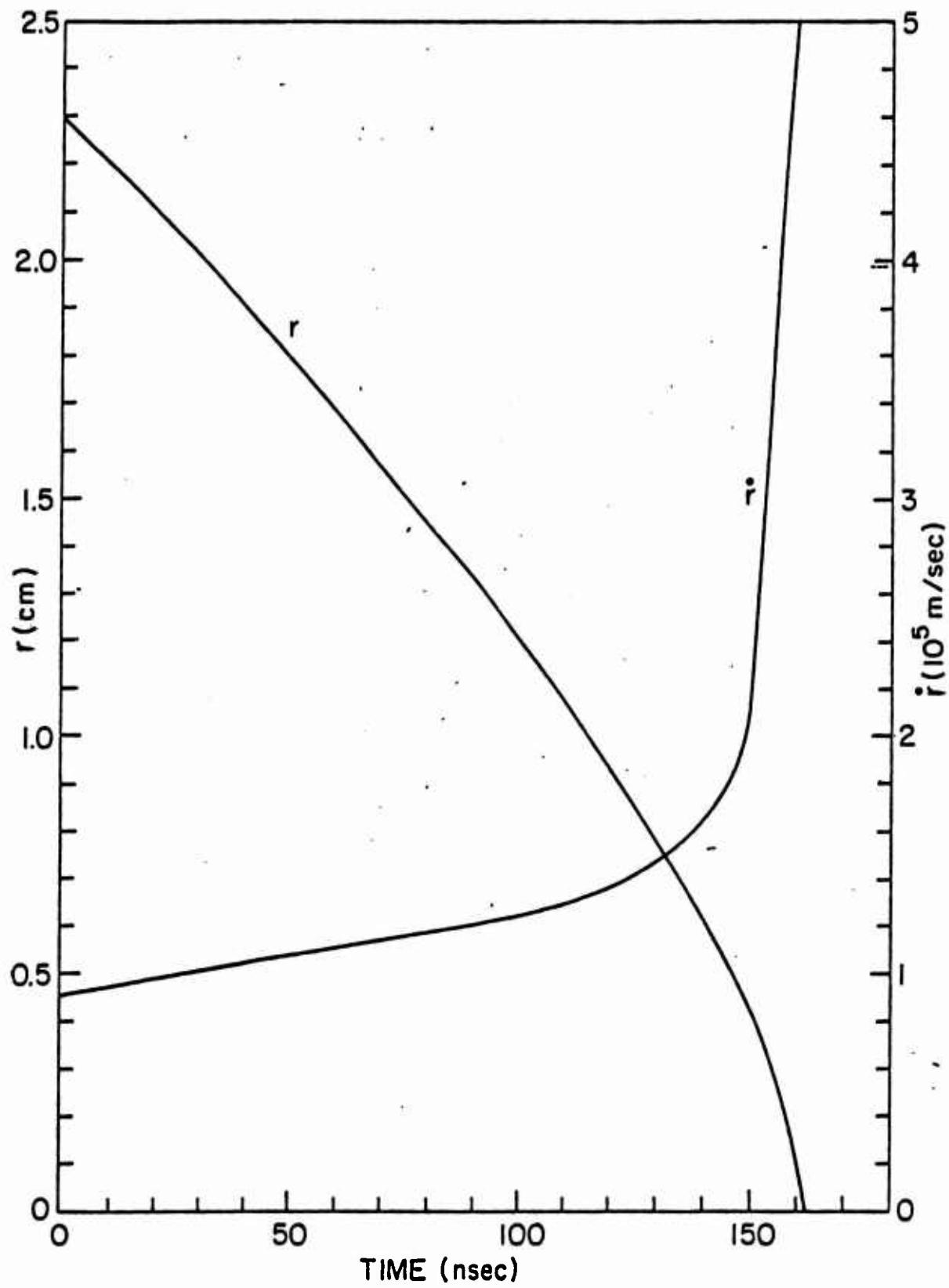
FIGURE 17

FIGURE 18  IMPLOSION DRIVEN BY FUSE STEEPENED CURRENT

FIGURE 19

FIGURE 20

RATIO OF LOAD AND FUSE IMPEDANCES $(Z_L/R_F)$

$t = t(R_0/2)$

COMPRESSION
TIME, $t_c$
LEADING   TRAILING
EDGE        EDGE

$H_2$, 0.4 TORR
$I_{MAX}$ = 500 kA

TIME (nsec)
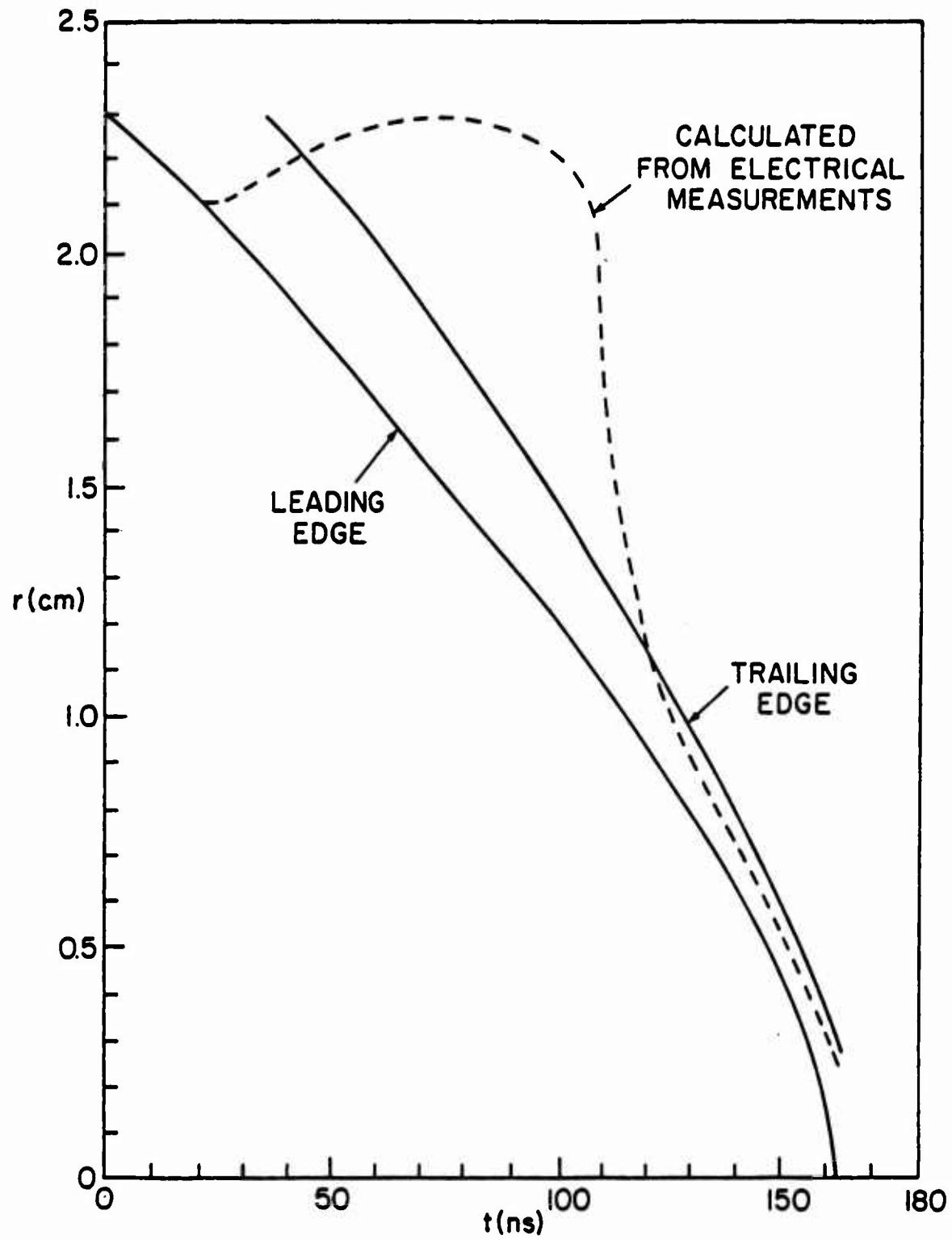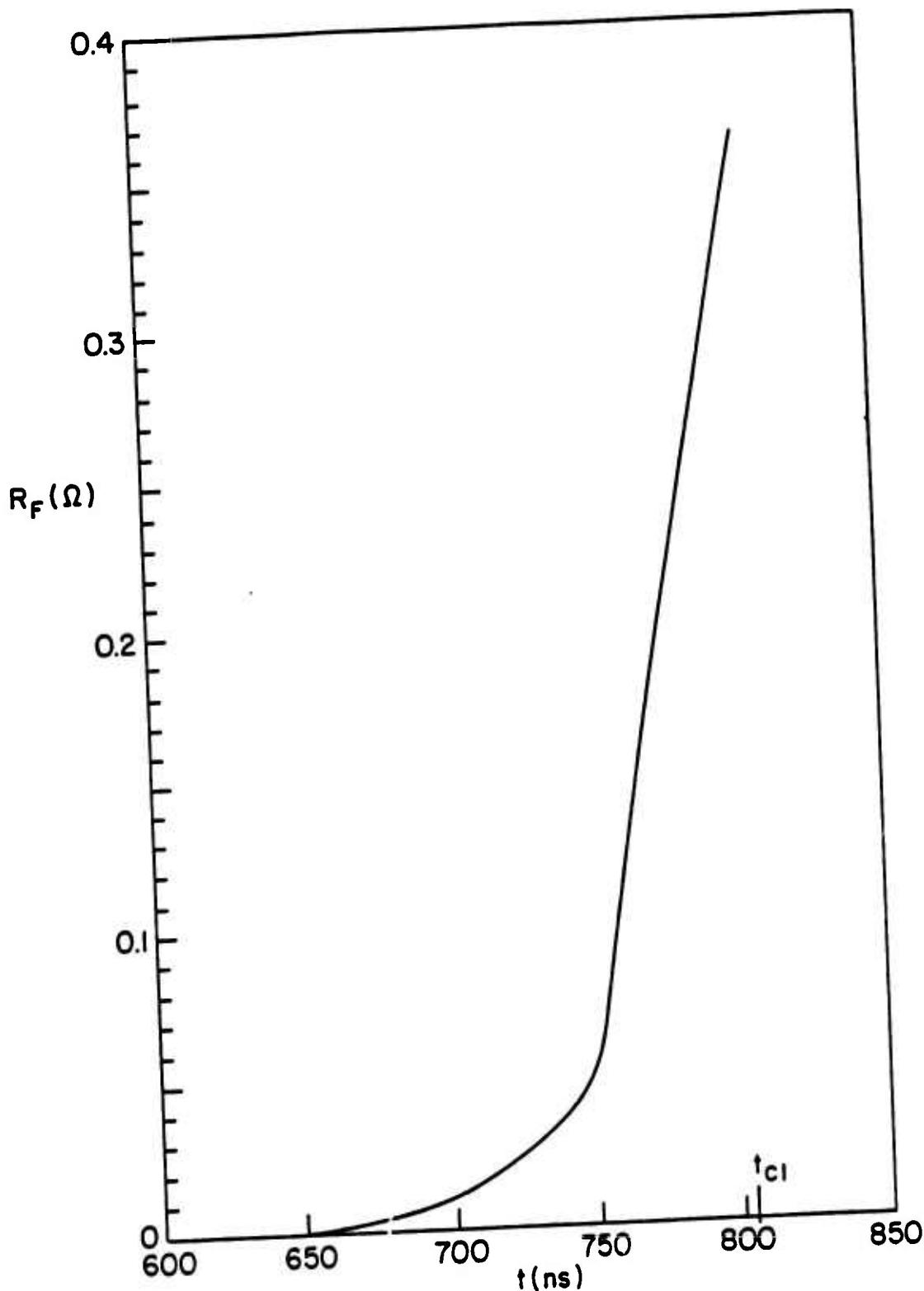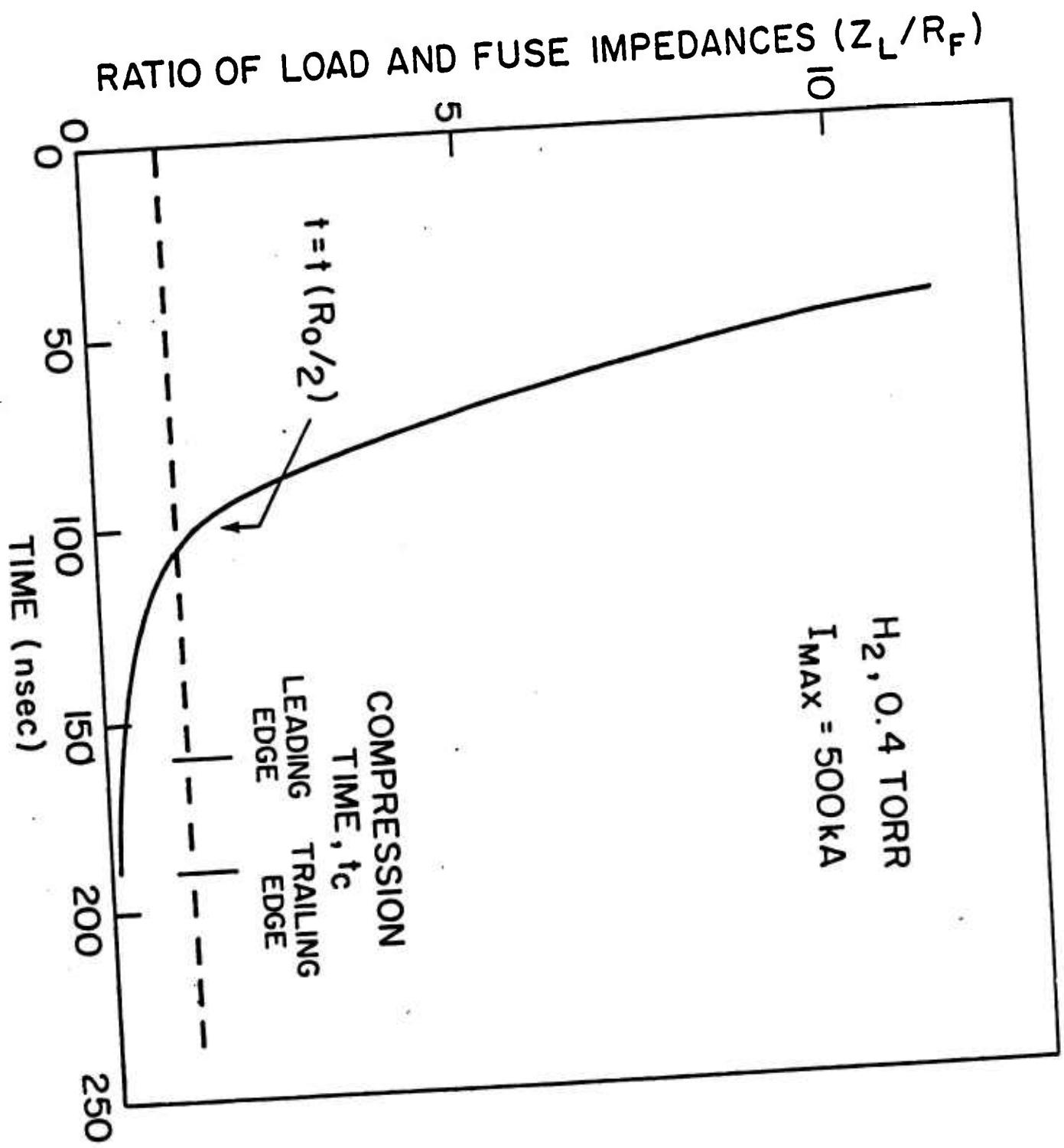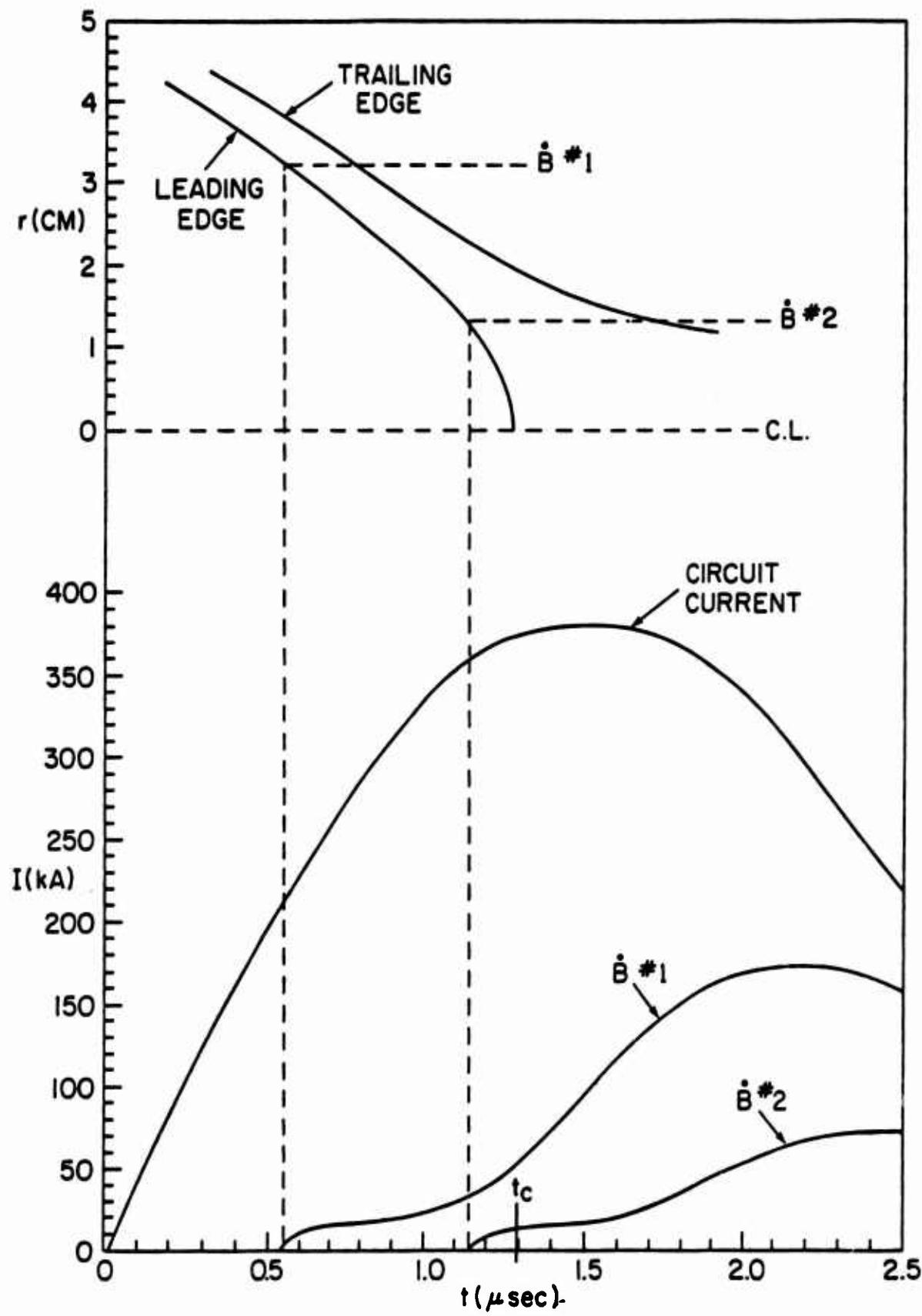
FIGURE 21

ELECTRICAL MEASUREMENTS FOR PLASMA IMPLOSION DRIVEN BY FUSE STEEPENED CURRENT
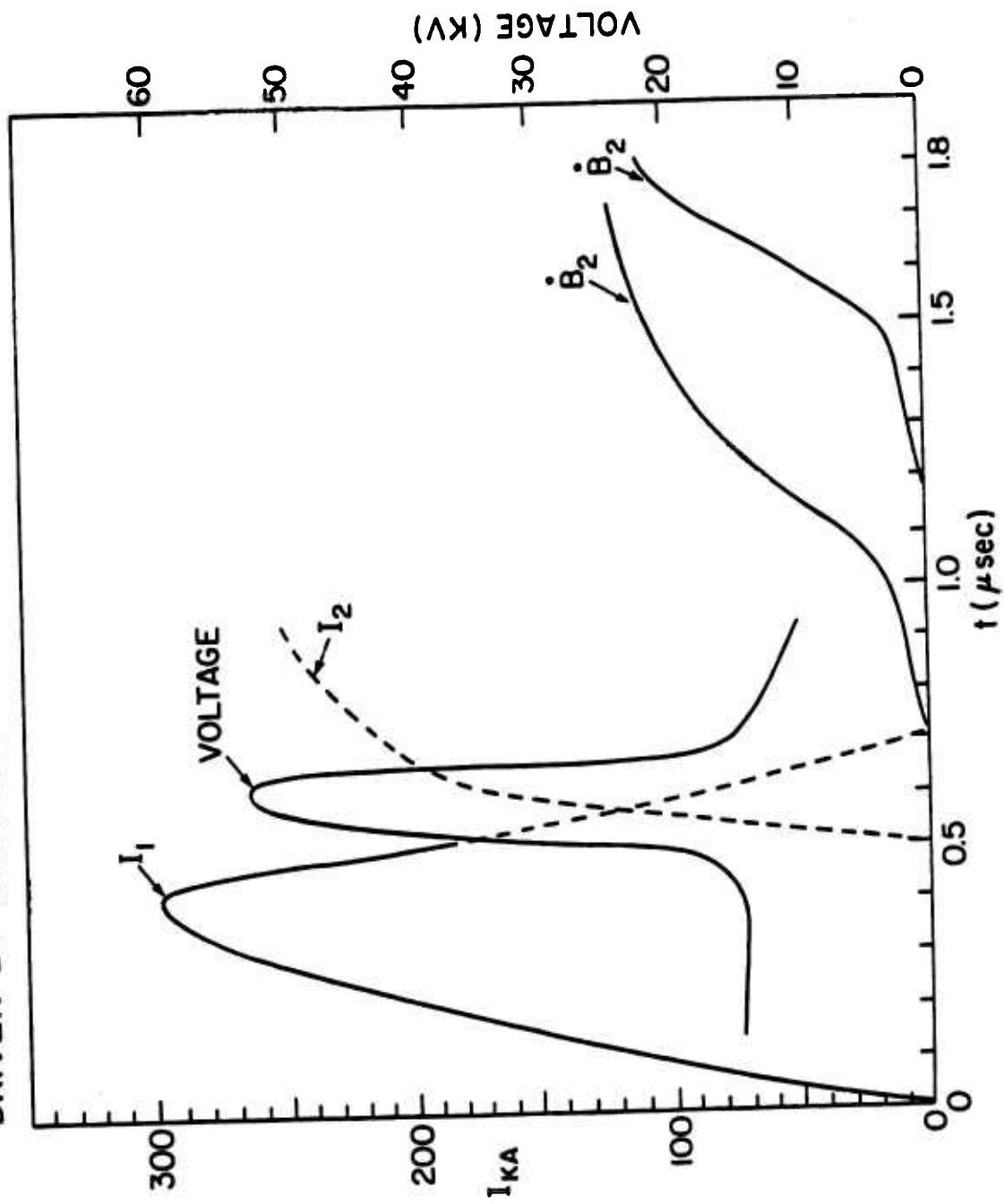
FIGURE 22

FIGURE 23 DEPENDANCE OF IMPLOSION VELOCITY AND SHEATH THICKNESS ON CURRENT RISE TIME
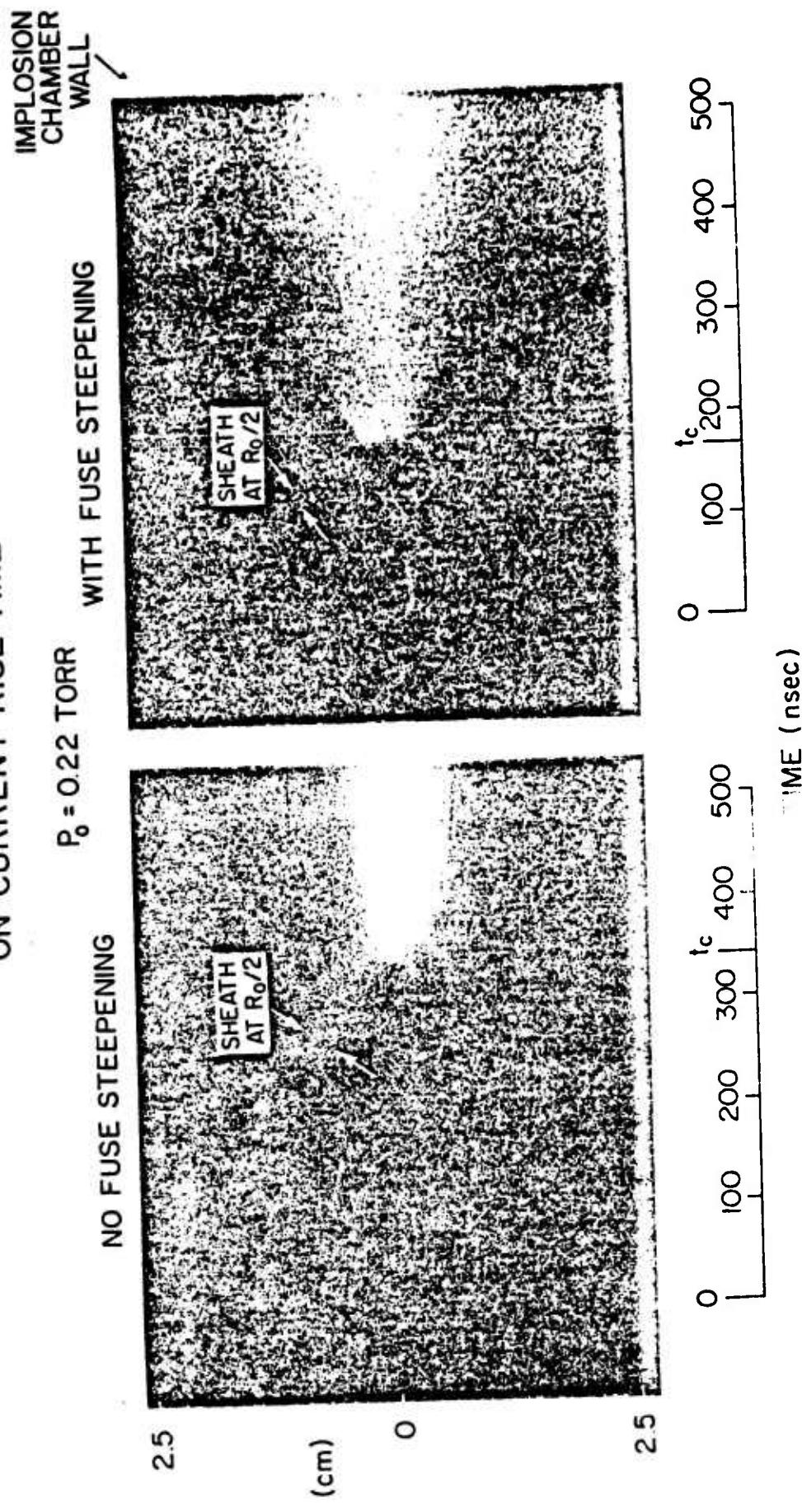
COMPARISON OF IMPLOSIONS WITH AND WITHOUT FUSE
(LEADING EDGE OF PLASMA)

FIGURE 25